Polymorphism and dynamics of the Hepatitis B virus capsid

Pepijn Moerman

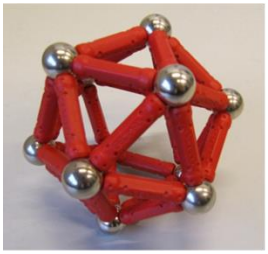
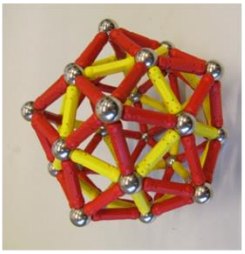
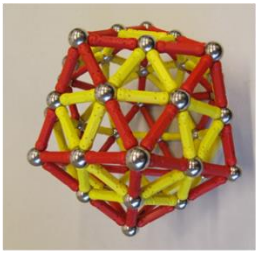
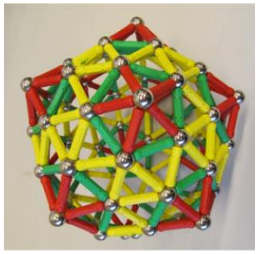

May 2014

Supervisors:

Willem Kegel
Rolf Boelens
Hans Wienk

FCC

NMR

Table of contents

Introduction

Self-assembly of colloidal particles (with sizes ranging from 1 nm to 1 μm) is, with applications in the material science and optoelectronics a widely investigated subject. In the past few years researchers have gained the ability to synthesize self-organizing, highly anisotropic particles such as bowls and dumbbells and investigated the self-assembly of particles with specific interaction patches, see Glotzer & Solomon, 2007 [1] and references cited therein. Although the understanding of self-organization and the interactions that drive the process is increasing and the number of colloidal building blocks is growing, there is still little comprehension of one of the most abundant types of self-assembly, the self-assembly of virus capsids.

Virus capsids are sphere-like hollow shells that contain and protect the genetic material of viruses. Many contain icosahedral symmetry which means that they exhibit 3, 5 and 6-fold rotation axis. A consequence of this high symmetry is that the number of capsomers that build up a capsid is quantized. Caspar and Klug [2] categorized icosahedral capsids based on their size and geometry using the T-numbering formalism, with $T = h^2 + hk + k^2$, where h and k indicate the number of capsomers (in different directions) that separate two fivefold symmetry elements. So starting from the smallest icosahedral capsid, the allowed T-numbers are 1,3,4,7,9 etc.

This mathematical characterization of virus capsids creates a picture of geometrical structures consisting of rigid building blocks, as is supported by x-ray crystallography structures. However, the building blocks of these capsids are in fact folded polymers, consisting of domains with variable flexibility, so that this image of rigid building blocks may be an oversimplification. In this perspective the comparison to assembly of man-made inorganic colloids, that really are rigid structures, is quite unfair. One may wonder about the role of this flexibility to both assembly energetics in terms of entropy and to structure geometry in terms of interaction directionality. Another factor that complicates the understanding of capsid assembly is the strong anisotropy in both shape and interaction potential of proteins as compared to colloids. The overarching goal of this study is therefore to see how far we can push the understanding of this complicated assembly behavior using a potentially oversimplified model of rigid and homogeneous building blocks. Application of the same theoretical groundwork that is used in colloid physics shows which features of the assembly can be understood from this model and which properties can only be ascribed to the detailed atomic structure of the constituent proteins and conformational changes therein.

In order to achieve this we employ a combined approach of a theoretical study to the interaction potential that drives virus capsid assembly, together with an experimental study of protein dynamics. In the first two parts we compare simple physical models with experimental data to see where they are accurate and where they flaw. In the third part the dynamics of the the Hepatitis B virus capsid are mapped using solution state NMR spectroscopy to gain insight in the degree and location of flexibility in the constituent proteins.

References

1. Glotzer, S. C. & Solomon, M. J. Anisotropy of building blocks and their assembly into complex structures. *Nat. Mater.* **6,** 557–62 (2007).

2. Caspar, D. L. D. & Klug, a. Physical Principles in the Construction of Regular Viruses. *Cold Spring Harb. Symp. Quant. Biol.* **27,** 1–24 (1962).

Part 1

Thermodynamics of virus assembly

This part deals with a theoretical study of virus capsid assembly. We will consider the interaction potential that drives the assembly process, which consists of a hydrophobic attraction balanced by an electrostatic repulsion. The model proposed by Kegel and Van der Schoot on the temperature and salt concentration dependence of the interaction strength will be reviewed and extended with pH dependence. The models will be compared with experimental data on the assembly of hollow capsids of the Hepatitis B Virus, Norovirus and the Brome Mosaic Virus. Based on the comparison we will describe where the model is accurate and where it flaws.

1.1 Thermodynamics of virus capsid assembly

Abstract

The coat proteins of numerous virus capsids show variable assembly behavior depending on temperature, salt concentration and pH. This phenomenon is often explained by conformational switching between an assembly-active and an assembly-inactive state, but can also be understood as the consequence of a tunable interaction potential that consists of a hydrophobic attraction balanced by an electrostatic repulsion. Kegel and Van der Schoot modeled the equilibrium constant between Hepatitis B virus capsids and their building blocks as function of temperature and salt concentration using simple thermodynamic equilibrium considerations. We present an extended version of this model that also takes the pH dependence of virus capsid stability into account and compare it to datasets by Zlotnick *et al.* and Wingfield *et al*. to obtain a complete model that describes the interaction energy as a function all three variables: pH, salt concentration and temperature. Furthermore we test universality of the model by comparing it with data available for the Norwalk virus.

Introduction

Hepatitis B (HBV) is an enveloped icosahedral virus that causes infectious liver inflammation. Apart from an infecting agent, the Hepatitis B virus is a regularly used and well investigated model system for virus capsid self-assembly [1-4]. The EM and X-ray structure showed that majority of the virus capsids contain T=4 [5] symmetry and a minor amount of capsids contains T=3 symmetry [6,7]. The capsids are built from dimers of the core protein HbcAg. Only the N-terminal 149 residues of this domain are vital for assembly. The C-terminal arginine-rich domain, often referred to as the protamine domain [8], was found to be responsible for RNA binding [9]. A construct of this protein missing the C-terminal 34 amino acids is called Cp149 or HbeAg.

Zlotnick [10] found that depending on different salt concentrations and temperatures the Cp149 dimers do or do not self-organize to form virus capsids. He suggested this was due to the presence of a conformational change that switched between an inactive and an assembly active state. Kegel and Van der Schoot convincingly showed that the self-assembling behavior based on temperature and salt concentration can also be explained using a simple physical-chemical model [11].

They suggested that the total interaction energy per capsomer can be described using an attractive term based on hydrophobic interactions and a repulsive term based on coulombic interactions. The model was validated by linking the interaction energy to the equilibrium constant using the following equation:

$$\frac{-\Delta G}{kT} = \ln(Keq) \qquad (1)$$

There appeared to be good correspondence with the experimental data by Zlotnick *et al.*[10] who measured equilibrium constants under various salt concentrations and temperatures. However no results were presented on the variation of the variation of the monomer concentration with pH.

An extended version of the same expression could account for data on the Tabacco Mosaic Virus, containing linear rather than icosahedral geometry [12]. This suggests that the model indeed has grasped some collective properties of viral self-assembly so that it should be universal over a large class of viruses.

Also the capsomers of the Norovirus have been shown to spontaneously and reversibly self-assemble into empty virus capsids under proper conditions so that this system can be used to put the universality of this model to the test. The Norovirus or Norwalk virus (NWV) is a single-stranded RNA virus that is responsible for the majority of outbreaks of viral gastroenteritis. EM and X-ray structures show that the capsid consists of 90 major capsid protein dimers ($VP1_2$) that encapsulate the viral RNA and minor capsid protein VP2 [13]. Most capsids have T=3 symmetry and an outer radius of 38 nm VP1 consists of an S (Shell)

domain that is responsible for capsid formation and a P (Protrusion) domain that is involved in dimerization. Under some conditions also the T=1 geometry is observed [14].

Thus the aim of this paper will be to extend the model proposed by Kegel and Van der Schoot with pH variation and check its internal consistency over multiple datasets. The data available on Hepatitis B to compare our model with are listed in table 1. Moreover we will include a description of data on the Norwalk virus to substantiate the idea that the presented expression for the free energy of association is universal.

Table 1. *Datasets available for about the effects of temperature, salt concentration and pH on the critical capsid concentration.*

	Wingfield [2]	**Zlotnick** [10]	**Shoemaker** [14]
Salt	pH=7.0 T= 295K	pH=7.5 T=273-303K	T=298K pH=6-9
pH	0.25M NaCl T=277K	-	T=298K 0.25M NH_4CH_3COO
Temperature	-	pH=7.5 0.15-0.7M NaCl	-

In the following section we will describe the extension to Kegels model. Next we will apply it to the available experimental data by Wingfield *et al.* and Zlotnick *et al.* to obtain a complete model (*i.e.* salt concentration, pH and temperature dependence) and check the internal consistency. In the remainder of the paper we will describe data by Heck *et al.* to see how general the model and its parameters are.

Description of the model

For simplicity, we use the critical capsid concentration (c.c.c.)(analogous to the critical micelle concentration) rather than the equilibrium constant that is generally used. The c.c.c. can be linked to the interaction energy using the following expression:

$$\ln[c.c.c.] = \frac{< u >}{kT} \qquad (2)$$

Following Kegel and Van der Schoot, $\frac{<u>}{kT}$ represents the total interaction energy per capsomer in units of kT and is given by equation 3.

$$\frac{<u>}{kT} = -\frac{A_H * \gamma}{kT} + A_C * \sigma^2 * \lambda_B * \kappa^{-1} \qquad (3)$$

Here A_H represents the hydrophobic surface area, which was estimated by Ceres and Zlotnick (2002) to be around $1.56*10^{-15}$ m^2 for the T=4 capsid, which corresponds to 13 nm^2 per capsomer. A hydrophobicity plot on the X-raystructure of the protein can be found in the supplementary material. γ Is the temperature dependent interfacial tension between proteins and water. A_C represents the coulombic surface area. We approximated this by dividing the total capsid surface by the number of capsomers. This leads to a value of 23.3 nm^2 of electrostatic surface per dimer. The charge screening is described by the Bjerrum length λ_B, that is 0.7 at room temperature and the Debye screening length, that is 0.3 divided by the square root of the salt concentration for a 1:1 electrolyte at room temperature.

The temperature dependence of the hydrophobic attraction is obtained via the first term of a Taylor expansion of the surface tension around a reference temperature T_0:

$$h(T) = -A_H\left[\gamma(T_0) + \frac{\delta\gamma}{\delta T}(T - T_0)\right] \qquad (4)$$

Where the reference temperature T_0 is 273K. Kegel and Van der Schoot compared this model with data by Zlotnick *et al.* and obtained the fit values of 19 kT for the hydrophobic attraction <u> at the reference temperature and an average of 0.04595k for $A_H\frac{\delta\gamma}{\delta T}$, the excess surface entropy. A reproduction of their fit using the critical capsid concentration is shown in Figure 1

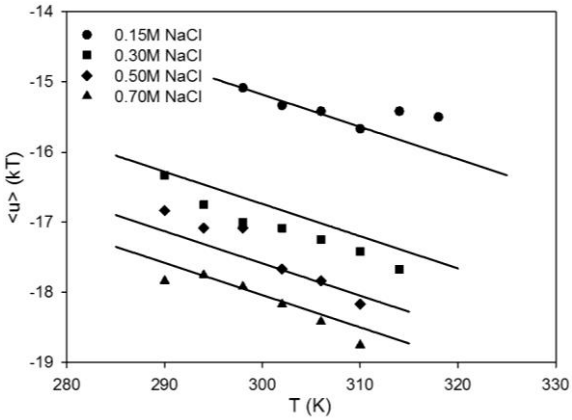

Figure 1. *Variation of total interaction energy as function of temperature. The dots show experimental data by Zlotnick at different salt concentrations. The lines are a fit based on charge and hydrophobic attraction energy as obtained from the analysis of salt concentration data. The temperature dependence of the surface tension multiplied by the hydrophobic surface area ($\boldsymbol{A_H \frac{\delta\gamma}{\delta T}}$) was used as a fit parameter. We found as an average over the four fit lines $\boldsymbol{A_H \frac{\delta\gamma}{\delta T}}$ = 0.04595k. The plotted model lines are based on this value rather than their individual fit values since this variation with temperature should be salt concentration independent.*

The pH dependence of the interaction between virus capsomers lies within the protein charge density. Equation 3 explains how the interaction energy varies with charge, but the pH dependence of the charge is somewhat more complicated. Protein charge originates from several ionizable amino acids. Aspartic acid, glutamic acid, cysteine and tyrosine can carry negative charges where arginine, lysine and histidine can carry positive charges. The expression for charge variation with pH is greatly simplified when we assume that all amino acids are surface exposed and that they can be ionized independent of each other. The first assumption is rather accurate because it is energetically favorable for a protein to have its hydrophobic residues buried and its polar and charged residues exposed. The second assumption holds only for relatively low charge densities. For highly charged proteins renormalization could occur. For now we assume that the surface charge density of $VP1_2$ is still below the renormalization limit.

The average charge of a single type of amino acid can then be described by a transformation of the Henderson Hasselbalch equation (derivation in supplementary material):

$$z = \sum_{i=1}^{b} \frac{n_{i,b}}{1+10^{pK_{a,i}-pH}} + \sum_{j=1}^{a} \frac{n_{j,a}}{1+10^{pH-pK_{a,j}}} \quad (5)$$

The first term accounts for all the acidic amino acids with $pK_{a,i}$ is the pKa corresponding to amino acid of type i and n_i is the amount of this type of amino acid. Likewise the second term accounts for all basic amino acids. The contribution of the C and N terminus of the amino acid chain can be shown to be negligible.

Theoretical pH-titrations

Simply filling in equation 5 with the amino acids form the protein sequence and their concomitant average pKa values gives the pH dependence of the protein charge. The results are presented as theoretical pH titration curves in Figure 2 for NWV and Figure 3 for HBV.

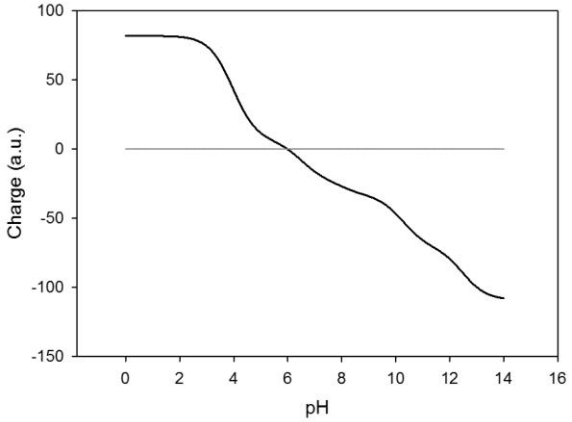

Figure 2. *Charge of the Norovirus capsid protein as a function of pH. The graph is a theoretical pH titration based on a transformation of the Henderson Hasselbach equation. From this model we expect a PZC of 6.*

From this curve we can read that the point of zero charge of NWV lies around pH 6. It is reassuring that in accordance with this finding Goodridge *et al.* [15] measured an isoelectric point of 5.9 for the Norovirus capsid.

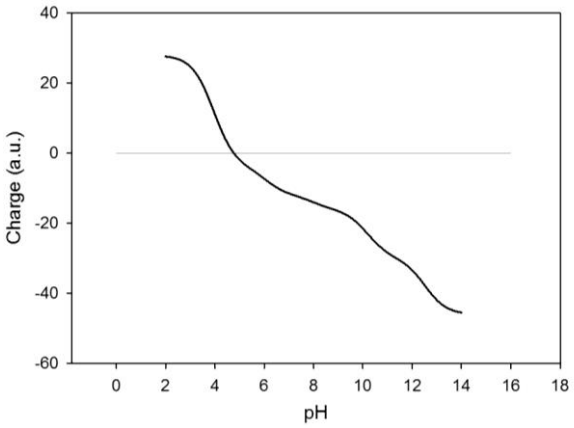

Figure 3. *Surface charge of Hepatitis B capsomers as a function of pH as modeled using a transformation of the Henderson Hasselbalch equation.*

Similarly for HBV we expect an isoelectric point of around 4.5 to 5, which is in good correspondence with the pI values of 4.3 to 4.8 that were obtained by Yamada *et al.*[16] and is comparable to the pI value of 4.88 measured for the full capsid protein HbcAg [17]. One may appreciate that although the number of charges on the Norovirus is considerably higher, the surface charge density of both HBV and NWV is similar. Charge densities are around 0.25 and 0.22 charges per nm^2 respectively at pH=8. This observation suggests that surface charge density might be a conserved property for viruses.

It should be noted that the shape of the theoretical titration curve is sensitively dependent on the number of free cysteines. Cysteines are slightly acidic residues having an average pKa of 8.0 and thus can contribute to protein charge. However, when they are oxidized to form sulfur bridges they can no longer become ionized. The HBV dimer contains a total of 6 cysteines of which C61 of both monomers are involved in an inter-monomer disulfide bridge. C48 is believed to be present as a mixture of both its oxidized and its reduced form [18]. We approximate that on average one of the two C48's will be ionizable so that we used 3 free cysteines per dimer in the model. A similar analysis of NWV leads to the use of 11 free cysteines.

Influence of electrostatics on Hepatitis B stability

With the protein charge fixed we can apply the model to pH data of HBV obtained by Wingfield *et al.* [2] taking for the hydrophobic attraction a value of 19kT as was found by Kegel and Van der Schoot. Data by Wingfield were converted to critical capsid concentrations using the following equation:

$$c.c.c. = \frac{\frac{n_{free}}{n_{tot}} * c_{tot}}{c_{water}} \qquad (6)$$

Where n_{free}/n_{tot} is the fraction of free capsomer, c_{tot} is the total capsomer concentration in mol/L and c_{water} is the molarity of water = 55.6 mol/L.
An overlay of the experimental data and the model is shown in Figure 4. The model describes the data surprisingly well for this pH range, which a posteriori justifies the coarse description of the pH dependence on the charge that we assumed.

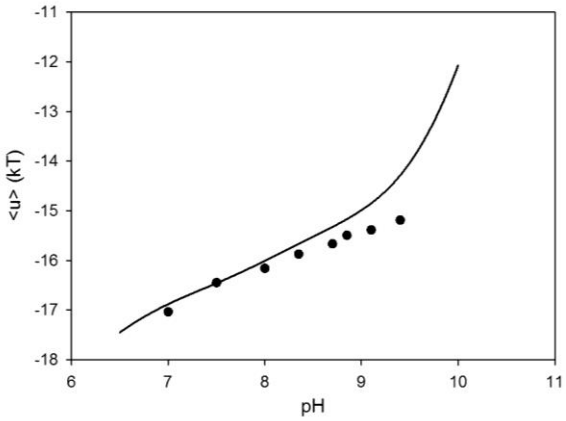

Figure 4. *Variation of the total interaction energy between capsomers as a function of pH. The dots represent data obtained by Wingfield et al. and the line represents the prediction by our model. For the hydrophobic attraction the 19 kT were used that Kegel and Van der Schoot found in their analysis.*

Now that the model can relatively well account for both the pH data by Wingfield *et al.* and the temperature data by Zlotnick *et al.*[10] it would be interesting to make the connection between the two datasets via the ion strength dependence in order to obtain a complete description of the interaction energy as function of all three variables: pH, salt concentration and temperature.
There are however two differences in the datasets by Zlotnick and Wingfield that need to be taken into account before attempting to describe them. For a start Zlotnick measured at a pH of 7.5 and Wingfield at a pH of 7.0. This will have a consequence for the slope of the graph. Furthermore Zlotnick used a Tris-HCl buffer, which is ionic and thus affects the ionic strength of the solvent, where Wingfield used a HEPES based

buffer that does not significantly affect the ionic strength.

For the salt dependence as measured by Zlotnick *et al.* we took the data at an arbitrarily set reference temperature of 273K. From this we calculated the critical capsid concentrations through dividing by 120 (number of capsomers). The number of charges on the capsomers can easily be calculated using equation 5. For pH=7 this gives 11.2 average charges per capsomer. For pH=7.5 we obtain a charge of 14.2. Filling in these values we have again a parameter free model to plot together with the concomitant experimental data. Kegel and Van der Schoot performed a model based fit through the data by Zlotnick *et al.* and obtained a charge of 14-15 per capsomer which is in excellent correspondence with our finding. Figure 5 shows both datasets and the model so that they can be easily compared.

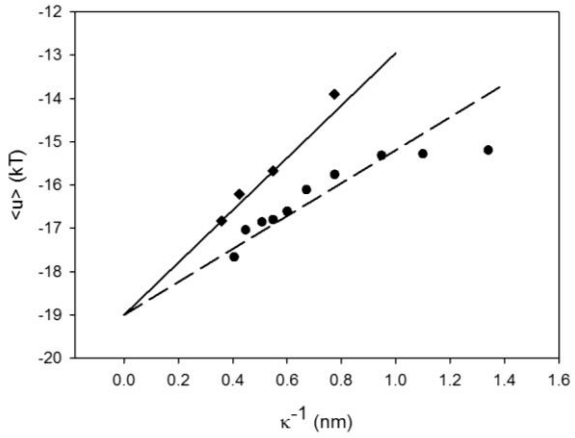

Figure 5. *Ion strength dependence of the total interaction energy per capsomer as observed by Zlotnick (diamonds) and Wingfield (circles). The lines represent predictions of the salt concentration dependence, where no fit parameters are used. The hydrophobic attraction was obtained from fitting with the temperature and pH dependent experiments. The charge of the particles is calculated using equation 5. The data appear to be consistent with each other.*

Influence of electrostatics on Norovirus stability

A similar analysis can be performed for the Norovirus where the model can be compared with mass spectrometry data by Heck *et al.* In this case A_c was calculated assuming that the capsomer is spherical and using the protein mass and the expression for a protein density as proposed by Fischer *et al.* [19]. We calculated a surface area of 126 nm^2. Note that this is different from the calculation for HBV where we divided the total capsid surface by the number of capsomers. Effectively, for HBV we consider only electrostatic interactions on the outside of the capsid, where for the NWV we assume that the entire protein surface contributes to electrostatic interactions. Reason for this choice is that model and data cannot be brought to agreement with another choice for the electrostatic surface area, but difference between NWV and HBV can be validated based on the different morphology of the viral coat proteins. The HBV protein is small and assembles into a large (T=4) and thin shell so that over 50% of the protein surface is exposed to the exterior. The Norovirus coat protein on the other hand is large and assembles into smaller (T=3), much thicker shells so that only a small fraction is exposed and a significant part of the homogeneously charged surface is buried. In such case one can imagine that the surface charge should be calculated by dividing the total number of charges by the entire protein surface, and not only the exterior part of this surface. The other parameters that were used are λ_B is which is 0.7 nm at room temperature and κ^{-1} is $0.3/\sqrt{c_s}$ for a 1:1 electrolyte in aqueous solution. The salt concentration c_s is 250 mM which gives a value of 0.6 nm for κ^{-1}. The fit is shown in Figure 6.

The model for the variation of the interaction energy with pH clearly gives also for this virus an excellent description of the experimental results. The fit gives a value for the hydrophobic attraction energy of 20 kT, which is very reasonable. Compare this for example with the hydrophobic energy of 19 kT for Cp149 (the HBV capsid protein) and 17 kT and 16 kT for respectively the TMV disk and helix [12]. Dividing by a hydrophobic surface of 2000$Å^2$ per capsomer [13] gives a surface tension of 4.6 mN/m, which is similar to the 5.5 mN/m that Kegel and Van der Schoot found for HBV.

Note also that the value for pH=6 is actually an upper boundary. At this pH all the capsomers were absorbed in capsids and no free proteins were observed. At this point our model deviates slightly from the observations.

We find a more shocking result when we consider the observation that the Norovirus capsid was

found to be stable at acidic pH [20]. Mechanical capsid stability was even reported at pH values as low as 3 [21].

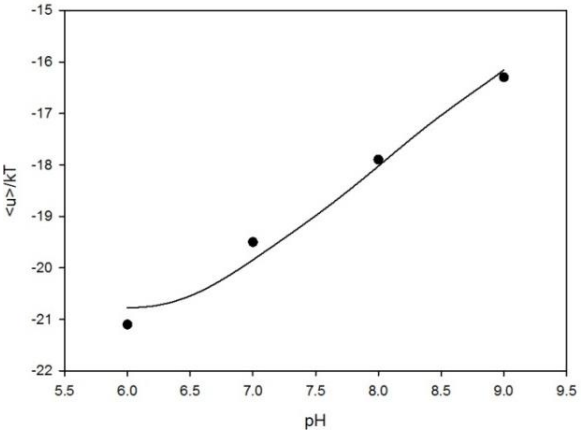

Figure 6. *Fit of the previously described model to experimental data measured at 250mM ammonium acetate. The only fit parameter was the hydrophobic attraction. The formula of the fitted function and results of the fit are shown below the graph.*

When we look at our model though, we would expect the electrostatic repulsion to increase when the pH falls below 6. At pH=6 the protein carries no net charge and the only interaction is the hydrophobic attraction. At lower pH the capsomer starts to build up a net positive charge. At pH=4 this should be in the order of 50 net charges already. This is completely incompatible with the observations that all capsomers are adsorbed in capsids at these low pH values. The most likely explanation for this anomaly is a strong hysteresis effect.

So we cannot explain the observation for pH=6 and lower using our model, because it assumes a reversible interaction, but the observations at higher pH are easily described. Next we want to check if this model is consistent with the observations of capsid stability at different salt concentrations at pH=8 and pH=9.

From the fit in Figure 6 we gained a value for the hydrophobic attraction energy and the charge of the protein at a certain pH follows directly from the modified Henderson Hasselbalch equation so that all parameters are fixed. Using these values we have again a model for the change of capsid stability with salt concentration. *Figure 7* shows data obtained by Heck *et al.* as well as a prediction based on our analysis of the pH variation.

The first thing we notice from this figure is that our predicted energies are close to the experimentally observed values. Especially for $\kappa^{-1} = 0.6$ nm (corresponding to a salt concentration of 250mM), there is a significant conformity between theory and experiments. At both lower and higher salt concentrations however, the measurements deviate from our theoretical line. According to the model the electrostatic repulsion depends linearly on the Debye length and so we expect a plot of the natural logarithm of the c.c.c. versus κ^{-1} to give a linear relationship. We find however sublinear behavior that is reproducible for two pH values and that was also observed in the analysis of HBV.

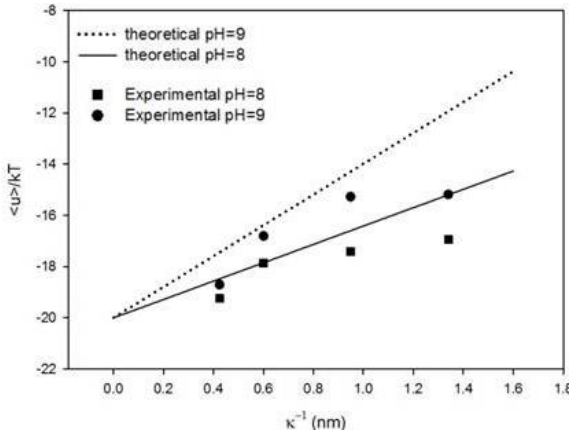

Figure 7. *Ion strength dependence of the total interaction energy. The experimental value at $\kappa^{-1} = 1.34$ and pH=9 is actually a lower boundary. At this point no capsids were observed so the c.c.c. was not reached yet.*

Note that the sublinear behavior of the salt dependence starts to play a role only at large Debye screening lengths (corresponding to very low salt concentrations). This could be explained by charge renormalization. In our model we assumed that the surface charge was still below the renormalization limit, but we did not verify this. A simple theoretical parameter that indicates whether or not charge renormalization is likely to occur is the far field potential ψ. When ψ approaches 2 (or minus 2 in the case of a negative charge), renormalization is expected [22].

$$\Psi = \frac{z_{max} * \lambda_B}{2r\left(1 + \frac{r}{\kappa^{-1}}\right)} \qquad (7)$$

Here z_{max} is the pH dependent net charge the protein carries if no normalization is taken into account and r is the radius of the protein, approximately 3nm. Plotting this expression versus the pH and taking 1.34 nm for κ^{-1} gives Figure 8.

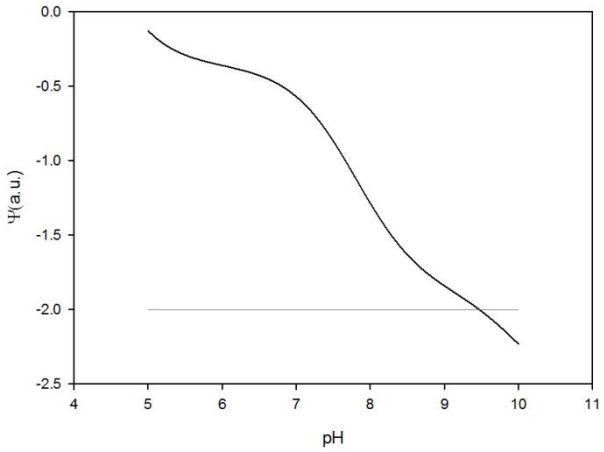

Figure 8. *Theoretical far field potential of $VP1_2$ at a salt concentration of 50 mM. The far field potential reaches the charge renormalization limit of 2 only if the pH increases above pH=9.*

At pH=9 Ψ approaches 2, so charge renormalization could account for part of the difference at low salt concentrations at pH=9, but it can definitely not fully account for the observed trend at pH=8.

Influence of temperature on Norovirus stability

For hepatitis B we already showed that the hydrophobic attraction increases linearly with increasing temperature. For the Norovirus this kind of data are lacking, but we can provide a prediction of the dependency of the capsid stability on temperature based on analogy with Hepatitis B.

For NWV we know neither the hydrophobic surface area A_H nor a value for the surface tension, but we do know that the hydrophobic attraction at the reference temperature, $A_H\gamma(T_0)$, is 20.3kT (see figure 3). If we make the reasonable assumption that the surface tension between protein and water is equal for different proteins, we can use the $\gamma(T_0)$ of 1.46kT/nm^2 calculated by Kegel and Van der Schoot for Hepatitis B, to find a hydrophobic surface area of 13.9nm^2. Kegel and Van der Schoot also found $A_H\frac{\delta\gamma}{\delta T}$=0.04595k for Hepatitis B. Using the hydrophobic surface area of both proteins, we can calculate $A_H\frac{\delta\gamma}{\delta T}$=0.04913 for $VP1_2$. Figure 9 shows a prediction of the temperature dependence of the interaction energy based on these values. If this prediction were to be verified, that would be a strong indication that the model proposed by Kegel and Van der Schoot is universal for virus assembly and not just specific for Hepatitis B.

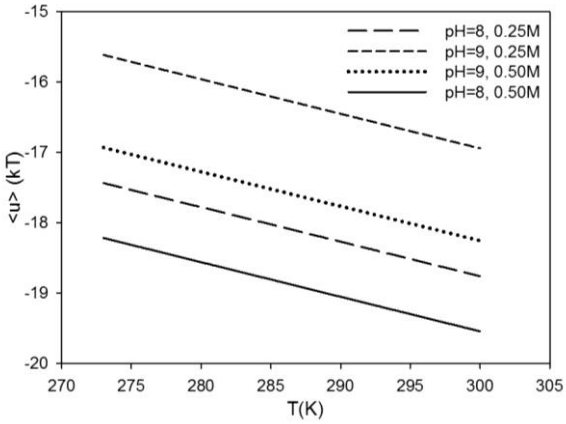

Figure 9. *Expected temperature dependence of total interaction energy. The lines show predicted variation of the total interaction energy as function of the temperature at different pH and salt concentrations. Predictions are based on comparison with Hepatitis B and analysis of pH dependence and ion strength dependence of the total interaction energy.*

Conclusion

In conclusion, our model has proven capable of most credibly modeling values for the interaction energies between capsomers of both Hepatitis B and the Norovirus. Prediction of the pH dependence is surprisingly accurate, considering the crudeness of the model, and there seems to be good accordance with experimental data obtained by Heck *et al.*, Zlotnick *et al.* and Wingfield *et al.* For the salt concentration dependence however we observed a deviation between experimental data and our theoretical prediction at low salt concentrations. This deviation is consistent for both viruses and multiple datasets. Given the accuracy of our model for the interaction energy as function of the pH, we believe this deviation to have a physical meaning. Charge renormalization cannot eliminate the differences. Likely there is an effect of charge regularization, but other possible explanations are the presence of small salt induced

conformational changes, an irregular charge screening effect originating from inhomogeneous protein charge distribution or the self-energy of the capsomers, that we have neglected so far.

References

1. *Are weak protein-protein interactions the general rule in capsid assembly.* Zlotnick, Adam. 2003, Virology, pp. 315;269-274.

2. *Hepatitis Core Antigen Produced in Escherichia coli: Subunit Composition, Conformational Analysis and In Vitro Capsid Assembly.* Wingfield, Paul T, *et al.*, *et al.* 1995, Biochemistry, pp. 34;4919-4932.

3. *Moving Towards High-Resolution Descriptions of the Molecular Interactions and Structural Rearrangements of the Human Hepatitis B Core Protein.* Ferguson, Neil, *et al.*, *et al.* 2008, J.Mol.Biol, pp. 384;1301-1313.

4. *Subunit exchange rates in Hepatitis B virus capsid are geometry- and temperature-dependent.* Uetrecht, Charlotte, *et al.*, *et al.* 2010, Phys Chem Chem Phys, pp. 12:13368-13371.

5. *Physical principles in the construction of regular viruses.* Kaspar, D.L.D. en Klug, A. 1962, Cold Spring Harb. Simp. Quant. Biol., pp. 27:1-24.

6. *Three-Dimensional Structure of Hepatitis B Virus Core Particles Determined by Electron Cryomicroscopy.* Crowther, R A, *et al.*, *et al.* 1994, Cell, pp. 77;943-950.

7. *The Crystal Structure of Human Hepatitis B Virus Capsid.* Wynne, S A, Crowther, R A en Leslie, A G. W. 1999, Molecular Cell, pp. 3;771-780.

8. *Electron microscopy of hepatitis B core antigen synthesized in E.coli.* Richmond, J E en Cohen, B J. 1982, Nature, pp. 296;677-679.

9. *Hepatitis B virus nucleocapsid assembly: primary structure requirements in the core protein.* Birnbaum, F en Nassal, M. 1990, J. Virol., pp. 64;3319-3330.

10. *Weak Protein-Protein Interactions Are Sufficient To Drive Assembly of Hepatitis B Virus Capsids.* Zlotnick, Adam en Ceres, Pablo. 2002, Biochemistry, pp. 41;11525-11531.

11. *Competing Hydrophobic and Screened-Coulomb Interactions in Hepatitis B Virus Capsid Assembly.* Kegel, Willem K en van der Schoot, Paul. sl : Biophysical Journal, 2004, Biophysical Journal, pp. 86: 3905–3913.

12. *Physical Regulation of the Self-Assembly of Tobacco Mosaic Virus Coat Protein.* Kegel, Willem K en van der Schoot, Paul. 2006, Biophysical Journal, pp. 91: 1501–1512.

13. *X-ray Crystallographic Structure of the Norwalk Virus Capsid.* Venkataram Prasad, B V, *et al.*, *et al.* 1999, Science, pp. 286, 287–290.

14. *Norwalk Virus Assembly and Stability Monitored by Mass Spectrometry.* Shoemaker, Glen K, *et al.*, *et al.* 2010, Molecular & Cellular Proteomics, pp. 9:1742–1751.

15. *Isoelectric point determination of norovirus virus-like particles by capillary isoelectric focusing with whole column imaging detection.* Goodridge, L, *et al.*, *et al.* 2004, Anal. Chem., pp. 1;76(1):48-52.

16. *Comparison of the Antigenicity and Protein Composition of Hepatitis B Virus e Antigen Subtypes HbeAg/1 and HbeAg/2.* Yamada, Ei, Ishida, Nakao en Ohori, Hitoshi. 1982, J.gen.Virol, pp. 64;895-903.

17. *Some properties of hepatitis B core antigen isolated from serum of infected humans.* Neurath, A R, Huang, S N en Strick, N. 1978, J.gen.Virol, pp. 39;91-101.

18. *The Structure of Hepadnaviral Core Antigens.* Zheng, Jian, Schödel, Florian en Peterson, Darell L. 1992, Journal of Biological Chemistry, pp. 267:9422-9429.

19. *Average protein density is a molecular-weight-dependent function.* Fischer, Hannes, Polikarpov, Igor en Craievich, Aldo F. 2004, Protein Science, pp. 13, 2825-2828.

20. *Conformational Stability and Disassembly of Norwalk.* Salvador, Ausar F, *et al.*, *et al.* 2006, JOURNAL OF BIOLOGICAL CHEMISTRY, pp. VOL. 281, NO. 28, pp. 19478–19488.

21. *Size and mechanical stability of norovirus capsids depend on pH: a nanoindentation study.* Cuellar, J L, *et al.*, *et al.* 2010, Journal of General Virology, pp. 91, 2449–2456.

22. *Alexander's prescription for colloidal charge renormalization.* Trizac, E, *et al.*, *et al.* 2003, Langmuir, pp. 19:4027-4033.

1.2 Influence of salt specific effects on Norovirus capsid assembly

In the first part of this chapter the salt concentration dependence of the interaction energy between Norovirus coat proteins was discussed and although the predicted interaction strengths were in the right ballpark, the experimentally observed repulsion was always weaker than the predicted one. This effect was most pronounced at both low and very high salt concentrations. At intermediate ion strength good correspondence between model and experiments was found. Charge renormalization was briefly discussed as a possible solution to explain the discrepancy at low salt concentration. A second effect that could play a part in understanding the difference in measurements and calculations, especially for higher salt concentrations are salt specific effects. In our model we assumed that the hydrophobic attraction energy is constant for the salt concentration, but this assumption might fail at higher salt concentrations.
There is abundant literature that reports that ions affect the surface tension between water and organic solvents or air [1] and recently this has also been shown for the surface tension between water and biopolymers [2,3]. Pegram and Record (2007) [4] listed some surface tension increments (STI) values for different salts. This allows us to semi-quantitatively describe the salt concentration dependence of hydrophobic attraction energy. For HBV at (near)physiological conditions, however, these effects are negligible. That is on itself in good correspondence with the fact that experimental values for this virus capsid do show linear behavior, but it raises the question whether this effect can be present for NWV at comparable salt concentrations.

The difference between the two experiments is however the type of salt that is used. The salt concentration experiments for HBV were conducted in sodium chloride solution, where the NWV experiments were performed in ammonium acetate.

The Hoffmeister series predict that surface tension increments not only depend on salt concentration but also on the speciation and that ammonium acetate has a larger effect on the surface tension between water and biopolymers than sodium chloride [4]. The question remains whether this effect is strong enough to account for the results.

If we express the hydrophobic attraction energy as a function of constant hydrophobic surface and a salt concentration dependent surface tension, we get:

$$\mathrm{h}(c_s) = A_H * \gamma(c_s) \tag{8}$$

Taylor expanding the surface tension around a reference salt concentration and neglecting the higher order terms then gives:

$$\mathrm{h}(c_s) \cong A_H * \left[\gamma_0 + \frac{\partial \gamma}{\partial c_s} * (c_s - c_0)\right] \tag{9}$$

Then γ_0 is the surface tension between water and the hydrophobic surface of $VP1_2$ at a reference salt concentration c_0 and $\frac{\partial \gamma}{\partial c_s}$ is the surface tension increment (STI) in kT/nm^2 per molar. We used $A_H * \frac{\partial \gamma}{\partial c_s}$, the total change in hydrophobic attraction energy per unit of salt concentration as a fit parameter to fit the data. Results are shown in *Figure 10*.

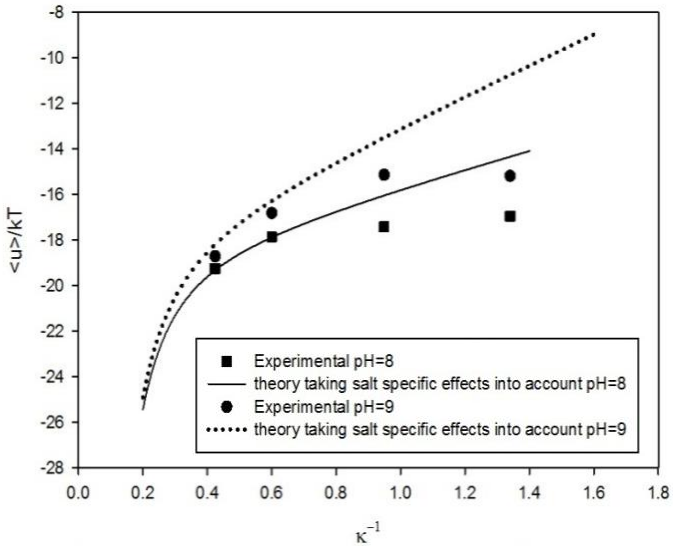

Figure 10. *A non-linear fit taking salt specific effects into account explains the experimental data at high salt concentrations. Surface tension increments multiplied by the hydrophobic surface area is used as a fit parameter and was found to be 2.98 kT/molar.*

The best fit was obtained for $A_H * \frac{\partial \gamma}{\partial c_s} = 2.98$ kT/molar. When we compare this to the total hydrophobic attraction energy of 20.27 kT. It seems quite a reasonable value. It means that one molar increase in salt concentration changes the hydrophobic attraction by around 14.7%.

This figure thus shows that salt specific effects can account for the high salt measurements (i.e. 0.5 M) but not for the observations at lower salt concentrations. In the previous section it was already shown that the surface charge is still above the renormalization limit, but since the trend is consistent over two pH values, we expect a physical meaning for the difference between measurements and theory. From Figure 6 we can see that the discrepancy between model and experimental data increases as the pH goes up and the salt concentration goes down. Hence it could be argued that the deviation is a consequence of processes related to charge regulation, that we have so far not taken into account. Another factor could be the contribution of different protein conformations.

References

1. Melander, W. Chromatography on Hydrophobic Interactions of Proteins : An Interpretation in Precipitation and of the Lyotropic Series ’. (1977).

2. Baldwin, R. L. How Hofmeister ion interactions affect protein stability. *Biophys. J.* **71,** 2056–63 (1996).

3. Zhang, Y. & Cremer, P. S. The inverse and direct Hofmeister series for lysozyme. *Proc. Natl. Acad. Sci. U. S. A.* **106,** 15249–53 (2009).

4. Pegram, L. M. *et al.* Why Hofmeister effects of many salts favor protein folding but not DNA helix formation. *Proc. Natl. Acad. Sci. U. S. A.* **107,** 7716–21 (2010).

1.3 Prediction of assembly energetics of Cowpea Chlorotic Mottle Virus and Brome Mosaic Virus capsids

Introduction

Next to the Norovirus, HBV also the Cowpea Chlorotic Mottle Virus (CCMV) and Brome Mosaic Virus (BMV) are constituted from protein building blocks that spontaneously self-assemble into hollow virus capsids in the absence of genetic material [4,5]. In fact CCMV is the first icosahedral virus for which in vitro self-assembly was demonstrated [1]. BMV and CCMV are very closely related as both are small icosahedral plant viruses with T=3 geometry. Also both viruses are slightly positively charged at neutral pH. The CCMV protein building block however shows rather rich phase behavior where the native BMV coat protein only exists in either free dimeric form or as capsids (a mutant lacking the N-terminal domain assembles into T=1 geometry)[6] (see Figure 11).

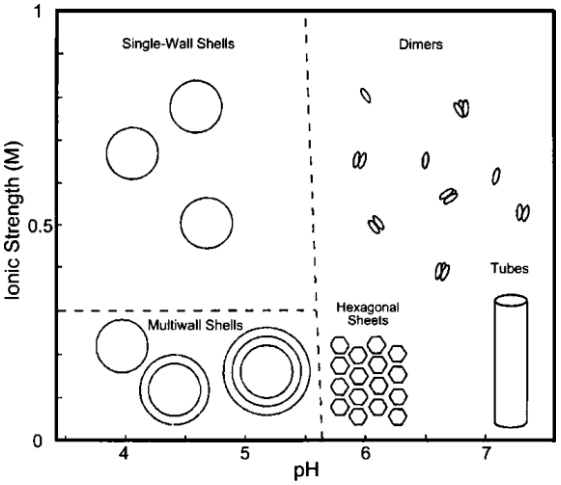

***Figure 11**. Phase diagram of CCMV capsid protein. Copied from [2]*

The majority of the studies on the self-assembly of CCMV were done in the presence of RNA. These studies show that RNA interacts with the positively charged N-terminal tail of the protein and thereby induces capsid formation. Yet recently *Willits et al*. designed a deletion mutant that self-assembles in absence of RNA [3]. This mutant CCMVΔβ27-35 lacks a specific β-barrel structure near the N-terminus. Since we are interested in describing viral self-assembly using a simple physical chemical model, we will attempt to understand the findings by Willits *et al*. So in this section we will use the models described earlier on to provide a theoretical pH titration of both the CCMV and BMV coat protein and compare the predicted interaction potential with experimental data on BMV.

Influence of pH on CCMV capsid formation

Figure 12 shows a theoretical pH-titration curve of CCMVΔβ27-35, calculated using equation 5 and the amino acid sequence. It shows that the pI lies near pH=10, indicating that the capsomers are indeed positively charged at neutral pH. This is different from other viruses we investigated, such as the Norovirus and Hepatitis B.

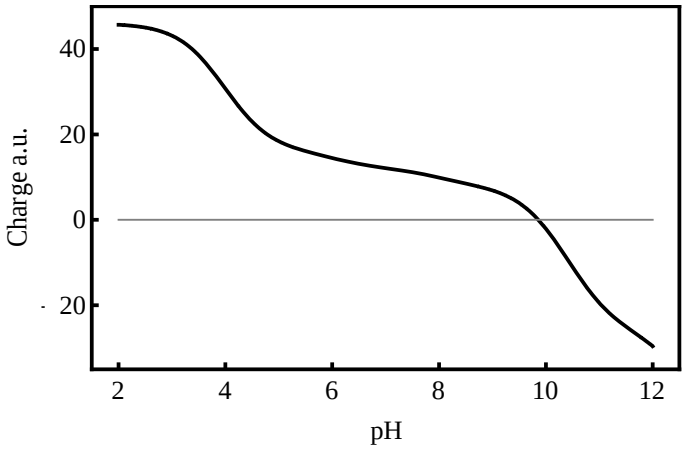

***Figure 12**. Theoretical pH titration curve of the deletion mutant of CCMV capsid protein, designed by Zlotnick et al. Based on this curve the protein would have a PZC of 10.*

Based on this theoretical pH titration curve, we make a prediction on the variation of the total interaction energy as function of the pH at different salt concentrations. For the hydrophobic attraction energy we use -19kT, the hydrophobic attraction of Hepatitis B. The prediction is shown in Figure 13.

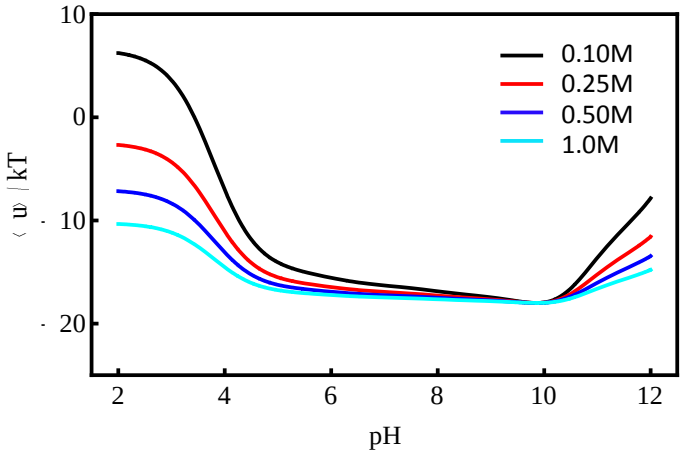

***Figure 13.** Prediction of the pH-dependency of the total interaction energy per capsomer at different salt concentrations. Notice the gentle slope between pH=5 and pH=10. Here deviations in pH should hardly effect the assembly equilibrium.*

Willits found that the CCMV mutant self-assembles at pH=4.5 and high salt concentration (i.e. 1.0 M). According to our prediction that corresponds to an interaction energy per subunit of around -17kT, enough to induce self-assembly. Based on *Figure 13*, we would also predict self-assembly at pH values up to 10. That is, if the protein itself is still stable at basic pH.

Influence of pH on BMV capsid formation

The assembly behavior of BMV is more straightforward than that of CCMV and the monomer and capsid concentrations were measured as function of pH and salt concentration by Jacrot *et al.* [5] rendering it an excellent system to test the predictive ability of the model on thermodynamics of virus assembly proposed by Kegel and Van der Schoot [7]. Using equation 5 and the amino acid sequence of the BMV coat protein we calculated a theoretical pH titration that is shown in Figure 14

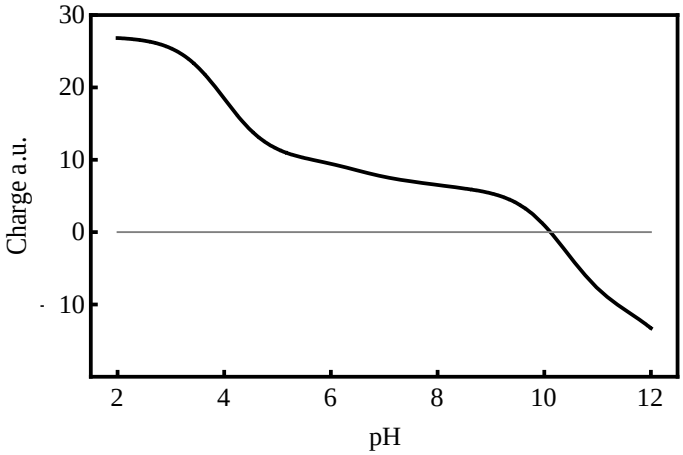

Figure 14. *Theoretical pH titration of the BMV virus capsid. Notice the similarity with the pH titration of CCMV. Both proteins are positively charged at neutral pH and the point of zero charge lies around pH=10.*

We assume a value of 19 kT at room temperature for the hydrophobic attraction, the same that was used for HBV and CCMV. The electrostatic surface area can be found to be 31.2 nm^2 by dividing the capsid surface by 90 (the number of protein dimers present in a T=3 capsid). Then we can predict the total interaction energy as function of pH and compare it with experimental data by Jacrot *et al.* at two different salt concentrations: 0.215 and 0.515 M of KCl. The result is shown in Figure 15.

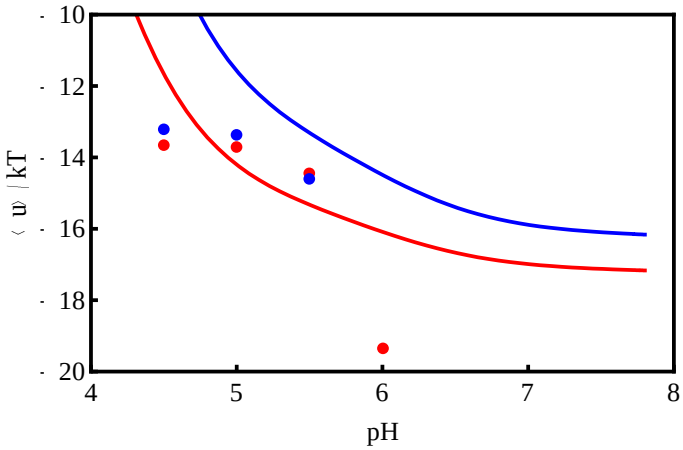

Figure 15. *Comparison between predicted (lines) and experimentally observed (dots) interaction energy of the BMV coat protein at 0.215 M (blue) and 0.515 M (red) KCl concentration. The interaction energy expected from the model is in the right ballpark, but does not show the same trend as the experimental data do.*

Notice that the overall predicted interaction energy is of the same order as the experimental values, but the trend is different. Where the model predicts interaction potential to become much weaker due to increased electrostatic repulsion below pH 4, the experiments suggest a plateau value is reached there. This discrepancy is a consequence of charge regularization that was not taken into account. That would also explain why the model predicts weaker interaction than observed from the experiment and why the difference in interaction energy between the two salt concentrations is larger for the model than for the experiments. So the proteins are likely less charged than the model predicts. The difference between data and model could also be due to the erroneous assumption of homogeneous charge distribution. In fact the charges are localized in positively and negatively charged patches on the proteins. Near the interaction area these patches could cause attraction when they are of opposite charge.

Comparison with other icosahedral viruses

It is interesting to note, that even though this virus is very different from Hepatitis B and Norovirus in a way that it carries a net positive charge rather than a negative one at neutral pH, the interaction energy landscape over different pH values is very similar. Based on that observation we would expect a similar charge density (albeit of opposite sign). Table 2 shows theoretical charge densities of Norovirus, Hepatitis B, CCMV and BMV at different pH values.

Table 2. *Surface charge in unit charges per squared nanometer of CCMV, HBV and NWV for neutral and basic pH.*

	CCMVΔβ27-35	**HBV**	**NWV**	**BMV**
pH=7	0.21	-0.21	-0.13	0.24
pH=9	0.12	-0.29	-0.29	0.17

The fact that CCMV and BVM have a pI of around 10 and thus carry a net positive charge at neutral pH, makes them interesting virus capsids to investigate. For both the Norovirus and Hepatitis B capsid protein, studies show that the capsids are stable at relatively acidic pH, deep below the pI of those proteins. This indicates a hysteresis effect. Yet oddly, above the PZC of both proteins, the capsids started to disassembly according to our model. From a purely physical point of view one would expect electrostatic repulsion to be independent of the sign of the charge, raising the question what causes the hysteresis at lower pH. Investigation of the CCMV virus capsid and comparison with Norovirus and Hepatitis B might help to explain this paradox.

References

1. Adolph, K. W. & Butler, P. J. Assembly of a spherical plant virus. *Philos. Trans. R. Soc. Lond. B. Biol. Sci.* **276,** 113–22 (1976).

2. Lavelle, L. *et al.* Phase diagram of self-assembled viral capsid protein polymorphs. *J. Phys. Chem. B* **113,** 3813–9 (2009).

3. Willits, D. *et al.* Effects of the cowpea chlorotic mottle bromovirus beta-hexamer structure on virion assembly. *Virology* **306,** 280–8 (2003).

4. Chen, C., Kao, C. C. & Dragnea, B. Self-assembly of brome mosaic virus capsids: insights from shorter time-scale experiments. *J. Phys. Chem. A* **112,** 9405–12 (2008).

5. Cuillel, M., Zulauf, M. & Jacrot, B. Self-assembly of brome mosaic virus protein into capsids: Initial and final states of aggregation. *J. Mol. Biol.* **72,** 63–72 (1983).

6. Cuillel, M., Jacrot, B. & Zulauf, M. AT= 1 capsid formed by protein of brome mosaic virus in the presence of trypsin. *Virology* **276,** (1981).

7. Kegel, W. K. & Schoot Pv, P. Van Der. Competing hydrophobic and screened-coulomb interactions in hepatitis B virus capsid assembly. *Biophys. J.* **86,** 3905–13 (2004).

Appendix A

We are looking for an expression that describes the charge of a protein as function of the pH. The charge originates form ionized basic or acidic amino acids. If we assume the general equilibrium between ionized and non-ionized acidic amino acids, we get:

$$[HA] \leftrightarrow [H^+] + [A^-]$$

Then the Henderson Hasselbalch equation gives:

$$K = \frac{[H^+] * [A^-]}{[HA]}$$

Taking the logarithm of both sides gives

$$pKa = pH - \log\left(\frac{[A^-]}{[HA]}\right)$$
$$10^{-pKa+pH} = \frac{[A^-]}{[HA]}$$
$$10^{-pKa+pH} * [AH] = [A^-]$$

Subtracting and adding $[A^-]$ on the left-hand side gives

$$10^{-pKa+pH}([AH] + [A^-]) - 10^{-pKa+pH}[A^-] = [A^-]$$
$$10^{-pKa+pH} * \frac{[AH] + [A^-]}{[A^-]} - 10^{-pKa+pH} = 1$$
$$\frac{[AH] + [A^-]}{[A^-]} - 1 = 10^{pKa-pH}$$
$$\frac{[AH] + [A^-]}{[A^-]} = 10^{pKa-pH} + 1$$

Now defining the number of charges originating from amino acid i , z_i, as the percentage of this amino acid that is ionized times its number gives

$$z_i = n_{a,i} * \frac{[A^-]}{[AH] + [A^-]}$$

Where $n_{a,i}$ is the number of acidic amino acids of type i. Filling this in in the modified Henderson Hasselbalch equation then gives

$$z_i = \frac{n_{a,i}}{1 + 10^{pKa-pH}}$$

For basic amino acids of type j we analogously find:

$$z_j = \frac{n_{b,j}}{1 + 10^{pH-pKa}}$$

The protein charge z is the sum of the charges originating from all types of ionizable amino acids and considering that acidic amino acids provide negative charges and basic amino acids provide positive charges , we find equation 5:

$$z = -\sum_{i=1}^{a} \frac{n_{a,i}}{1 + 10^{pKa - pH}} + \sum_{j=1}^{b} \frac{n_{b,j}}{1 + 10^{pH - pKa}}$$

a being the number of types of acidic amino acids and b being the number of types of basic amino acids.

Appendix B

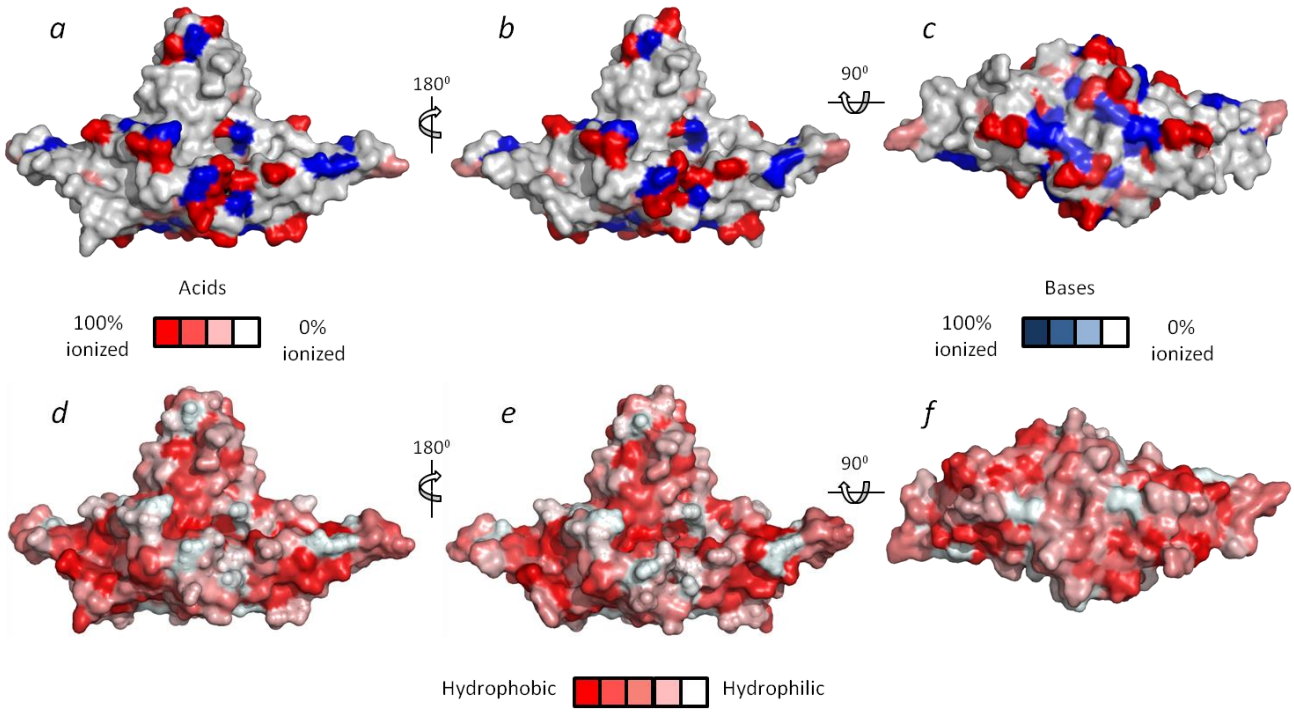

Figure 16. *Chemical nature of HBV capsid protein surface. Figure a, b and c show the distribution of ionizable amino acids. The colors indicate what percentage of the time amino acids is ionized at neutral pH based on their average pKa values. Aspartic acids and glutamic acids are colored dark red, cysteines are slightly lighter red and tyrosines are shown in salmon. As regards the basic residues, lysines and arginines are dark blue and histidines are lightblue. Non-ioniziable amino acids are white. This gives an indication of how the charges are distribute d over the protein. Figures d, e and f show the hydrophobic surface of Hepatitis B. Hydrophobicity was calculated using the Heisenberg Hydrophobicity scale (Heisenberg et al., 1984). Red indicates a hydrophobic region and white a hydrophilic region. One can see that four the interacting regions (left and right bottom of both molecules) do indeed show increased hydrophobicity. One can also see that the charge is more or less evenly distributed over the protein, although the hydrophobic patches show decreased charge density. Both figures are based on the X-ray structure of dimeric HbeAg, crystallized as part of capsids, by Bourne and Zlotnick, 2006*

Appendix C

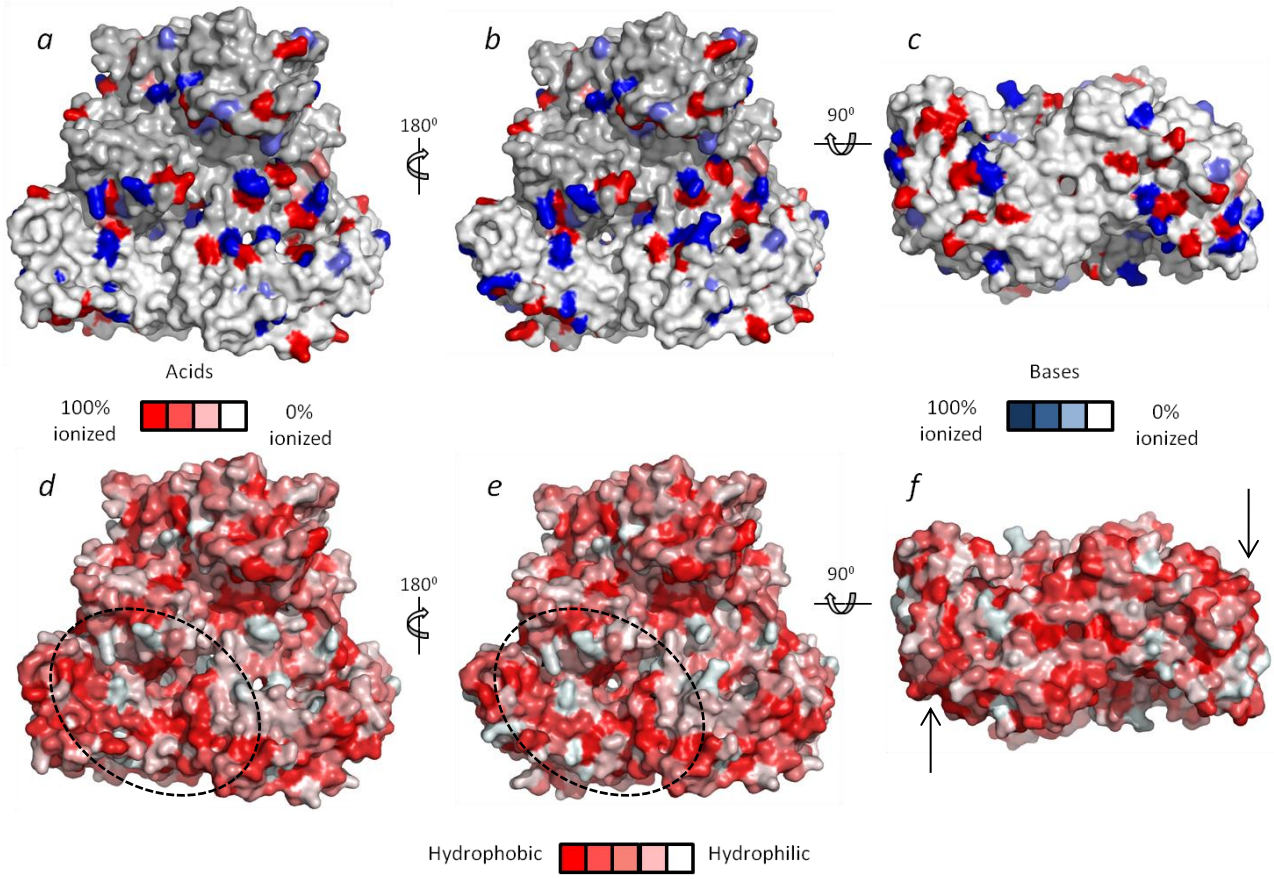

Figure 17. *Charge distribution and hydrophobic residues of Norovirus capsid protein surface. All pictures are based on the X-ray structure of $VP1_2$ crystallized in capsids by Prasad et al., 1999. The protrusion domain is shown in grey and the shell domain in white. Figure a, b and c show the distribution of ionizable amino acids. The colors indicate what percentage of the time amino acids is ionized at neutral pH based on their average pKa values. Aspartic acids and Glutamic acids are colored dark red, cysteines are slightly lighter red and tyrosines are shown in salmon. As regards the basic residues, lysines and arginines are dark blue and histidines are lightblue. Non-ioniziable amino acids are white or grey. The figures show that the charges are relatively evenly distributed over the protein.*
Figure d, e and f show the hydrophobic surface of $VP1_2$. The hydrophobicity was calculated using Heisenbergs hydrophobicity scale (Heisenberg et al., 1984). There are four interaction patches on each dimer, indicated by the dotted circles and arrows that do not seem to be more hydrophobic than the rest of the protein, but one can argue they are slightly less charged. Note also the high amount of symmetry in the dimer.

Part 2

Virus capsid polymorphism

With a physical description of assembly-behavior in hand, we aim for the explanation of virus capsid polymorphism, the property of viruses to assemble in multiple types of capsids of different sizes. We propose two models to account for the observed capsid polymorphism of HBV, one based on assembly kinetics and one based on equilibrium thermodynamics. Both require the addition of a curvature free energy term to the interaction potential. We propose to take curvature into account as a continuum elastics term, analogous to Helfrichs curvature free energy. Furthermore we make the connection between the preferred curvature as parameter for the curvature free energy term and the structure of the protein building blocks. As an alternative approach to consider curvature effects we provide a model to relate the interaction angle of rigid subunits in icosahedral symmetry to the equilibrium energy of the structure.

2.1 Kinetics versus thermodynamics in virus capsid polymorphism

Virus capsid proteins spontaneously self-assemble into hollow shells under the right conditions driven by an interaction energy of the order of 10 kT, consisting of a short range attraction balanced by an electrostatic repulsion. In this regime of soft interactions it is subject to debate whether the properties of the assembly process are dominated by kinetics or by thermodynamics. Here we account for the observed virus capsid polymorphism of Hepatitis B both from the perspective of assembly rates and equilibrium energies by adding a curvature free energy term to the interaction potential. From these models we propose experiments that may conclusively distinguish between kinetically and thermodynamically governed polymorphism.

The genetic material of viruses is protected by a protein shell called virus capsid. In absence of viral RNA, the protein building blocks of amongst others HBV, CCMV and the Norovirus can under the right conditions self-assemble into hollow capsids [1–5]. In recent years interest in these virus capsid has increased for their potential application as drug delivery systems [6,7], for which a comprehensive understanding of self-assembly process is pivotal. A main unresolved question concerns the origin of polymorphism, the property of viruses to display multiple capsid sizes. An indication that protein structure is not the only determinant of capsid size and geometry is given by the observation of different capsid sizes, built from the same building block [2,3,8,9]. Generally only one of the observed capsid sizes is infectious, indicating also the medical relevance of this study.

A well investigated example of this structural dimorphism is shown by Hepatitis B (HBV), an enveloped icosahedral virus that causes infectious liver inflammation. The (dimeric) HBV capsid protein mutant $Cp149_2$ was shown to spontaneously form hollow virus capsids under the right conditions (i.e. near-neutral pH and medium to high salt concentrations) [1,8,10]. Interestingly HBV capsids occur both in T=4 and T=3 geometry in a ratio of about 95:5 almost independent of conditions [8,11]. The successful description of interaction energies that account for the equilibrium between HBV capsid and monomer [12], suggests that a similar coarse-grained model could be used to describe polymorphism.

These interaction energies that drive the aggregation process are in the order of 10 kT [1,12]. This regime of soft interactions is interesting from a fundamental point of view in the sense that it is not a priori clear whether structure formation is dominated by kinetics (as for chemical reactions with energies in the order of 100kT) or by thermodynamics (as is the case for amongst others gas-liquid transitions with energies in the order of 1kT). In general, one can state that the relative abundance of different capsid sizes is governed either by their equilibrium energy – when all reactions are reversible and the system is in thermodynamic equilibrium – or by their respective rates of formation – if polymorphism is the consequence of a kinetic trap.

In this paper we provide theoretical considerations on the origin of structural dimorphism of icosahedral viruses and address the fundamental question whether dimorphism is the consequence of the thermodynamics or the kinetics of virus capsid self-assembly. Therefore we will propose two models, one based on nucleation kinetics, and one based on equilibrium thermodynamics that could explain the presence of structural dimorphism. We will compare them with the experimentally observed polymorphism of HBV and propose testable hypotheses that can conclusively distinguish between the two regimes.

Consider an equilibrium aggregation process where monomers attach to incomplete capsids of different sizes.

$$nA \leftrightarrow A_n \qquad (1)$$

Where n represents the number of capsomers present in a completed capsid of a certain size. We assume reversible assembly to prevent formation of kinetically trapped assembly intermediates, combined with strong hysteresis [13] so that disassembly of complete capsids and concomitant equilibration is prohibited. This assumption is ratified by the observation of subunit exchange times in the order of months [9]. The relative

number densities of the two capsid sizes will then only be determined by their respective time dependent rates of formation, $J_p(t)$ and $J_q(t)$ where p and q are the allowed capsid sizes. Previous studies show that viral assembly is characterized by a sigmoidal increase of capsid density with time [14,15]. This can, using classical nucleation theory, approximately be described by a steady-state reaction rate J^0 after a lag time t_0 such that there will be a linear increase in capsid concentration until the number of monomers drops below the critical value (that resembles a critical micelle concentration) and the self-assembly stops [16]. Since we assumed that no disassembly can take place once the capsid is formed and the ratio between two different sizes of capsids at any time after assembly is given by

$$\frac{\rho_{T=4}(\infty)}{\rho_{T=3}(\infty)} = \frac{J^0_{T=4} * \left(t_t - t_{0,p}\right)}{J^0_{T=3} * \left(t_t - t_{0,q}\right)} \sim \frac{J^0_{T=4}}{J^0_{T=3}} \qquad (2)$$

Where in the last step we use the fact that the difference between lag times $t_{0,p}$ and $t_{0,q}$ is small compared to the termination time t_t, where the monomer concentration drops below the cmc. According to classical nucleation theory of virus capsids [17] the steady state assembly rate is given by

$$J^0 = \nu Z e^{-\Delta G} \qquad (3)$$

where ν is the attempt frequency, a measure for the interaction rate of the monomers with an incomplete assembly, Z is the Zeldovich factor that accounts for the time the incomplete aggregates survive without disassembling and ΔG is the free energy of nucleation scaled to thermal energy. We assume that the attempt frequency is independent of capsid size, so that it does not influence the ratio at which the capsids are formed, which is in accordance with a reaction limited assembly process. Expressions for the Zeldovich factor and the nucleation energy are given below.

$$Z = \sqrt{\frac{a}{n\pi}}(1 + \Gamma^2)^{3/4} \qquad (4)$$

$$\Delta G = \frac{n * a}{2}\left(\sqrt{\Gamma^2 + 1} - \Gamma\right) \qquad (5)$$

Here Γ is a measure of the supersaturation that drives the capsid assembly and *a* represents the rim energy that determines the nucleation barrier height in units kT. They are given by the following equations

$$\Gamma_n = \sqrt{n-1}\left(1 - \frac{\ln(\varphi)}{\ln(\varphi_c)}\right) \qquad (6)$$

$$a_n = -\frac{\Delta g}{\sqrt{n-1}} \qquad (7)$$

where Δg is the interaction energy per bond in units of thermal energy. So from a kinetics perspective it is the interplay between the supersaturation favoring the formation of large capsids and the nucleation barrier favoring the formation of small capsids, that determines the different rates of formation and thus the dimorphism.

Now it is insightful to investigate the two typical limits of high concentration, where the supersaturation dominates, and low concentration, where the energy barrier dominates the polymorphism. At this point we take identical interaction energies for proteins assembling into a T=4 capsid as for proteins assembling into a T=3 capsid. At very low supersaturation Γ→0 and the ratio $\frac{\rho_{T=4}}{\rho_{T=3}}$ simplifies to $Exp\left[-\frac{1}{2}|\Delta g| * \left(\sqrt{n_{T=4}-1} - \sqrt{n_{T=3}-1}\right)\right]$. In this limit the ratio between T=4 and T=3 capsids will always be (much) smaller than 1, so indeed T=3 capsids are favored. When Γ>>1 the ratio between T=4 and T=3 capsids simplifies to 1 independent of conditions. So the larger capsid is always disfavored and at best equally abundant as the smaller one.

Alternatively we can assume complete reversibility, so that the obtained dimorphism is determined by the equilibrium energies of the respective assemblies rather than their assembly rates. For an ideal dilute solution, the capsid mole fraction x_n is then given by

$$x_n = x_1^n exp[-(\Delta\mu_n)/kT] \qquad (8)$$

With x_1 is the mole fraction of free capsomer and $\Delta\mu_n = \mu_n^0 - n\mu_1^0$ is the difference in free energy

between free monomers and monomers absorbed into an aggregate. This energy difference corresponds to n times the (negative) interaction energy per capsomer ε_n. The total mole fraction of monomer x is the sum of the mole fractions of free and absorbed monomers $x = \sum_j \nu_j x_j$ (conservation of mass). Combining this with equation 8 and expressing the energy difference in terms of interaction energy per capsomer, gives

$$x = x_1 + p x_1^p exp[-p\varepsilon_p] + q x_1^q exp[-q\varepsilon_q] \quad (9)$$

The interaction free energy per capsomer ε is built up from three terms, the hydrophobic attraction and electrostatic repulsion that have been previously described by Kegel and Van der Schoot and an energy term related to the curvature of the virus capsids. So in general

$$\varepsilon = \varepsilon_H(T) + \varepsilon_E(pH, c_s) + \varepsilon_C(n) \quad (10)$$

Where ε_H(T) is the temperature dependent hydrophobic attraction, ε_E is the electrostatic repulsion and ε_C the curvature energy, all in units of kT per capsomer. When we now consider equal interaction energies for the T=3 and T=4 capsid analogous to our kinetic model – so $\varepsilon_C(n) = 0$ – we find that again the smaller capsid is favored, this time for entropic reasons, as is shown in *Figure 19*. This is inconsistent with numerous observations that for various mutants of the HBV capsid protein, under a large set of conditions, the larger capsid is found to be most abundant [1,9,18]. So clearly the effective interaction energies between proteins absorbed in capsids of different sizes are actually unequal. This is intuitively evident from the fact that different capsids have different geometries so that the local interactions are indeed expected to vary [19,20]. It is however subject to debate whether the origin for this variation in effective interaction energy is related to interaction angles that affect the effective hydrophobic attraction, whether it is due to different protein conformations that are not equally energetically favorable, or that it is the consequence of the bending rigidity of the curved protein sheet. Although one can argue that all are merely different levels of description of an equivalent principle, we will not elaborate on the physical nature of the size dependent energy, but just note that it is reasonable to introduce a curvature free energy term to the free energy of interaction for which we propose the following Ansatz

$$\varepsilon_C(n) = \kappa' \left(\sqrt{\frac{n}{n_0}} - 1 \right)^2 \quad (11)$$

where n0 is a measure of the preference curvature and *κ'* is a stress constant related to the protein bending rigidity that sets the energy scale for the penalty related to deviation from preference curvature, see Figure 18. The harmonic spring character of this curvature free energy makes it general and rigorous in a way that it does not consider the source of the curvature stress. It can be shown to be isomorphic to the rotational and translational invariant curvature free energy deduced by Helfrich that for spherical particles corresponds to

$$F_c = 4\pi R^2 \left(\frac{\kappa}{2} \left(\frac{2}{R} - \frac{2}{R_0} \right)^2 + \frac{\bar{\kappa}}{R^2} \right) \quad (12)$$

where the first term accounts for the mean curvature and the second term for the Gaussian curvature with concomitant bending elastic modulus κ and Gaussian modulus $\bar{\kappa}$. Here 1/R represents the capsid curvature and $1/R_0$ is the reference curvature. Our stress constant *κ'* then equals 8πκ.

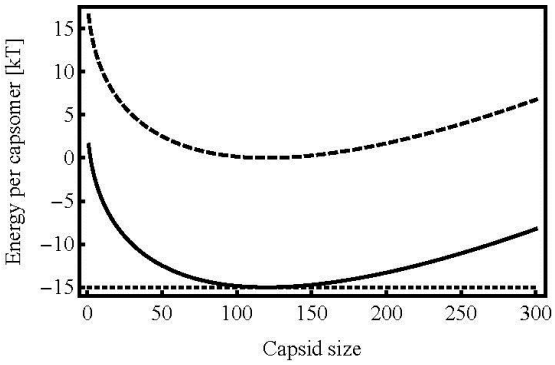

Figure 18. *The total energy gain per capsomer upon binding (continuous) is the sum of the capsid size independent interaction energy (dotted) and the size dependent curvature free energy (dashed). Here $\varepsilon_E+\varepsilon_H$=-15 kT, κ=20 kT and n0=120.*

Again we apply both models to the specific case of HBV at the same conditions at which Zlotnick *et al.* performed experiments [10] (i.e. pH=7.5 and 0.8 M NaCl) this time taking our Ansatz for the curvature

free energy into account. We assume that n_0 is 120 based on the experimental observation that the 120 capsomer containing T=4 capsid is the most abundant aggregate. We used the stress constant κ' as a fit parameter to obtain the expected T=4/T=3 ratio of 95:5 (=19:1) similar to the analysis by Šiber [21]. We found that in the thermodynamic model the curvature free energy of a single dimer absorbed in a T=3 capsid must be of the order of $5\,kT * \left(\sqrt{\frac{90}{120}} - 1\right)^2 = 0.09\,kT$ under the described conditions. For the kinetic model it is of the order of 0.32kT. It would indeed be expected that the curvature energy is small with respect to the interaction energy (of 10-20kT) since Kegel and Van der Schoot managed to describe the effect of experimental conditions on the interaction energy while completely neglecting the effect of curvature [12]. So conveniently the curvature energy term can be added to the hydrophobic attraction and the electrostatic repulsion terms in order to account for the observed dimorphism without significantly affecting the total interaction energy (the critical capsid concentration for T=3 capsids shifts about 8%).

Figure 19 shows the fits of the thermodynamic and the kinetic model to the experimental data by Zlotnick *et al.* who measured the concentration dependence of the fraction T=4 capsids at three different concentrations: 24 μM, 118 μM and 294 μM [11]. He found 95% of T=4 capsid using electron microscopy and 80% of T=4 by sucrose gradient ultracentrifugation. We take the value of 95% to be true since this was reproduced by other studies [8,15]. Zlotnick found this same fraction for all the concentrations so he concluded that HBV dimorphism is concentration independent. We however predict very slight concentration dependences that interestingly go in the opposite direction for both models, which allows us to propose an experiment that can conclusively distinguish between kinetically and thermodynamically governed polymorphism.

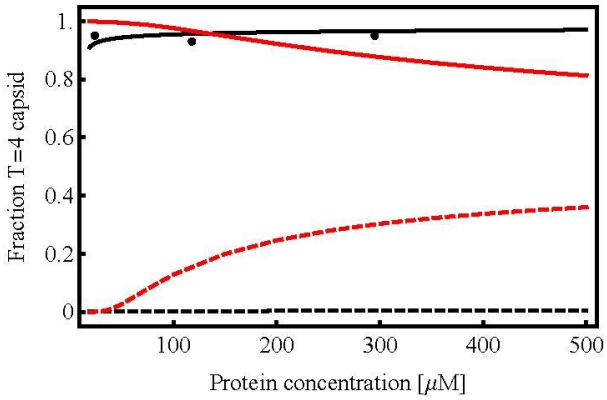

Figure 19. *Fraction of the T=4 capsid with respect to the total number of capsids as function of protein concentration in a system where only T=3 and T=4 capsids and monomers are allowed. The dashed lines represent predictions based on thermodynamic equilibrium (black) and assembly kinetics (red) with $\Delta g_{T=3}=\Delta g_{T=4}$=-15kT. Under these conditions the smaller capsid is more abundant because it is entropically favored. Circles represent the experimental data by Zlotnick et al [11]. The continuous lines are fits of the kinetic (red) and thermodynamic (black) model to the data using stress constant κ'. For the thermodynamic model κ'=4.7kT and for the kinetic model κ'=20kT. In both cases n0=120.*

The concentration dependence is explicit in the kinetic model because reaction rates depend on supersaturation. At higher concentrations, the contribution of the supersaturation will dominate with respect to the rim tension and both capsid sizes will form at more or less equal reaction rates. So if virus capsid polymorphism is the consequence of nucleation kinetics, the number of T=3 capsids will increase towards 50% at very high concentrations. In the case of HBV about 40% of the capsids should be T=3 at 1 mM dimer concentration.

In the thermodynamic model the concentration dependence is implicit and comes in via de x_1^p term. Critical micelle theory dictates that when the total concentration is lower than or of the same order of magnitude as the critical capsid concentration an increase in total capsomer concentration leads to an increase in free dimer concentration. The T=4 capsid concentration scales with x_1^{120} and the T=3 capsid concentration only with x_1^{90} (see equation 8). So in this case one would expect a larger fraction of T=4 capsids at higher protein concentrations. Although this effect will very mild, the concentration dependence should be fairly independent of the stress constant and preference curvature because it is purely entropic in nature.

The effect will also be stronger for dimorphism between T=3 and T=1 capsids (with a difference of 60 capsomers) than for T=4 and T=3 (with a difference of 30 capsomers).

In the models described above we assumed equilibrium interactions and ignored all atomistic effects of the protein subunits. As a consequence there is a priori no reason that $Cp149_2$ should only be able to form T=3 and T=4 capsids and no larger or smaller capsids. So if capsid polymorphism is indeed solely the consequence of these coarse entropy and curvature effects, the same energy terms should be able to account for the absence of other capsid sizes. When only taking icosahedral geometry into consideration other possible capsid sizes are T=1 (containing 30 dimers) and T=7 (containing 210 dimers). Smaller than T=1 is not possible and we ignore capsids even larger than T=7. Using the thermodynamic model with the same value for the curvature energy as used before, we found that indeed the T=4 capsids are 10^9 times more abundant than T=1 capsids and even 10^{59} times more abundant than T=7 capsids which is in excellent agreement with the fact that these capsid sizes have never been observed for Hepatitis B. Based on the kinetic model these effects are less pronounced, but still up to 2 mM no T=1 or T=7 capsids should be observed. At 3 mM dimer concentration however, one would expect measurable quantities of T=7 HBV capsids. This observation would be a strong indication that HBV capsid polymorphism is governed by reaction rates instead of equilibrium energies.

Another parameter that can be tuned to vary the relative abundance of different capsid sizes is the preference curvature n_0. Changing the shape of the protein would lead to a different preference curvature and hence a different ratio between T=3 and T=4 capsids. Zlotnick *et al.* found that this is indeed the case. They systematically removed residues of the C-terminus of the HBV capsid protein, forming protein structures that he called Cp147 (lacking 2 residues), Cp144 (lacking 5 residues etc.), Cp142, Cp140 and Cp138 [11]. He found that by decreasing the c-terminal taillength, the number density of T=3 capsids increased at the expense of T=4 capsids. So apparently by varying tail length, he tuned the preference curvature. We can understand this at least qualitatively if we compare capsid formation with micellization. Long fatty acid tails lead to larger micelles (or even bilayers) because the aspect ratio between headgroup and tail is decreased and hence the preference curvature is increased. Similarly the C-terminal tail of the capsid protein can also affect the preference curvature of the capsomer if it causes steric hindrance upon capsid formation. This leads to the interesting and testable hypothesis that the addition of an uncharged, hydrophilic amino acid to the c-terminal tail will shift the preferred capsid size towards larger T-numbers, independent of the chemical nature of the amino acid – serine, threonine, alanine, proline and glycine should give roughly the same effect, as long as the tail remains unstructured and does not interfere with the hydrophobic and electrostatic interactions. Figure 20 predicts the variation of capsid polymorphism with HBV protein length based on the ratio between the protein core and tail size. Fitting the prediction to the data shows that increasing the tail length of Cp149 by 80 amino acids should lead to the formation of observable quantities of T=7 capsids.

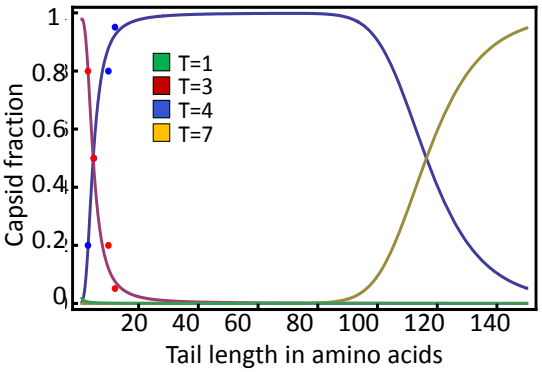

Figure 20. *Variation of preferred capsid size protein length for HBV capsid protein. Green, red, blue and yellow line represent T=1, T=3, T=4 and T=7 capsids respectively. The red (T=3) and blue (T=4) dots represent experimentally determined capsid cocentrations by Zlotnick et al. [11]. A core length of 127 amino acids was used based on the crystal structure [22]. An addition of 80-90 amino acids to the c-terminal tail of the Cp149 protein would lead to the formation of measurable quantities of T=7 capsids.*

So by adding a single curvature free energy term to the interaction potential we can quantitatively account for the observed virus capsid dimorphism of HBV and explain the absence of larger and smaller virus capsid sizes. We applied this curvature term to both a kinetic and a thermodynamic model and find measurements at

dimer concentrations of around 1mM can conclusively reveal which effect is dominant.

References

1. Ceres P, Zlotnick A. Weak Protein-Protein Interactions Are Sufficient To Drive Assembly of Hepatitis. 2002;4(13):11525–11531.

2. Shoemaker GK, van Duijn E, Crawford SE, et al. Norwalk virus assembly and stability monitored by mass spectrometry. *Mol. Cell. Proteomics*. 2010;9(8):1742–51.

3. Lavelle L, Gingery M, Phillips M, et al. Phase diagram of self-assembled viral capsid protein polymorphs. *J. Phys. Chem. B*. 2009;113(12):3813–9.

4. Gross I, Hohenberg H, Kräusslich HG. In vitro assembly properties of purified bacterially expressed capsid proteins of human immunodeficiency virus. *Eur. J. Biochem.* 1997;249(2):592–600.

5. States F. Self-assembly of Brome Mosaic Virus Protein Initial and Final States of Aggregation Into Capsids. 1977:589–603.

6. Wu W, Hsiao SC, Carrico ZM, Francis MB. Genome-Free Viral Capsids as Multivalent Cariers for Taxol Delivery. 2010;48(50):9493–9497.

7. Dasa SSK, Jin Q, Chen C-T, Chen L. Target-specific copper hybrid T7 phage particles. *Langmuir*. 2012;28(50):17372–80.

8. Wingfield PT, Stahl SJ, Williams RW, Steven a C. Hepatitis core antigen produced in Escherichia coli: subunit composition, conformational analysis, and in vitro capsid assembly. *Biochemistry*. 1995;34(15):4919–32.

9. Heck AJR. Subunit exchange rates in Hepatitis B virus capsids are geometry- and temperature-dependent. 2010;12(41):13368–13371.

10. Freund SM V, Johnson CM, Jaulent AM, Ferguson N. Moving towards high-resolution descriptions of the molecular interactions and structural rearrangements of the human hepatitis B core protein. *J. Mol. Biol.* 2008;384(5):1301–13.

11. Zlotnick a, Cheng N, Conway JF, et al. Dimorphism of hepatitis B virus capsids is strongly influenced by the C-terminus of the capsid protein. *Biochemistry*. 1996;35(23):7412–21.

12. Kegel WK, Schoot Pv P Van Der. Competing hydrophobic and screened-coulomb interactions in hepatitis B virus capsid assembly. *Biophys. J.* 2004;86(6):3905–13.

13. Singh S, Zlotnick A. Observed hysteresis of virus capsid disassembly is implicit in kinetic models of assembly. *J. Biol. Chem.* 2003;278(20):18249–55.

14. Chen C, Kao CC, Dragnea B. Self-assembly of brome mosaic virus capsids: insights from shorter time-scale experiments. *J. Phys. Chem. A*. 2008;112(39):9405–12.

15. Zlotnick a, Johnson JM, Wingfield PW, Stahl SJ, Endres D. A theoretical model successfully identifies features of hepatitis B virus capsid assembly. *Biochemistry*. 1999;38(44):14644–52.

16. Van der Schoot P, Zandi R. Kinetic theory of virus capsid assembly. *Phys. Biol.* 2007;4(4):296–304.

17. Zandi R, van der Schoot P, Reguera D, Kegel W, Reiss H. Classical nucleation theory of virus capsids. *Biophys. J.* 2006;90(6):1939–48.

18. Newman M, Suk F, Cajimat M, Chua PK. Stability and Morphology Comparisons of Self-Assembled Virus-Like Particles from Wild-Type and Mutant Human Hepatitis B Virus Capsid Proteins. 2003;77(24):12950–12960.

19. Mannige R V, Brooks CL. Geometric considerations in virus capsid size specificity, auxiliary requirements, and buckling. *Proc. Natl. Acad. Sci. U. S. A.* 2009;106(21):8531–6.

20. Bruinsma R, Gelbart W, Reguera D, Rudnick J, Zandi R. Viral Self-Assembly as a Thermodynamic Process. *Phys. Rev. Lett.* 2003;90(24):248101.

21. Šiber A, Majdandžić A. Spontaneous curvature as a regulator of the size of virus capsids. *Phys. Rev. E*. 2009;80(2):021910.

22. Crowther R a, Kiselev N a, Böttcher B, et al. Three-dimensional structure of hepatitis B virus core particles determined by electron cryomicroscopy. *Cell*. 1994;77(6):943–50.

2.2 Capsid polymorphism as a geometrical problem

In the first part of this chapter we used a continuum description of curvature based on Helfrichs theory on the energy of liquid-liquid interfaces to account for capsid polymorphism. It would be constructive to compare this model with the complete opposite, a geometrical description of capsid polymorphism that considers proteins as rigid rods and takes their interaction angle into account. For this we will first look into two studies that provide qualitative explanations for the existence of multiple virus capsid sizes based on geometrical models.

Bruinsma *et al.* [1] considered the existence of various polymorphs as a purely geometrical problem. In their model virus capsids are represented by disks that interact with each other through their edges. The Hamiltonian of the capsid then consists of three energy terms: a term related to the interaction between the capsomers, V(0) that depends on the number of capsomers N and their number of contacts z, a term related to the packing fraction of discs, ρ, on a spherical surface that they call the in-plane free energy of the shell, and finally an "out-of-plane" part that originates from the angle, θ, under which the discs interact:

$$H(N) = \frac{z}{2}NV(0) + \frac{B}{2}N[\rho_{max} - \rho(N)]^2 + \frac{\kappa}{2}\sum_{i,j}(\theta_{i,j} - \theta^*)^2 \qquad (13)$$

Plotting the coverage as function of the number of discs then shows which sizes of aggregates are the most stable. They found the surprising result that next to the icosahedral structures also two non-icosahedral shells are stable, corresponding to N=24 and N=48. Allowing for 12 smaller discs (these would be the 12 pentameric disclinations), that carry an extra "switch energy" Δ*E* solves this problem, makes the non-icosahedral structures unstable and causes the T=4 structure stability increase. They also shows that the preference curvature of a disc determines which shell size dominates. That gives us a nice starting point for understanding polymorphism, because this simple Hamiltonian explains how different viruses can exhibit different sizes of capsids. However, Bruinsma *et al.* [1] used discs as building blocks, which is a quite reasonable approximation for viruses with pentameric capsomers (such as the polyoma virus), but does not work for viruses with dimeric capsomers such as HBV. So in the remainder of this paper, with capsomers of HBV we refer to their smallest building blocks, being protein dimers.

Mannige and Brooks [2] used a similar model, but applied it to capsomers with a more physical (trapezoidal) geometry. The major difference is that one trapezoidal capsomer can be in both a 5-fold symmetry element and a 6-fold symmetry element at the same time. This is of importance mainly in the smaller capsid sizes, because there is a large overlap of the 5- and 6-fold symmetry elements. The focused on the effect of capsomers in 6-fold symmetry elements and noticed that in different capsid sizes, the hexamers of capsomers exhibit different conformations thus exert a different amount of stress on the capsomer-capsomer interactions. In correspondence with the Hamitonian by Bruinsma *et al.* [1], Mannige and Brooks [2] expressed the stress energy as function of the difference of dihedral angles between the capsomers with respect to a reference angle (or "endo-angle"). They found the interesting result that only capsids with T≥7 can buckle, because it requires that hexamers can sample at least 2 different conformations and hexamers in lower T-number capsids cannot. This observation will be used later on to account for the polymorphism pattern displayed by HBV. Before we proceed to looking at the specific case of HBV it is good to notice that there is a difference between the capsomers considered in this study and $Cp149_2$, because HBV capsomers do not contain the conserved trapezoidal geometry but are more diamondshaped which has consequences for the amount of interactions per capsomer (4 instead of 5) and the definition of the dihedral angle, as we will discuss later on.

In the following we will provide a model that builds on the description of the capsomer-capsomer interaction energy discussed earlier, that can explain capsid polymorphism of HBV. Section 1 will provide a model that

quantitatively accounts for the observed dimorphism. In section 2, this model is slightly changed in order to account for the absence of larger and smaller capsids. The model used to translate the interaction energy into a size ratio between capsids of different sizes will be the same thermodynamic model that was used in the first part of this chapter:

$$x = x_1 + px_1^p Exp[\frac{-p\varepsilon_p}{kT}] + qx_1^q Exp[\frac{-q\varepsilon_q}{kT}] \quad (14)$$

1.1 A small energy term can account for the observed dimorphism

Equation 14 can be numerically solved and thus we can plot the mole fractions of the different aggregation states as function of the total capsomer concentration x, given certain values for the interaction energy. In the case of HBV p is 90, corresponding to the T=3 capsid and p=120, corresponding to the T=4 capsid. For now we assume that the interaction energy between per capsomer is identical for capsomers absorbed into a T=3 capsid and capsomers absorbed into a T=4 capsid, so $\varepsilon_p = \varepsilon_q$ is -17kT (a value obtained from the analysis by Kegel and Van der Schoot [3]. That gives Figure 21.

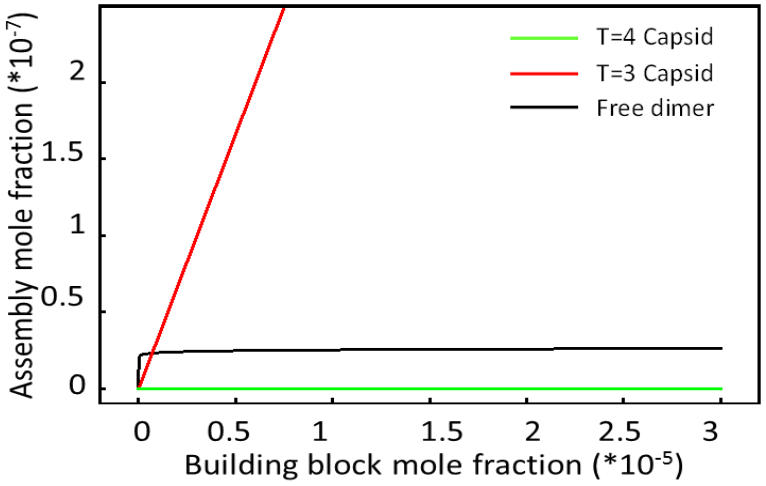

***Figure 21**. Relative abundance of aggregates as function of total capsomer concentration. The graph shows a well-defined ccc at 5*10^{-8}M. At this concentration T=3 capsids start to form, but T=4 capsids remain absent.*

Figure 21 shows a very nice critical micelle like behavior, as was expected. Notice however that in this model the T=3 capsid dominates whereas experimental data on the self-assembly of Cp149 yield a T=4 to T=3 ratio of 95/5 under several conditions [4–6]. This is of course logical, because there is no energy term that distinguishes between small and large capsids and smaller capsids are obviously entropically most favorable.

The simplest means to model an energy term related to the capsid geometry is to introduce a penalty for every fivefold disclination. If one assumes the lowest energy configuration to be an infinite flat sheet of proteins, where all subunits have four contacts under ideal interaction angles, the twelve fivefold symmetry elements, which need to be introduced to bend the sheet into an icosahedron, can be seen as defects with a concomitant energy. The number of fivefold disclinations is constant independent of capsid size, so that the contribution of this defect energy is smaller for large capsids than for small capsids. Together with entropy which favors formation of small capsids, the introduction of this term could lead to a minimum in the energy landscape corresponding to a most stable capsid of a certain size.

$$x = x_1 + \sum_{T=1}^{T=\infty} nx_1^n * e^{[\frac{-n\varepsilon_{int}+12*\varepsilon_5}{kT}]} \quad (15)$$

We found that a penalty of 2.3 kT per fivefold symmetry element is required to find a ratio between T=4 (green) and T=3(blue) capsids of 95:5, see Figure 22. T=1 (red) capsids are not found under these conditions, but T=7 (not shown) would be even more stable.

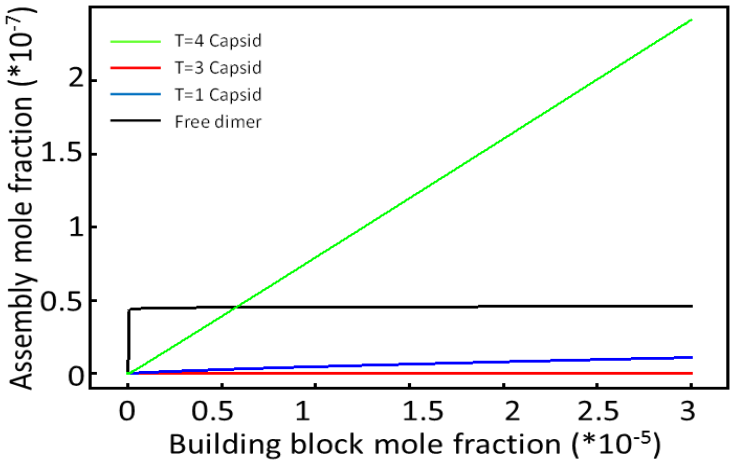

Figure 22. *Number of capsids as function of the total protein concentration, where an energy penalty of 2.3kT was added for every fivefold disclination. For this value the largest capsid is the most abundant.*

This approach shows that a very small energy term is sufficient to radically change the polymorphism of a virus. A defect energy of 20kT per capsid as compared to the interaction energy of the order of 300kT for a T=4 virus is enough to achieve the experimentally observed T=4 to T=3 ratio. However, using only this penalty does not suppress capsids even larger than T=7. Arguably the model is too coarse to achieve that and a more detailed description of the relation between interaction angles and curvature penalty is required. So in order to account for the observed dimorphism we relate the capsid geometry to energy terms. We follow Bruinsma *et al.* [1] in their description of the energy as the sum of an in-plane part and an out-of-plane part. The out-of-plane interaction energy must indeed relate to the some sort of angle that capsomers make with respect to each other. We conjecture that the energy of the capsid depends on the interaction angle rather than an internal angle in the proteins themselves. The underlying postulation is that proteins act as rigid entities and that all curvature is localized at the interaction sides. The angle dependence on the interaction energy can then be attributed to an effective decrease in hydrophobic attraction due to reduced contact area.

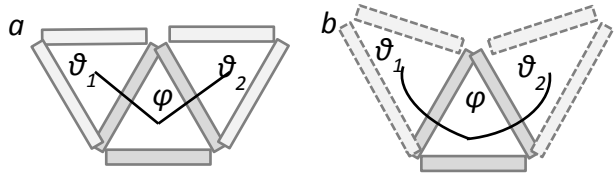

Figure 23*. Definition of interaction angle between capsomers. The (dimeric) capsomers are depicted as rectangles. They all interact with four other capsomers, one at each corner. The interaction energy is optimal (i.e. -17kT) if φ is* $\varphi_{ref.}$ *When the interaction becomes strained due to un unfavorable interaction, the interaction energy becomes less negative. Figure a shows a situation with an unstrained interaction over angle φ and figure b shows a situation where the interaction over angle φ is strained.*

Let us consider a trimer of dimeric protein building blocks and look at the interaction between two capsomers over an angle ϕ (see *Figure 23*). The angle ϕ is fixed and equal to zero in the z-direction, because three dimers always lie within a single plane. That means that the interaction between the two capsomers over this angle can only be strained due to out of plane rotation of the capsomers. One capsomer is always part of two separate trimeric planes. So if those trimers are not in plane with each other (i.e. the dihedral angle is non-zero) the capsomers will rotate away from each other and thus strain their interaction. That means that the

strain on the interaction ϕ is determined by two dihedral angles and a reference angle. For the sake of simplicity we assume that this reference angle is flat but note that this is not necessarily the case.

So the interaction energy between two capsomers is ε_{int} (=-17kT) when the dihedral angle around both capsids equals the reference dihedral angle. Both negatively and positively deviating angles result in a strain so we need a description of the type

$$\varepsilon = \varepsilon(0) + k\left(\frac{\theta_1 + \theta_2}{2} - \theta_0\right)^2 \tag{16}$$

In which θ_1 and θ_2 indicate the angles the two capsomers involved in the strained contact make with their respective neighbors (the two angles are unequal for proteins that border a 3- and 5-fold symmetry element) and k represents the bending stiffness of the capsomers. To estimate this value, let us consider the limiting case that the interaction is under extremely unfavorable conditions. Say, that both capsomers dihedral angles are 90 degrees away from their reference angle, so that in the case of a reference angle of zero, the two triangles that make up a dihedral angle, would be perpendicular to each other. In this case the strain on the interaction is maximal. Yet the strain can never be larger than the original contact energy, since such situation would cause the interaction to simply break. So *k* must be such that at $\theta_1=\theta_2=\theta_0+90$, $\varepsilon=\varepsilon(0)$. That gives a value of *k* in the order of $1*10^{-3}$kT/degree^2 per interaction. This is of course an upper boundary rather than an absolute value, because the bond might be broken at angles lower than in this limit situation.

$$\begin{aligned}
E_{T=1} &= 30\varepsilon_{int} + 60k\left(\tfrac{\theta_1+\theta_1}{2} - \theta_0\right)^2 \\
E_{T=3} &= 90\varepsilon_{int} + 60k\left(\tfrac{\theta_1+\theta_1}{2} - \theta_0\right)^2 + 120k\left(\tfrac{\theta_1+\theta_2}{2} - \theta_0\right)^2 \\
E_{T=4} &= 120\varepsilon_{int} + 60k\left(\tfrac{\theta_1+\theta_1}{2} - \theta_0\right)^2 + 120k\left(\tfrac{\theta_1+\theta_2}{2} - \theta_0\right)^2 + 60k\left(\tfrac{\theta_3+\theta_3}{2} - \theta_0\right)^2 \\
E_{T=7} &= 210\varepsilon_{int} + 60k\left(\tfrac{\theta_1+\theta_1}{2} - \theta_0\right)^2 + 120k\left(\tfrac{\theta_1+\theta_2}{2} - \theta_0\right)^2 + 240k\left(\tfrac{\theta_4+\theta_4}{2} - \theta_0\right)^2
\end{aligned} \tag{17}$$

Where $\varepsilon_{int}$is the interaction energy per capsomer of around -17kT, c is a rigidity constant that contains the two dimensional Young's modulus, k is the bending stiffness of about $1*10^{-3}$kT/degree^2, $\theta_1(=40^0)$is the dihedral angle over a capsomer in a pentamer, $\theta_2(=5^o)$is the dihedral angle over a capsomer neighbouring a pentamer and $\theta_3$and θ_4(respectively 0^o and 5^o) are dihedral angles of capsomers that are exclusively in hexameric geometry, of which the dihedral angle depends on the class of hexamer (see for more information ref (8)). It seems however that by this method of counting interaction angles and assigning an energy to them, either large capsids are suppressed, or small capsids are, but either T=1 or T=7 will always be formed. This is displayed in *Figure 24* where the preference curvature was chosen 0 and the bending rigidity k is $1.75*10^{-4}$ such that both T=1 and T=7 are favored over T=3 and T=4 capsids.

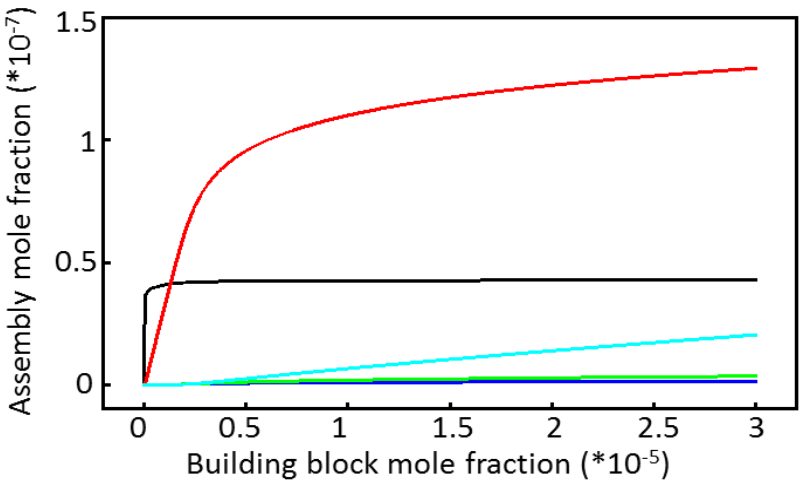

Figure 24. *Number of capsids as function of the total protein concentration, where an energy penalty is related to every interaction angle that deviates from the preference angle that was chosen zero degrees. In this calculation k=1.75*10^{-4}. Then both T=1 and T=7 capsids are favored over the T=3 and T=4 capsid.*

Bruinsma *et al.* [1] stated that there is also an in-plane deformation energy term in the total energy of the capsid that they related to the fraction of the surface of the shell that the disk-shaped capsomers did not occupy. HBV however is not built from disk-shaped capsomers, but rather diamond-shaped capsomers. We assume that in a capsid built from rod shaped capsomers the in-plane deformation energy is a continuum elastics term that relates to the preference curvature of a capsid. It describes the energy originating from the interaction between the twelve 5-fold disclinations. The energy of a single disclination in a flat array of hexamers increases with the size of the array [7]. In the same paper Nelson *et al.* [7] argue that under the buckling transition the energy of all 12 disclinations on a spherical capsid increases with the radius of the capsid squared. Our interpretation of this result is that a pentamer brings along a certain preference curvature for the capsid. Any capsid size larger than the preference curvature leads to stress in the 5-fold disclinations and thus to a higher energy of the capsid. Following Nelson *et al.* [7] this energy per capsid is

$$E = \frac{0.604}{4\pi} * \left(\frac{2\pi}{6}\right)^2 * Y * R^2 \qquad (18)$$

With Y is the two-dimensional Young's modulus and R is the system size. In our case $R=R_{capsid}-R_0$ where R_0 is the preferred radius. The preference radius will be 6.9nm, the radius of a T=1 capsid, because in such capsid the pentamers overlap so that the array of hexamers around a pentamer is zero. Hence, given the fact that there are fivefold disclinations, this must be the preferred capsid size.
Combining these to geometry related energy terms with the interaction energy per capsomer gives the following set of expressions for the energies of different capsid sizes

$$\begin{aligned}
E_{T=1} &= 30\varepsilon_{int} + c(R-R_0)^2 + 60k\left(\tfrac{\theta_1+\theta_1}{2} - \theta_0\right)^2 \\
E_{T=3} &= 90\varepsilon_{int} + c(R-R_0)^2 + 60k\left(\tfrac{\theta_1+\theta_1}{2} - \theta_0\right)^2 + 120k\left(\tfrac{\theta_1+\theta_2}{2} - \theta_0\right)^2 \\
E_{T=4} &= 120\varepsilon_{int} + c(R-R_0)^2 + 60k\left(\tfrac{\theta_1+\theta_1}{2} - \theta_0\right)^2 + 120k\left(\tfrac{\theta_1+\theta_2}{2} - \theta_0\right)^2 + 60k\left(\tfrac{\theta_3+\theta_3}{2} - \theta_0\right)^2 \\
E_{T=7} &= 210\varepsilon_{int} + c(R-R_0)^2 + 60k\left(\tfrac{\theta_1+\theta_1}{2} - \theta_0\right)^2 + 120k\left(\tfrac{\theta_1+\theta_2}{2} - \theta_0\right)^2 + 240k\left(\tfrac{\theta_4+\theta_4}{2} - \theta_0\right)^2
\end{aligned} \qquad (19)$$

We used this set of expressions to plot the mole fractions of the several capsid sizes as function of the total concentration of capsomers, as can be seen in *Figure 25*. When the parameters are chosen correctly, the experimentally observed ratio of T=3 and T=4 capsids can be found, where both smaller and larger capsids are absent. The model itself is however rather pathological in a way that it combines a continuum description of in-

plane curvature and a rigid atomistic description of the out-of-plane bending. For this reason the continuum elastics approach based on Helfrich's curvature free energy that was introduced in the previous section, would be preferred over this combined model.

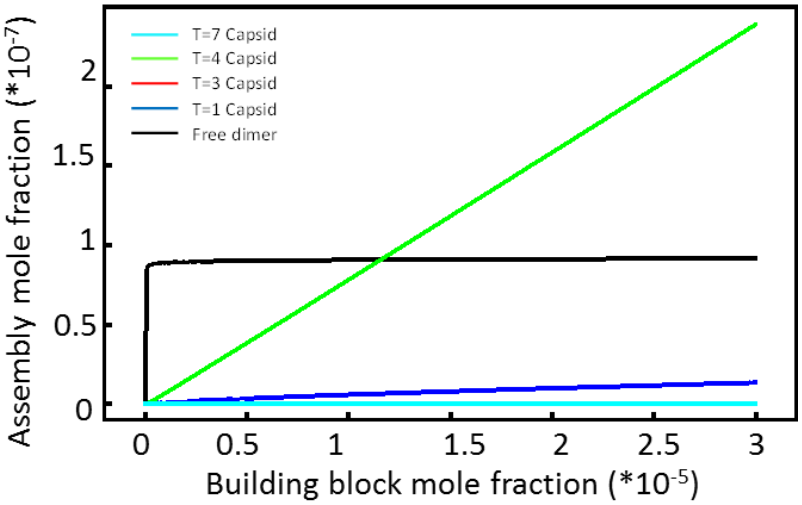

Figure 25. *Number of capsids as function of the total protein concentration, where an energy penalty is related to every interaction angle that deviates from the preference angle that was chosen 5 degrees. In this calculation k=7*10^{-4}. The energy constant related to in-plane curvature is 1. The radii used for the calculation are 6.9, 11.9, 13.6 and 18.2 nm for T=1, T=3, T=4 and T=7 capsids respectively. Under these circumstances indeed a T=4/T=3 ratio of 95:5 combined with suppression of both T=1 and T=7 capsids can be acquired.*

At this point it would be interesting to discuss the implications of the fact that a rigid description based on a geometrical 'sticks-and-balls' model of virus capsids is not capable of accounting for the observed virus capsid polymorphism, where a continuum elastics model based on curvature in liquid-liquid interfaces is. One could argue that the rigid description is a more accurate rendering of real virus capsids than a liquid-liquid interface, considering the comparison with crystal structures, but one should keep in mind that proteins are soft matter. They are flexible, folded polymers that can rearrange and bend. It may therefore be erroneous to focus all the bending energy on the interaction angles, where the flexible proteins themselves may just as well serve as hinges. It is plausible that in such flexible and possibly even dynamic virus capsid the curvature is not localized on fivefold symmetry elements or interaction sides at all, but homogenously spread over the entire structure. In such case a continuum description would indeed be expected to be a more accurate representation of reality. That being said, the truth is likely somewhere in the middle. Although proteins themselves are flexible and hence can contribute to curvature, it is likely easier to bend interaction sides where no covalent bonds are present than the protein itself.

References

1. Bruinsma, R., Gelbart, W., Reguera, D., Rudnick, J. & Zandi, R. Viral Self-Assembly as a Thermodynamic Process. *Phys. Rev. Lett.* **90,** 248101 (2003).

2. Mannige, R. V & Brooks, C. L. Geometric considerations in virus capsid size specificity, auxiliary requirements, and buckling. *Proc. Natl. Acad. Sci. U. S. A.* **106,** 8531–6 (2009).

3. Kegel, W. K. & Schoot Pv, P. Van Der. Competing hydrophobic and screened-coulomb interactions in hepatitis B virus capsid assembly. *Biophys. J.* **86,** 3905–13 (2004).

4. Ceres, P. & Zlotnick, A. Weak Protein-Protein Interactions Are Sufficient To Drive Assembly of Hepatitis. **4,** 11525–11531 (2002).

5. Zlotnick, a, Johnson, J. M., Wingfield, P. W., Stahl, S. J. & Endres, D. A theoretical model successfully identifies features of hepatitis B virus capsid assembly. *Biochemistry* **38,** 14644–52 (1999).

6. Wingfield, P. T., Stahl, S. J., Williams, R. W. & Steven, a C. Hepatitis core antigen produced in Escherichia coli: subunit composition, conformational analysis, and in vitro capsid assembly. *Biochemistry* **34,** 4919–32 (1995).

7. Lidmar, J. & Nelson, D. R. Virus shapes and buckling transitions in spherical shells. 1–11 (2003).

2.3 Kinetic competition in virus capsid assembly

In the first part of this chapter two models were discussed to predict the ratio between virus capsids of different sizes, one based on equilibrium thermodynamics and one based on assembly kinetics. In both cases a difference in assembly energetics, due to curvature of capsids of various sizes, was related to a ratio between concentrations of the different capsids. Assuming thermodynamic equilibrium, it may be intuitive that the equilibrium energy directly relates to an equilibrium concentration of a certain aggregate, but how these interaction energies translate capsid concentrations via a kinetic model is less straightforward. Therefore the purpose of this section is to elaborate on the kinetic model of capsid assembly, indicate which assumptions were made in the process and show how these calculations lead to a prediction for the polymorphism of HBV.

The cornerstone of a kinetic model of virus capsid assembly is the assumption of hysteresis upon assembly. If monomers are stuck once a capsid is complete and hence no exchange of building blocks between capsids of different sizes can occur, the aggregate concentrations are determined by their respective assembly rates. So we consider the concurrent assembly of two types of capsids, one containing p monomers and one containing q monomers. Here monomers refers to the smallest building block, but these can still be protein dimers as long as they are irreversibly attached. When two capsids of different sizes are assembled with their respective steady-state assembly rates from the same pool of monomers, both assembly processes will stop simultaneously as the monomer pool is depleted, resulting in a linear relation between final concentrations and assembly rates.

Based on Zandi *et al.* [1] we describe the assembly kinetics using classical nucleation theory of virus capsids. Intuitively the assembly rate depends on the free monomer concentration (or rather on the supersaturation) so that the increase in capsid concentration follows sigmoidal growth, as was also observed experimentally for BMV [2] and HBV [3]. In the theory proposed by Zandi *et al.* [1] this sigmoidal growth curve is approximated by a lag time followed by a steady state assembly rate that is no longer time dependent. The time-independent steady-state assembly rate is given by the following equation:

$$J^0 = \nu Z e^{-\Delta G} \tag{20}$$

where ν is the attempt frequency, a measure for the rate with which monomers probe the incomplete capsids, Z is the Zeldovich factor that accounts for the time the incomplete aggregates persist without disassembling and ΔG is the free energy barrier of nucleation scaled to thermal energy. Expressions for the Zeldovich factor and the nucleation energy are given below.

$$Z = \sqrt{\frac{a}{n\pi}}(1+\Gamma^2)^{3/4} \tag{21}$$

$$\Delta G = \frac{n*a}{2}\left(\sqrt{\Gamma^2+1}-\Gamma\right) \tag{22}$$

Here Γ is a measure of the supersaturation that drives the capsid assembly and *a* represents the rim energy that determines the nucleation barrier height in units kT. They are given by the following equations

$$\Gamma_n = \sqrt{n-1}\left(1-\frac{\ln(\varphi)}{\ln(\varphi_c)}\right) \tag{23}$$

$$a_n = \pi * c * \frac{\Delta g}{\sqrt{n}} \tag{24}$$

Where c represents a geometrical factor that relates to the number of bonds a protein at the rim lacks with respect to a protein in a fully assembled capsid. The interaction energy in kT per building block is given by Δg.

The simplest way to estimate the ratio between two different capsid sizes from their assembly-rates is by assuming that the lag times are negligible. This can be justified by the notion that the assembly time is of the order of 50 times larger than then lag time [2]. Furthermore we can estimate the ratio between both lag times between a T=4 capsid and a T=3 capsid for equal interaction energies and attempt frequencies to be 1.15 using the following equation. So only a small percentage of a short lag time would favor either of the capsids. It is unlikely that a difference in these small lag times will result in a large difference in ultimately obtained concentration.

$$t_{lag} = \frac{1}{4\pi\nu Z^2} \tag{25}$$

Then the ratio between the concentrations of the two types of capsids equals the ratio between their respective assembly rates

$$\frac{\rho_q}{\rho_p} = \frac{J_q^0}{J_p^0} = \frac{\nu_q Z_q e^{-\Delta G_q}}{\nu_p Z_p e^{-\Delta G_p}} \tag{26}$$

The Zeldovich factor and energy barrier height can be calculated using the above equations, but the attempt frequency is notoriously hard to estimate. In this model it would be safest to assume that the attempt frequency for the formation of either capsid is the same. This corresponds to a reaction-limited assembly process where the attempt frequency depends on local structure of the proteins and the time it takes for them to restructure themselves upon addition to an incomplete capsid. The alternative is diffusion-limited assembly where the flux of free monomers to incomplete capsids is the limiting factor. This flux scales with the area to which new proteins can attach, which is the rim times the shell thickness. The rim circumference scales with square root of the number of proteins in the incomplete capsid. Since the formation of a critical nucleus is the rate-determining step in the assembly process, the relevant number of proteins is the size of the critical nucleus. The size of the critical nucleus is given by

$$n_* = \frac{n}{2}\left(1 - \frac{\Gamma}{\sqrt{\Gamma^2 + 1}}\right) \tag{27}$$

For coat proteins with an interaction energy of 15 kT at a concentration of 300 μM the critical nuclei consist of 11 and 12 building blocks for assembly into T=3 and T=4 capsids respectively. Since there is hardly any difference in the size of the critical nuclei, the critical rim area that determines the monomer flux will also be similar. Hence we consider it safe to assume that the attempt frequency will not be of significant influence on ratio between different capsid sizes.

Then the ratio between assembly rates only depends on protein concentration, interaction energy, the number of proteins in the complete capsid and the geometrical factor c. For the latter 0.5 seems a logical choice [1], since a protein at the rim will miss about half its contacts. One could however also argue it is slightly smaller since the proteins at the rim will maximize interaction with their neighbors. So in theoretical papers on virus assembly several suggestions were proposed such as c=0.1 and c=1/π [4,5] based on thermodynamic consistency arguments. Unfortunately the choice of c has a significant effect on the ratio between different capsid sizes that is found, as is visualized in *Figure 26*.

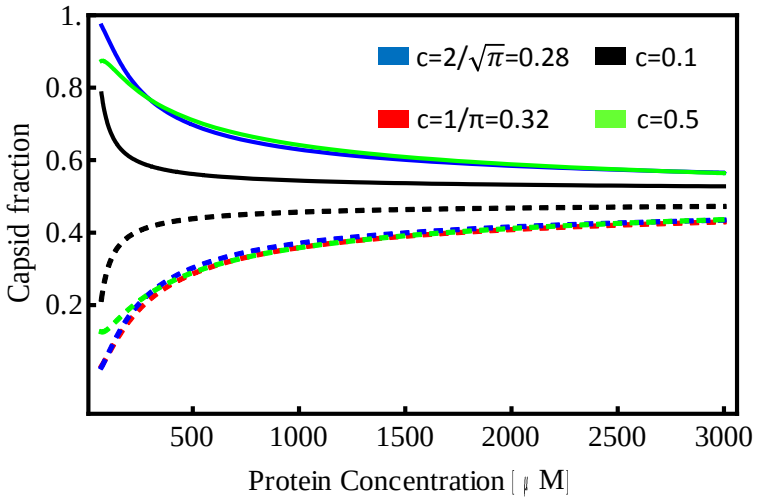

Figure 26. *Fraction of T=3 capsids (continuous line) and T=4 capsids (dashed line) as function of protein concentration for different values of the geometrical factor c. No curvature was taken into account and the interaction energy used was 15 kT.*

The reason is that c acts as a weighing factor for the contribution of the supersaturation with respect to the energy barrier height. Especially for lower values of c the barrier height becomes irrelevant and the ratio starts to approach 1 independent of other conditions. The trend that at higher concentrations all capsids start to be formed at equal rates is however independent of the choice for c, so that it will not drastically change our conclusions. In the rest of the analysis we follow Zandi and Van der Schoot [5] in the choice for c=1/π.

Within the approximation that the sigmoidal growth curves of capsid assembly can be described by a steady-state assembly rate, we have made plausible that all assumptions are reasonable. But so far we have not discussed the validity of the use of a steady-state assembly rate itself. This would only be reasonable if the linear increase regime of the sigmoidal curve is longer than the depletion regime, where the assembly decreases due to an exhausted monomer pool. Therefore we will now show how the time dependency of the critical monomer concentration can be taken into account to obtain a differential equation that can be numerically solved. For this we consider self-assembly as a time dependent process, where at every instance the assembly rate obeys the steady-state approximation and can be calculated from the instantaneous free monomer concentration. The free monomer concentration in turn decreases in time due to simultaneous assembly of the two capsids (with p and q building blocks) yielding the following differential equation.

$$\frac{\partial \rho_m}{\partial t} = -q * \rho_m(t) \nu_q Z_q[\rho_m(t)] e^{-\Delta G_q[\rho_m(t)]} - p * \rho_m(t) \nu_p Z_p[\rho_m(t)] e^{-\Delta G_p[\rho_m(t)]} \qquad (28)$$

This can only be solved iteratively in three steps. In the first step the steady-state assembly rates are calculated on a time t from the monomer concentration ρ_m. These values can be used to calculate the decrease in monomer concentration during time dt in the second step. Then the new monomer concentration at time t+dt can be calculated from the previous monomer concentration and the increase in time. This process is shown in the following equation.

$$J_q^0 = \nu * Z_q(\rho_m) * e^{-\Delta G_q(\rho_m)}$$
$$J_p^0 = \nu * Z_p(\rho_m) * e^{-\Delta G_p(\rho_m)}$$

$$d\rho_q = \rho_m * J_q * dt$$
$$d\rho_p = \rho_m * J_p * dt \qquad (29)$$
$$d\rho_m = -(J_q * dt + J_p * dt)$$

$$\rho_q = \rho_q + d\rho_q$$

$$\rho_p = \rho_p + d\rho_p$$
$$\rho_m = \rho_m + d\rho_m$$
$$t = t + dt$$

The required input parameters are the monomer concentration at time t=0, the duration of time increments dt ($dt=t_{max}/n_{step}$), the number of building blocks in the complete capsid, the free energy of interaction, the attempt frequency and the geometrical factor c. The iterations must be stopped when the monomer concentration falls below the critical monomer concentration. This value is approached asymptotically so that it is most time-efficient to abort the iterations at $\rho_m=1.1*\rho_c$.

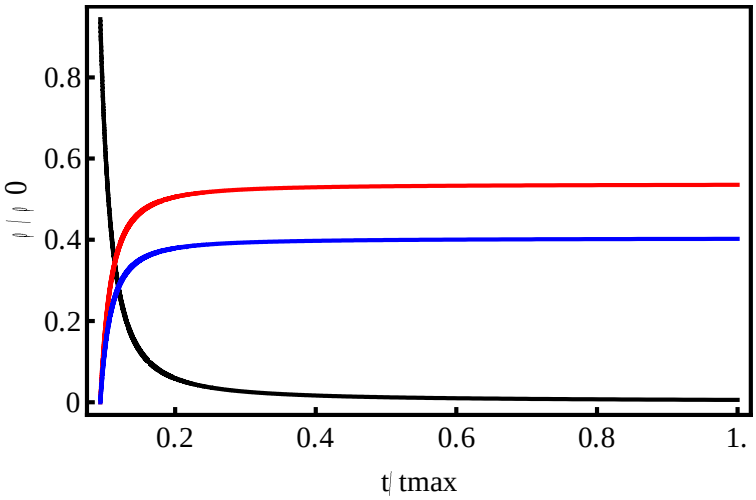

Figure 27. *Time dependent increase of capsid concentration with concomitant decrease of monomer concentration. The total building block concentration was chosen 300 μM, the interaction energy -15kT for both capsids (so no curvature effects are taken into account). The attempt frequency was chosen 1 and the geometrical factor c=0.02 (for which T=3 and T=4 capsids are expected to assemble at equal rate). The reason that there are more proteins absorbed in T=4 capsid than in T=3 capsid is that T=4 capsids contain 120/90 times more building blocks. The ratio between T=4 and T=3 capsids is exactly 1.*

Figure 27 shows that the time dependent assembly can indeed relatively well be described by a steady-state assembly rate. About 90 % of the protein building blocks are absorbed in capsids during the linear assembly regime, and only 10 % in the depletion regime, where the assembly rate significantly decreases with time. Still all conclusions drawn in the previous part of this chapter are based on such time dependent calculations. An advantage of this iterative method to describe kinetic competition between capsids of different sizes is also that capsids of other sizes can easily be taken into account, since we are no longer calculating a ratio between two assembly rates, but absolute values.

In the above, we have only considered assembly where the interaction energy between proteins is the same in all capsids, independent of size or geometry. In order to favor one capsid size over the others, a curvature free energy needs to be implemented in the interaction energy. Again the effects are straightforward in the thermodynamic model, where a stronger (less penalized due to curvature) interaction potential leads to a deeper minimum in the free energy and hence a higher equilibrium concentration of capsids of the corresponding size. In the kinetic model implementation of the curvature free energy term has two separate effects. The change in interaction potential alters the supersaturation via critical monomer concentration and the barrier height through the rim tension. It is the interplay between those effects that eventually determines which capsid assembles the fastest. Clearly still the least penalized capsid size wins, but the effect is less pronounced than for the thermodynamic model because not only the supersaturation that drives assembly is affected, but also the barrier height that stalls it. Therefore the bending rigidity, that sets the energy scale for the penalty due to curvature, needs to be higher in the kinetic model than in the thermodynamic model (20kT with respect to 5kT) to find a ratio between T=4 and T=3 capsids of 95:5. Another result of this 'softening' of the curvature effect is that at protein concentrations of several millimolar, the kinetic model predicts formation

of T=7 capsids for viruses that otherwise only assemble in shells with T=3 or T=4 geometry, as can be seen in Figure 28.

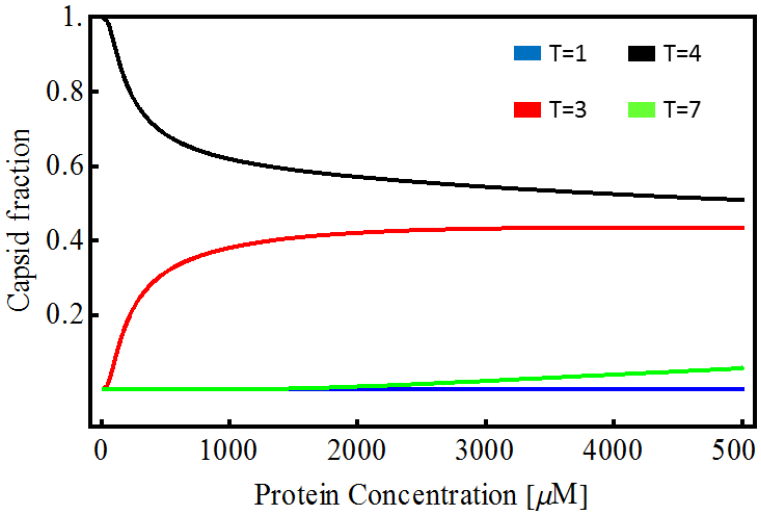

Figure 28. *Predicted virus capsid polymorphism at different protein concentrations based on kinetic competition. The bending rigidity, k, was chosen 20kT at a preference curvature of 120 building blocks. so that the ratio between T=4 and T=3 capsids is about 95:5 at concentrations between 20 and 300 μM, where Zlotnick performed his experiments. The geometrical factor c=1/π and the interaction energy in absence of curvature is 15kT.*

So we described how competition between virus capsids of different sizes can be predicted based on assembly rates and validated assumptions taken in the model. A choice for the geometrical factor c, remains problematic when searching for quantitative results but does not change the conclusion that the experimental data by Zlotnick can be described using the kinetic model, when the proper curvature free energy is applied. Moreover the kinetic model predicts formation of T=7 capsids at very high protein concentration.

References

1. Zandi, R., van der Schoot, P., Reguera, D., Kegel, W. & Reiss, H. Classical nucleation theory of virus capsids. *Biophys. J.* **90,** 1939–48 (2006).

2. Chen, C., Kao, C. C. & Dragnea, B. Self-assembly of brome mosaic virus capsids: insights from shorter time-scale experiments. *J. Phys. Chem. A* **112,** 9405–12 (2008).

3. Zlotnick, a, Johnson, J. M., Wingfield, P. W., Stahl, S. J. & Endres, D. A theoretical model successfully identifies features of hepatitis B virus capsid assembly. *Biochemistry* **38,** 14644–52 (1999).

4. Luque, A., Reguera, D., Morozov, A., Rudnick, J. & Bruinsma, R. Physics of shell assembly: line tension, hole implosion, and closure catastrophe. *J. Chem. Phys.* **136,** 184507 (2012).

5. Van der Schoot, P. & Zandi, R. Kinetic theory of virus capsid assembly. *Phys. Biol.* **4,** 296–304 (2007).

2.4 Relation between protein structure and preference curvature

Previously we showed how virus capsid polymorphism can be described using Helfrichs curvature free energy term that depends on a bending rigidity k and a preference curvature n_0. The bending rigidity k was used as fit parameter to compare the model with experimental data on HBV, and for the preference number of building we used the value 120 based on the observation that the T=4 capsid is the most abundant for HBV. It would however be interesting to link this preference curvature to the atomic structure of the coat proteins that make up virus capsids.

As mentioned before, Zlotnick *et al.*[1] showed that by systematically varying the length of the C-terminal tail, they could change the ratio between T=3 and T=4 capsids that were formed. Apparently they varied the preference curvature of the protein, which can be understood from comparison with critical micelle theory. Also there the ratio between size of the polar head group and the length of the apolar tail determines the size of the micelle. The unstructured C-terminal tail seems to be a generic feature of viral coat proteins [2,3]. Hence we conjecture that the preference curvature might be determined by the ratio between this C-terminal tail length and the size of the protein core.

In order to make the connection between the size of the protein and the preference curvature, we consider a simplified picture of viral proteins, where the core is a spherical domain with radius R_1 which is attached to the tail, that also occupies a spherical space of radius R_2. The distance between the centers of both spheres is then given by $d=R_1+R_2$. Both spheres define a cone of a certain length that determines the capsid radius R_c, as shown in Figure 29.

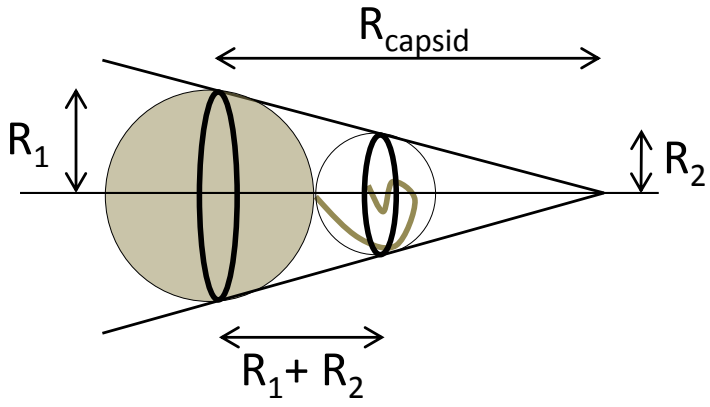

Figure 29. *Schematic of the cone defined by the core size and tail length of virus coat proteins, that defines the preference curvature. R_1 is the radius of the spherical core and R_2 the radius of the spherical space occupied by the tail.*

From basic congruency principles it can be shown that

$$\frac{R_c}{R_1} = \frac{R_c - (R_1 + R_2)}{R_2} \tag{30}$$

Then the preferred capsid radius is given by

$$R_c = R_1 \frac{(R_1 + R_2)}{(R_1 - R_2)} \tag{31}$$

In order to translate this radius to a preference number of building blocks, we divide the capsid surface by the surface of a single capsomer and multiply by a packing density σ to correct for the non-ideal packing of disks on a sphere.

$$n_0 = R_1 \frac{4\pi {R_c}^2}{\pi {R_1}^2} * \sigma = 4\sigma \left(\frac{R_1 + R_2}{R_1 - R_2}\right)^2 \quad (32)$$

Now we can link the radii of the two spheres to the number of amino acids that the protein is constituted of. The core of the protein is structured so we assume that the radius scales with the number of amino acids to the power 1/3. For the tail, the radius of the sphere is scales with a power ν that should vary between 1 for a stiff chain and 1/2 for a freely jointed chain. The resultant preference curvature is given by the following equation

$$n_0 = 4\sigma \left(\frac{{n_c}^{1/3} + {n_t}^{\nu}}{{n_c}^{1/3} - {n_t}^{\nu}}\right)^2 \quad (33)$$

Combining this with the thermodynamic model for polymorphism from the first part of this chapter, we can fit the model to the data by Zlotnick using σ and ν as fit parameters, as is shown in Figure 30.

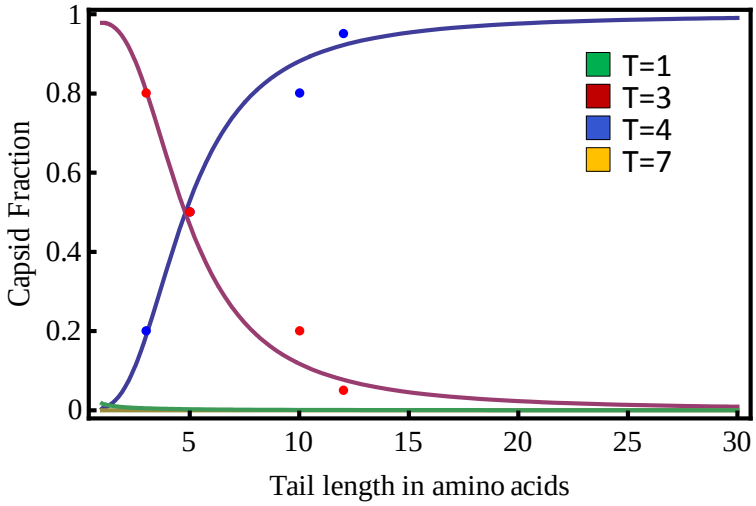

Figure 30. *Variation of polymorphism pattern with length of C-terminal tail of the HBV capsid as predicted by the geometrical model described above. Dots represent experimental data on the relative concentrations of T=3 (red) and T=4 (blue) capsids by Zlotnick et al.*[1] *From the x-ray structure* [4] *the number of amino acids in the core was found to be 127. The values of ν and σ required to fit the model to the data were 0.2 and 12 respectively.*

Considering the simplicity of the model, it manages to describe the experimental data strikingly well, although the values for the two fit parameters required to match model and experiments are outside the expected range. For ν we expected a value between ½ and 1 and it turned out to be 0.2. That would mean that the tail is actually more compact than a globular polymer, like the core. This can be understood as a preference of the tail to be elongated so that the space it occupies resembles a prolate ellipsoid rather than a sphere. The radius R_2 of this prolate might then indeed be smaller than the hydrodynamic radius of a freely jointed chain with the length of the tail. The value of 12 for the packing density σ is less easy to understand. Obviously the actual packing fraction can never exceed 1, so that there must be another factor involved that causes the apparent preference curvature to be higher than the predicted one. From this same model the prediction follows that measurable quantities of T=7 capsids could be observed if the tail is extended with 80 amino acids. It is however unlikely that the protein will survive such major modification.

References

1. Zlotnick, a *et al.* Dimorphism of hepatitis B virus capsids is strongly influenced by the C-terminus of the capsid protein. *Biochemistry* **35,** 7412–21 (1996).

2. Prasad, B. V. V. X-ray Crystallographic Structure of the Norwalk Virus Capsid. *Science (80-.).* **286,** 287–290 (1999).

3. Willits, D. *et al.* Effects of the cowpea chlorotic mottle bromovirus beta-hexamer structure on virion assembly. *Virology* **306,** 280–8 (2003).

4. Wynne, S. a, Crowther, R. a & Leslie, a G. The crystal structure of the human hepatitis B virus capsid. *Mol. Cell* **3,** 771–80 (1999).

Apendix: Energy landscape of capsid assembly with different geometries

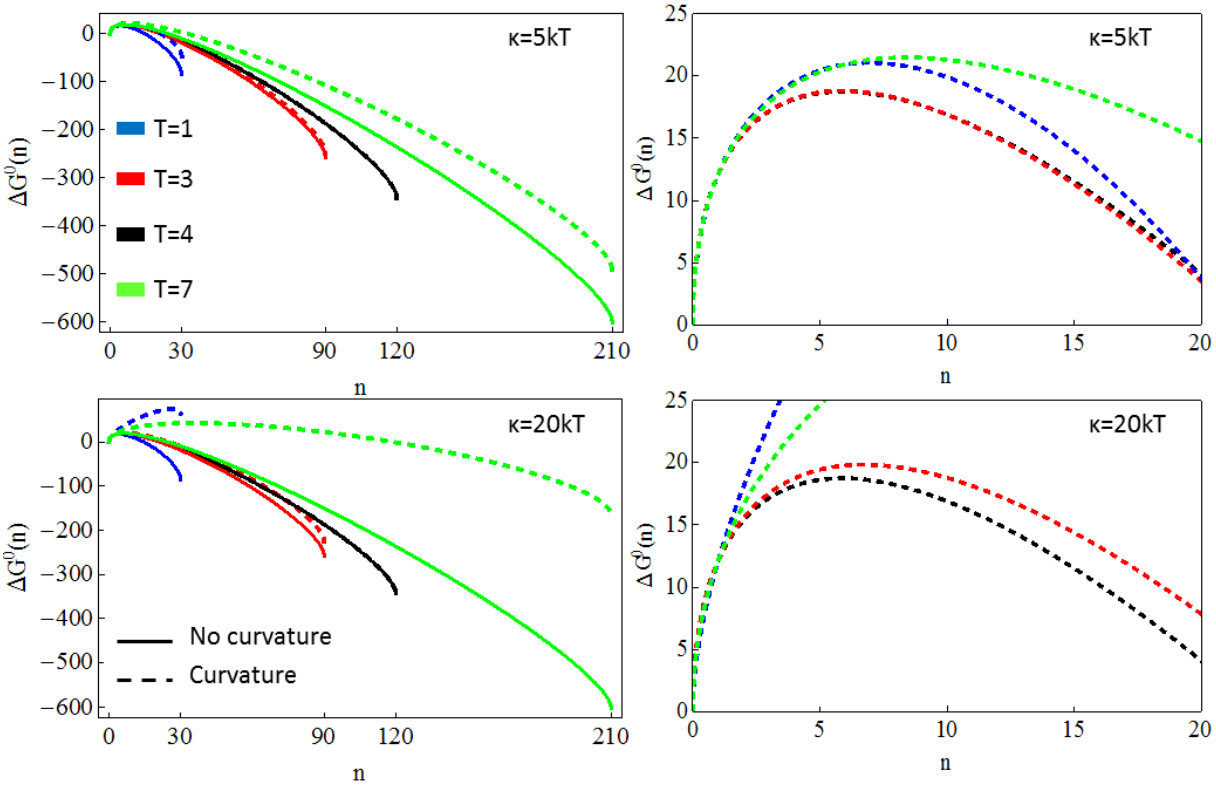

Figure 31. *The energy landscape of Hepatitis B virus capsid self-assembly. Free energy of binding is indicated as a function of number of capsomers in the (incomplete) capsid. The upper two pictures consider a stress constant of 5kT, which is required to account for the observed dimorphism using equilibrium thermodynamics, and the lower two pictures show the landscape with a stress constant of 20kT, which is required using the nucleation kinetics model. The right pictures are zoom-ins on the free energy barrier.*

Part 3

Solution state NMR study of the HBV capsid

In the previous chapters the interaction potential was discussed that drives virus capsid self-assembly, how this energy depends on conditions such as salt concentration, pH and temperature and what the contribution of curvature is. In the model used for this description, the contribution of entropy was taken into account implicitly through analogy with micellization theory. The only entropic component in the model is translational entropy, while internal degrees of freedom have not been taken into account. A protein is not properly described as a rigid unit but has a certain degree of internal flexibility, the extend of which varies from domain to domain. Upon assembly about 5 *kT* of translational and rotational entropy is lost that is unlikely to be compensated by a high interaction enthalpy for reasons that will be discussed later on. We therefore hypothesize that the protein building blocks will increase their internal dynamics to minimize the entropy loss upon assembly.

In the following chapter we will describe how state-of-the-art solution state NMR spectroscopy techniques were employed to investigate protein dynamics of the 4 MDa HBV capsid. The dynamics measurements together with diffusion experiments that provided an indication for subunit exchange, will be discussed in the first part. Then a section will be devoted to challenges in performing solution state NMR spectroscopy on such large protein complex. The pulse program of a Diffusion-TROSY will be introduced that allows measurement of the diffusion coefficient for every peak in a relaxation optimized [^{1}H,^{15}N]-correlation spectrum and its application on proton exchange in Ubiquitin will be given. A protocol for magnetic gradient calibration is provided and finally a theoretical background of all performed NMR experiments is given.

3.1 NMR study of exchange and dynamics in the Hepatitis B virus capsid

Abstract

The coat proteins of a large class of viruses, amongst which Hepatitis B, display the ability to spontaneously self-assemble into hollow capsids in the absence of genetic material. The potential driving this assembly process consists of a hydrophobic attraction balanced by an electrostatic repulsion and is of the order of 10 *kT* per subunit. How such weak interaction enthalpy can drive spontaneous assembly of capsids from 120 building blocks raises questions on the contribution of entropy to this process. We hypothesize that an increase in protein flexibility upon virus assembly will minimize entropy loss. This paper describes a solution state NMR study to these dynamics in a HBV capsid with an effective molecular weight of 20 MDa. We find indications for subunit exchange between dimer and capsid corroborating the notion of weak interaction enthalpy. Furthermore we obtained qualitative information on the global dynamics of the HBV capsid using the size dependence of cross-relaxation induced polarization transfer and we find that the C-terminal tail is the only region of the protein with flexibility on timescales of microseconds or faster.

Introduction

In the past decade the upper size limit of solution state NMR spectroscopy was extended through the invention of TROSY[1] (Transverse Relaxation Optimized Spectroscopy) and CRIPT[2] (Cross Relaxation Induced Polarization Transfer). Before development of these techniques biomolecular structures of more than 50 kDa were unamendable to solution NMR techniques due to fast transverse relaxation of spin magnetization. The development of TROSY increased this size limit about fourfold by exploiting the mutual internal cancellation of chemical shift anisotropy (CSA) and dipole-dipole interactions (DD). A smart trick of peak selection where this phenomenon is most effective lead to minimization of signal relaxation during chemical shift evolution and data acquisition so the size limit was mostly governed by loss of coherence during magnetization transfer periods. The development of CRIPT overcame a large part of this problem and gave the perspective to perform solution state NMR analysis of megadalton protein complexes. Here we employ these NMR techniques to investigate dynamics of the Hepatitis B virus, which has a rotational correlation time corresponding to a 20 MDa molecular weight object. (HBV) capsid, challenging previous NMR size limits.

This study of protein dynamics was motivated by a major unresolved problem concerning the contribution of entropy to the self-assembly of virus capsids, protein shells that contain and protect viral genomic material. Obviously the formation of large well-ordered protein aggregates is an entropically highly unfavorable process. Hence, in the case of spontaneous assembly, one would expect large binding enthalpies to compensate for the loss of entropy, which is in poor agreement with the notion that capsid assembly must be reversible[3,4] This is required for the assembly of fully formed capsids since in the case of irreversible assembly high interaction enthalpies would lead to large Kramer's escape times, thereby preventing the subunit exchange and inducing formation of kinetic traps instead of complete capsids. As a consequence we expect capsomers that are absorbed in capsid shells to retain or even increase part of their rotational or vibrational degrees of freedom to minimize the loss of entropy upon assembly. Hence assembled proteins should display a larger degree of flexibility than unassembled building blocks. This study of dynamics in virus capsids is not only interesting from a fundamental point of view, but will also lead to a more thorough understanding of the morphology of viruses, which is useful for the development of antivirals.

The Hepatitis B virus capsid is a suitable model system for this study of protein dynamics. Firstly because it is thoroughly investigated and thus many properties of this virus, such as the free energy of interaction[3] and the crystal structure (shown in Figure 32) [5] are known and secondly

because self assembly studies have been performed with a truncated version of the capsid protein before. [4,6,7]. This 17 kDa truncation of the viral coat protein, named HBc_{1-149} or Cp149, lacks the arginine rich C-terminal domain that is highly positively charged and was shown to associate with the genomic material of the virus. Like the wild type capsid protein, this construct irreversibly dimerizes through the formation of a disulfide bridge to form the capsid building blocks. Without the C-terminal domain and in the presence of sufficient salt, the electrostatic repulsion is small enough to allow the dimers to aggregate so that they will spontaneously self-assemble into hollow capsids [5]. Through this equilibrium assembly process a mixture is formed containing mostly (~95 %) T=4 capsids built from 120 protein dimers and a small amount (~5 %) of T=3 capsids containing 90 building blocks [4]. Also a small amount of free dimers will be left unassembled that can be compared to a critical micelle concentration. This study focusses on the most abundant (T=4) capsid that was separated from the free dimer and T=3 capsid using sucrose gradient ultracentrifugation.

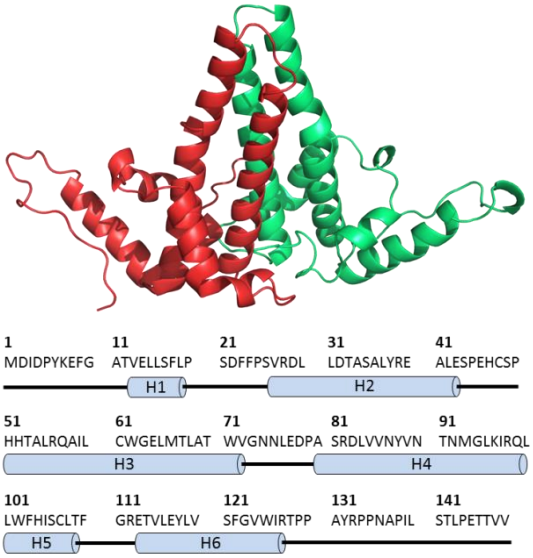

Figure 32. *Sequence and structure of HBV capsid building block. The dimeric building block consists of two mutant coat proteins Cp149, indicated by different colors. The secondary structure of the protein is shown under the sequence where a black line indicates a loop or unstructured element and a cylinder represents a helix. Structure is based on pdb file 1QGT by Wynne et al.* [5].

The remainder of this paper is organized as follows. First we will briefly review the origin of the solution state NMR size limit and techniques designed to overcome this. Subsequently [^{1}H,^{15}N]-correlation spectra of the 4 MDa HBV capsid will be compared with that with the free dimer to identify which part of the capsid can be observed. The third part deals with diffusion experiments and their implications on capsid dimer exchange. Finally we will show measurements of dynamics of the HBV capsid and we introduce a novel method based on CRIPT transfer to measure rotation correlation times of very large protein structures.

NMR size limit

The origin for the NMR size limit is the size dependence of transverse relaxation. Coherence of magnetic spins that leads to signal intensity will partially dephase during an NMR experiment as a consequence of interactions with the surroundings, a phenomenon that is called T_2 relaxation. The other magnetic dipoles in the sample, being other proteins or solvent, show Brownian motion, which leads to fluctuations in the local magnetic field experienced by any nuclear magnetic spin. One can imagine that these fluctuations affect large proteins much more than small proteins, which rotate so quickly that the fluctuations in local the magnetic field average out.

The T=4 capsid is a 4 MDa protein complex, which spans a diameter of about 30 nm (with a spike to spike diameter of 36nm) will have very long rotation correlation times and thus a very short T_2 relaxation time. Note that this rotation correlation time is even 5 times larger even than you would expect based on a mass of 4 MDa because the capsid itself is hollow. So it exhibits the apparent size of a 20MDa protein complex. A poor signal to noise ratio and severe line broadening are expected due to this rapid transverse relaxation. The NMR linewidth $\Delta\nu_{1/2}$ is given by the equation:

$$\Delta\nu_{1/2} = \frac{1}{\pi * T2} \quad (1)$$

$$\frac{1}{T2} = 2\,\gamma^2 < B >^2 \left(\tau_c + \frac{\tau_c}{1 + (\omega_0\tau_c)^2}\right) \quad (2)$$

in which is γ is the proton gyromagnetic constant (267.5 MHz/T), <B> is the average of the magnetic field inhomogeneities that cause the relaxation, τ_c is the rotational correlation time and ω_0 the proton resonance frequency. In the case of large τ_c, the

first term dominates. Previous measurements of the dimer showed an average peak width of around 21 Hz [8]. Using this value and an estimate for its rotation correlation time of 17 ns the average relaxation inducing magnetic field could be calculated ($\langle B \rangle^2$ ~$5*10^{-8}$ T). Using this value, one can get an idea of the peak width of the capsid. This gives a stunning estimate of 6 kHz on a spectrometer operating at 900 MHz. That corresponds a stunning 6.7 ppm.

The rotational correlation time of a 4 MDa capsid was estimated to be 3 to 6 µs (depending on whether the spikes are taken into account) using Stokes' law assuming spherical complexes (a very reasonable approximation for the virus capsid)

$$\tau_c = \frac{4\pi\eta r^3}{3kT} \qquad (3)$$

Clearly protein structures that will result in such peak widths are not amendable to solution state NMR spectroscopy unless measures are taken to minimize relaxation effects. Therefore we employed Transverse Relaxation Optimized Spectroscopy (TROSY) techniques to minimize loss of signal intensity due to relaxation events during chemical shift evolution and acquisition, combined with Cross-Relaxation Induced Polarization Transfer (CRIPT) to minimize signal loss during magnetization transfer.

Experimental procedures

Sample preparation

Perdeuterated, ^{15}N and ^{13}C labeled HBc_{1-149} was overexpressed in E. Coli as described earlier [8]. The protein was purified using affinity chromatography and assembled into virus capsids in a 20 mM Tris buffer at pH 7.4 containing 250 mM NaCl and 50 mM Hepes. T=4 Capsids were separated from T=3 capsids and unassembled dimers using sucrose gradient ultracentrifugation and the total protein concentration was determined to be 600 µM by collaborators Ferguson, Alexander and Jurgens at University College Dublin.

NMR spectroscopy

All NMR spectra were recorded at 298K on a BRUKER AVANCE spectrometer operating at 900MHz proton frequency. DSS (4,4-dimethyl-4-silapentane-1-sulphonic acid) was added as internal standard. The performed experiments are: ^1H-1D, ^{13}C-1D, ^1H-^{15}N-TROSY [1], ^1H-^{15}N-HSQC, ^1H-^{15}N-CRINEPT [2], ^1H-^{15}N-CRIPT [2], HNCO (HC-plane), HNCA (HC-plane), HN(CO)CACB (HC-plane) [9], DOSY, ^{15}N-TRO-STE [10] and TRACT [11] (at 600MHz).

Results and discussion

Sample characterization

An overlay of the INEPT-TROSY spectrum of the capsid with the corresponding spectrum of the free protein dimer is shown in *Figure 33*. Almost all peaks of the capsid spectrum overlay with the peaks of the dimer spectrum, indicating that the observed peaks indeed originate from the Cp149.

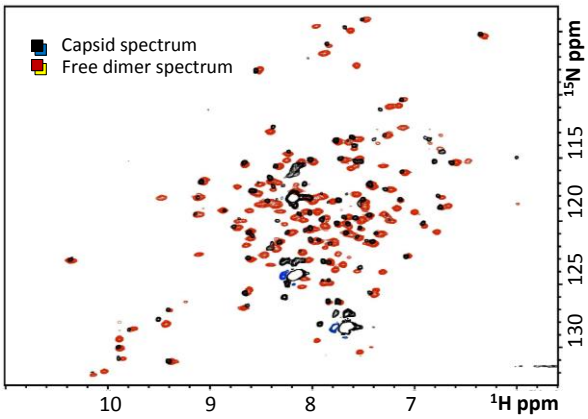

Figure 33. *Overlay of [^1H,^{15}N]-correlation spectra of the Hepatitis B virus capsid (black) and dimer (red) sample. Both spectra are recorded using the BRUKER trosyetf3gpsi2 pulse sequence. The blue negative signal is an artifact related to the high peak intensity of the peak next to it.*

In fact, the observed signals are also visible in the HSQC (see supplementary material) and surprisingly narrow for a structure as large as the HBV capsid, raising the question if they originate from proteins absorbed in a 4 MDa capsid or from a residual amount of free dimer. One can distinguish two kinds of peaks: the high intensity peaks at 7.8 and 8.2 Hppm that do not overlap with peaks in the dimer spectrum on one hand and a large set of low intensity peaks that do show overlap with the dimer spectrum on the other hand. Using HNCA, HNCO and HNCOCACB on the HC planes we could assign the high intensity peak at 7.8 ^{1}Hppm and 130 ^{15}Nppm and the peak at 8.2 ^{1}Hppm and 125 ^{15}Nppm to the C-terminal residues valine 148 and valine 149 respectively.

One can argue that the third high-intensity peak, at 8.2 ^{1}Hppm and 120 ^{15}Nppm , is likely to correspond to the residue next to it, Threonine 147.

Although the high intensity peaks originate from the C-terminal tail of the Cp149 protein, it cannot be concluded yet whether this protein is absorbed in the HBV capsid or free in solution. The distinction between peaks emanating from the 30 nm capsid or the 2 nm dimer can be made using DOSY. Through measurement of diffusion rates per signal, the respective signals could be related to either capsid or dimer. To this means a TROSY-based diffusion experiment (TROSTE [10]) was performed and the measured signal intensity scaled to its maximal value was plotted as function of the strength of the magnetic z-gradient that was applied. A fit of the Stesjkal-Tanner equation

$$S/S_0 = Exp\left[-D * \delta^2 g^2 \gamma^2 \left(\Delta - {}^{\delta}/_{3}\right)\right] \quad (4)$$

yields a value for the diffusion coefficient D. Duration and strength of the magnetic gradient δ and g are known as well as the delay Δ and the gyromagnetic constant γ.

The diffusion coefficient of the dimer was shown to be $2.2*10^{-10}$ m^2. The diffusion coefficient of the residues corresponding to the high intensity peaks at 7.8 and 8.2 proton ppm appeared to be $3.3*10^{-11}$ m^2/s (see *Figure 34*), almost ten times slower than the dimer, suggesting that these signals indeed originate from the HBV capsid.

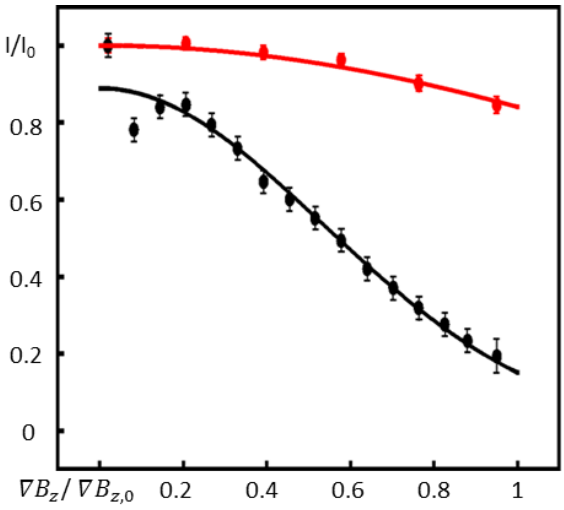

Figure 34. *Signal intensity decay of high intensity peaks in the capsid spectrum (red) and the dimer (black). Normalized signal intensity is shown as function of normalized magnetic gradient strength. Clearly the residues corresponding to the high intensity peaks have a much slower diffusion coefficient than the dimer, indicating that they originate from residues in the HBV capsid.*

Critical micelle theory

For the low intensity peaks we argue that they correspond to the free protein dimer based on the fact that the signals are sharp and observable in the HSQC experiment as well as in the TROSY. For reasons previously discussed a 4 MDa protein complex should not give narrow peaks in a HSQC spectrum. A 34 kDa protein dimer however could. The presence of free monomer in the capsid sample can be explained through the analogy with critical micelle theory. In an equilibrium assembly process a small portion of unassembled building block, which is referred to as a cmc (critical micelle concentration) in micelle theory, must always be present. Based on the peak intensities we show that the free protein concentration is indeed comparable to the cmc. The line of argumentation is the following: the concentration of a structure causing a signal in the capsid spectrum could be estimated by comparing its peak intensity with the peak intensity of the corresponding peak in the dimer spectrum of which the dimer concentration is known. The ratio between the peak intensities is then, when corrected for the difference in number of scans, a measure for the ratio between the concentrations. In this way the concentration matching the low intensity peaks in the capsid spectrum was estimated to be of the order of 5 µM. That corresponds to an interaction potential of -16 kT, which is expected at room temperature with pH=7.4 and a salt concentration of 250 mM [3]. Note that the sample was pure T=4 capsid before the start of NMR experiments and light scattering experiments showed that no free dimer was left in the sample after purification (see supplementary material). So the observation of this critical monomer concentration of free proteins in the NMR sample shows that the system has re-equilibrated which is in accordance with the notion that the enthalpy of interaction is low. The re-establishment of a critical monomer concentration was corroborated by the observation of a small protein concentration in light scattering experiments after the NMR measurements. These

results demonstrate exchange between free dimers and capsids and set the upper boundary for the timescale of this process to be of the order of a week (time between purification and first NMR experiment).

Diffusion and exchange

The diffusion coefficient obtained for the C-terminal capsid peaks V148 and V149 was almost ten times slower than the diffusion of the dimer but still considerably faster than the diffusion of $1.2*10^{-11}$ m^2/s that could be expected for a spherical object with a radius of 15 nm based on the Stokes-Einstein equation (eq. 3). To obtain an accurate value for the diffusion coefficient of the virus capsid, we performed the diffusion experiment for both the V148 and V149 peak at different diffusion delays varying from 100 ms to 1 s of which the results are shown in *Figure 35*. Two observations can be made from those experiments. The first is that for all diffusion delays the obtained diffusion coefficient is 2 to 4 times faster than the theoretical diffusion coefficient. The second observation is that the quality of the fit decreases as the diffusion delay increases. Especially for the experiment with 1 s diffusion delay there appears to be a small but systematic deviation between experiments and fit.

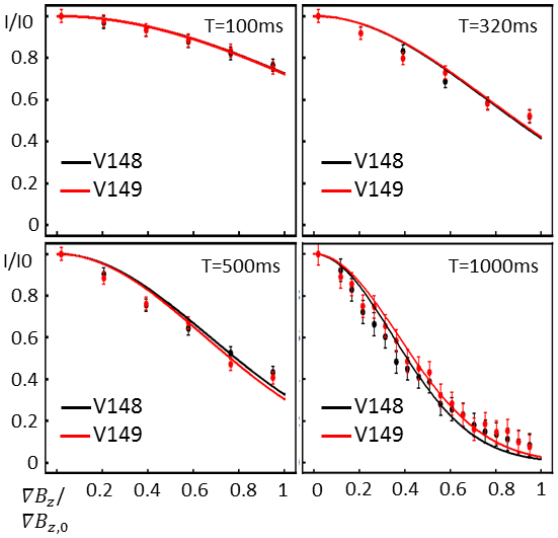

Figure 35. *Diffusion measurements of the C-terminal tail residues in the HBV virus capsid. Red dots correspond to V149 and black to V148. The lines are fits based on the Stesjkal-Tanner equation with the diffusion coefficient as a fit parameter. Error bars represent the noise level.*

We can think of at least two processes that could explain both observations. Either convection in the sample contributes to anomalously quick diffusion or the measured diffusion is faster due to exchange processes with a structure smaller than the virus capsid, which increases the average displacement.

Convection in the NMR sample could be expected because there is a temperature gradient present in the sample holder. The BRUKER Spectrometer operating at 900MHz is particularly notorious for this effect. Convection may lead to a faster apparent diffusion coefficient by addition of a linear displacement as a consequence of solvent flow to the random movement caused by diffusion. Since the random translation of a large structure such as a virus capsid due to Brownian motion is of the order of 1 µm/s, tiny solvent flows of the same order of magnitude may already influence the diffusion experiment. On the other hand, the use of a Shigemi tube should overcome temperature gradient induced solvent flows. If the convection is non-turbulent and causes a linear up- and down flow of equal flow rates, it would add a cosine modulation to the diffusion induced signal attenuation [12]:

$$\frac{S}{S_0} = Cos[\delta * g * \gamma * \Delta * v] * Exp\left[-D * \delta^2 g^2 \gamma^2 \left(\Delta - {}^{\delta}/_{3}\right)\right] \quad (5)$$

Where v represents the flow velocity, which is roughly of the order of 1 µm/s for aqueous liquids at room temperature [13], dependent on the viscosity and the temperature gradient causing the convection. Figure 36 shows attempts to fit the diffusion experiment with a delay of 1 s including both the convection and diffusion induced modulation. The quality of the fits are poor indicating that convection is at least not the only cause of the anomalously high diffusion coefficients. This finding was corroborated by the fact that by application of a convection compensated pulse program [12] a similar diffusion coefficient was found.

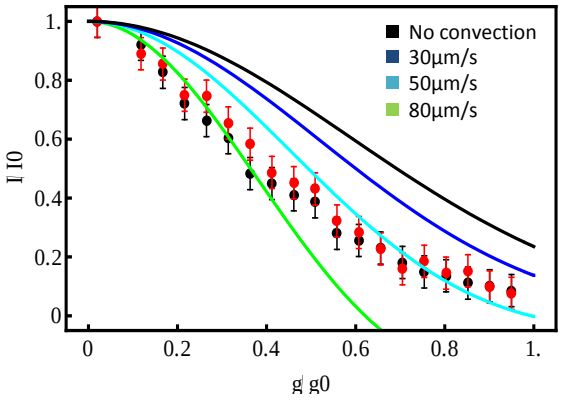

Figure 36. *The simulated effect of convection on signal attenuation of an NMR diffusion experiment. The black line shows signal decay as predicted based on the theoretical diffusion coefficient of the HBV capsid (1.2*10^{-11} m^2/s). The blue, cyan and green lines predict signal decays as result of with a flow rate of respectively 30, 50 and 80 µm/s. The data again represent the diffusion experiments with a delay of 1 s.*

A well-known example of an exchange process that can affect the diffusion coefficient occurs between amide protons and water and was first observed for Ubiquitin by Brand *et al.* [14]. This phenomenon can be recognized by an unexpectedly high diffusion coefficient combined with a poor fit of the Stesjkal-Tanner equation. Brand *et al.* [14] proposed a model to describe the diffusion decay as a function of the diffusion coefficient of both components and the exchange rate between them that indeed describes the data significantly better. The decrease of signal intensity as function of gradient strength for two exchanging objects with diffusion coefficients D_1 and D_2 and an exchange rate k is given by the following equation:

$$\frac{S}{S_0} = \left(e^{-(k+D_1K^2)\Delta} + \frac{k}{k+D_1K^2-D_2K^2} * \left(e^{-D_2K^2\Delta} - e^{-(k+D_1K^2)\Delta}\right) \right) e^{-D_1K^2\left(\tau-\frac{\delta}{3}\right)} \quad (6)$$

Amide proton exchange with water would be a plausible mechanism to account for the fast diffusion coefficients measured for V148 and V149 as well since they are in the C-terminal tail of the virus capsid, where one would not expect to find stable hydrogen bonds. Figure 37 however shows that when using the model by Brand and combining the diffusion of the HBV capsid and water, the fit only becomes worse. This indicates that if the anomalously large diffusion coefficient is a consequence of exchange, the structure with which exchange takes place is larger than water. Figure 37c shows a fit in which both the diffusion coefficient and the exchange rate are free fit parameters. It shows that the diffusion coefficient of the exchanging structure should be of the order of 10^{-10} m^2/s, which corresponds well to the diffusion coefficient of the dimer of 1.01*10^{-10}. The fit yielded a value for the exchange rate k of the order of 1 s^{-1}. Figure 37d shows the difference between the fit value and the experimental value at every data point and clearly the fit taking exchange into account (cyan line) is significantly better than the fit where only the diffusion of a single object was considered. Also exchange with the dimer would explain the faster diffusion coefficient that was observed. This exchange between dimers in the capsid and dimers free in solution was expected since we found that a critical concentration of free proteins was re-established in a week. The timescale of the exchange between dimer and capsid that is suggested by these diffusion experiments should however be on the order of seconds. Slower exchange would not have a significant effect on experiments with a diffusion delay of a second. This would also explain why a systematic deviation in the fits of the Stesjkal-Tanner equation only became visible for experiments with diffusion delays of 500ms to 1s (see Figure 35). The timescale of the exchange however also poses a contradiction. If dimers in a capsid would exchange with the pool of free proteins at such high rates it would never be possible to purify either of the two from the other since a sucrose gradient purification takes several hours to perform. It is also contradictory to a previous study by Heck *et al.* [15] who showed that exchange between dimer and T=3 capsid is of the order of month and who found no exchange between T=4 capsid and dimer whatsoever. We suggest a model of stochastic adsorption and release of dimers, where the timescale of the event can be very fast, of the order of seconds, but the net exchange from a dimer pool to capsid pool depends on an imbalance between on- and off-rates, so that this timescale can be much smaller than the timescale of the actual attachment and detachment process that is observed by NMR. Furthermore the samples investigated by Heck *et al.* [15] contained an equilibrium concentration of dimer and capsid to

begin with so that a driving force for exchange lacks, which gives a possible explanation for the absence of assembly in their experiments.

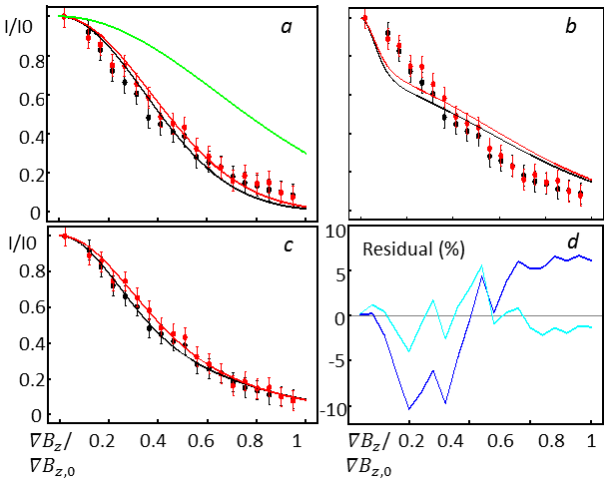

Figure 37. *Effect of exchange on diffusion experiments. a) Dots represent experimental data and lines represent fits of the Stesjkal-Tanner equation. The green line shows a prediction for the diffusion decay of the HBV capsid. (same as in Figure 35b). b) Shows the same data where the fits include exchange with H_20, based on equation 6. Theoretical diffusion coefficients of water ($2.2*10^{-9}$ m^2/s) and the HBV capsid are given as input parameters and the exchange rate was used as a fit parameter. c) Shows the fit where the diffusion coefficient of the structure with which exchange takes place, was also used as a fit parameter. The value for the diffusion coefficient and exchange rate to obtain a good fit are $D=1.1*10^{-10}$ m^2/s and $k=1.1$ s^{-1} respectively. This diffusion coefficient exactly matches the diffusion of a dimer free in solution. d) Shows the residual (difference between fit value and data value) of the fit without exchange (blue line) and the fit with exchange (cyan line).*

Dynamics

To further investigate the properties of the three peaks that likely originate from the virus capsid, a TRACT (TROSY for rotational correlation times) experiment was recorded at 600 MHz. This experiment was first proposed by Lee *et al.*[11] and selectively measures the relaxation rates of α (pointing in the same direction as the nitrogen nuclear spin) and β (pointing in the opposite direction as the nitrogen nuclear spin) amide protons due to ^{15}N relaxation. It uses the fact that relaxation due to dipole dipole (DD) interactions and chemical shift anisotropy (CSA) are independent of spin state but the cross-correlation between the two has a different sign for alpha protons than for beta protons. This means that $R_\beta - R_\alpha$ is a measure for the cross-correlated relaxation rate R_{cc}, which in turn is related to the rotational correlation time τ_c by the following set of equations:

$$R_\beta - R_\alpha = R_{cc} = 2p\delta_N\big(4J(0) + 3J(\omega_N)\big)(3cos^2(\theta) - 1)$$

$$p = \mu_0\gamma_H\gamma_N h/(16\pi^2\sqrt{2r_{HN}{}^3}) \qquad (7)$$

$$\delta_N = \gamma_N B_0 \Delta\delta_N/(3\sqrt{2})$$

$$J(\omega_N) = 0.4\tau_c/(1 + (\tau_c\omega_N)^2)$$

Here p is the dipolar coupling between nitrogen and proton, δ_N the chemical shift anisotropy of nitrogen, J the spectral density function, ω_N the nitrogen frequency, ϑ the angle of the nitrogen chemical shift tensor with the N-H bond, μ_0 the permittivity of vacuum, γ_H and γ_N the gyromagnetic ratios of proton and nitrogen respectively, h plancks constant, r_{HN} the H-N internuclear distance, B_0 the magnetic field strength and $\Delta\delta_N$ the difference between the principle components of the nitrogen chemical shift tensor. The relaxation rates are measured by increasing the time interval in which relaxation effects take place. At a certain delay time the signal has completely decayed to zero intensity.

The obtained decays of the proton intensities of the peaks at 7.8 and 8.2 ppm are shown in Figure 38a and b respectively. A mono-exponential decay was used to fit the data points where the pre-exponential factor and the relaxation rate R are used as fit parameters. From the obtained values for the relaxation rates, rotation correlation times of 2.7 and 1.5 ns were calculated for V148 and V149 respectively. These rotation correlation times are three orders of magnitude faster than the τ_c of the order of microseconds that would be expected based on the size of the virus capsid. This can however be easily explained by the fact that these peaks originate from residues that are located in the C-terminal tail, which is often very flexible in the ns to ps timescale. In such mobile part of the protein the rotation correlation time is dominated by internal motion rather than the tumbling of the entire virus capsid. So the high mobility of the intense peaks further substantiates the idea that they correspond to C-terminal amino acids and simultaneously explains why these peaks could be observed in an HSQC experiment.

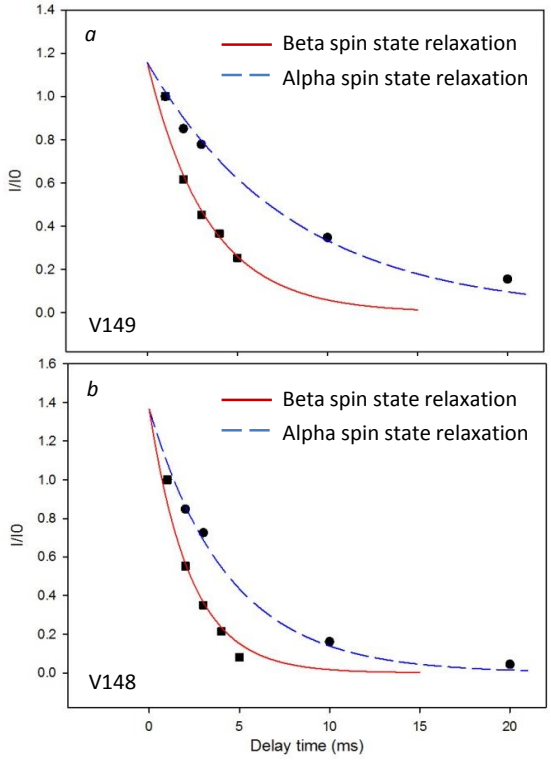

Figure 38. *Signal intensity decay at TRACT experiments for the amide proton at a) 7.8 ppm corresponding to V149 and b) 8.2 ppm corresponding to V148 and possibly T147. Signal intensity was normalized to the initial peak height. The figure shows that beta spins (red, squares) relax faster than the alpha spins (blue, circles).*

So the TRACT data show that the C-terminal tail is highly flexible in proteins that a part of the HBV capsid. Lack of observation of other peaks that correspond to the capsid however limits the amount of information that can be extracted from conventional dynamics measurements. Therefore we now propose a method to acquire information on protein mobility of very large complexes based on CRIPT. First we will briefly discuss the theory behind CRIPT and then will show how this experiment was used to obtain information on the dynamics of the 4 MDa HBV capsid.

CRIPT

There are two fundamentally different ways of achieving polarization transfer from one nucleus (e.g an amide proton) to its neighboring nucleus (e.g the amide nitrogen). The first and most commonly used is INEPT transfer that used J-coupling to turn in-phase magnetization on nucleus into anti-phase magnetization on the other nucleus. The efficiency of this process itself is independent of the size of the protein complex involved, but during the transfer period, the transverse magnetization will lose coherence in a size-dependent manner due to T_2-relaxation so that the overall transfer efficiency of INEPT decreases with protein size.

The alternative method is Cross-Relaxation Induced Polarization Transfer which was first introduced by Riek *et al.*[2] CRIPT uses the cross-relaxation between two nuclei. J-coupling is not the only connection between two neighboring nuclei, they also experience each other via dipole-dipole interactions (DD) and chemical shift anisotropy (CSA). Both interactions offer pathways via which relaxation can occur, so that the relaxation rates of both spins are coupled. That is, if either of the spins is out of equilibrium (which would be the consequence of interaction with a 90 degree radiofrequency pulse), also the other spin is perturbed. This connection will lead to the cross-relaxation process, where loss of coherence on the perturbed spin will lead to simultaneous buildup of magnetization on the connected nucleus. Like all relaxation processes, the rate of this effect increases with molecular size, or rather it decreases with effective rotation correlation time. Obviously, the newly created magnetization on the neighboring spin will be subject to relaxation as any other so that the overall transfer efficiency of CRIPT is given by

$$I_{antiphase} = I_0 \sinh(R_c \mathrm{T}) \exp(-R_H T) \qquad (8)$$

With $R_c = \frac{4}{15}(\gamma_H B_0 \Delta\sigma_H) * \left(\frac{\hbar\gamma_H\gamma_N}{r_{HN}^3}\right) * \tau_c$, and T represents the transfer time during which cross-relaxation can occur. Note that the cross- and auto-relaxation rates R_c and R_H always show up in combination with the transfer time. Both depend linearly on the effective rotation correlation time τ_c. The consequence is that there is an optimal transfer time for every given rotation correlation time, such that when the optimal transfer time is found, the overall transfer efficiency of this mechanism is in theory independent of the protein size. This is illustrated in Figure 39 that was copied from Riek *et al.* [2]. Note how the curve representing CRINEPT transfer combines the

principles of INEPT and CRIPT so that it should always yield better results than either of the two.

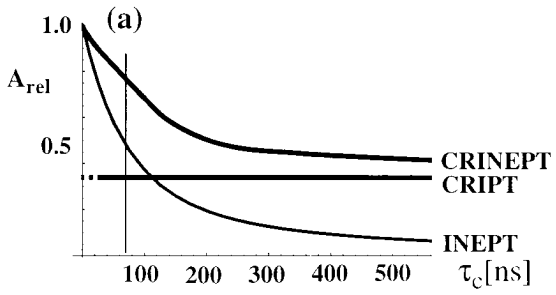

Figure 39. *Efficiency of magnetization transfer as function of effective rotation correlation time for three different magnetization transfer techniques: CRIPT, INEPT and CRINEPT. Note that CRIPT efficiency is in theory independent of size, where INEPT efficiency is much higher for small structures, but decreases to zero as* τ_c *increases.*

Another effect of the correlation between optimal transfer time and effective rotation correlation time is that a CRIPT experiment with a transfer time optimal for a large protein complex such as the virus capsid, will be suboptimal for a protein of different size so the free dimer signals are no longer observed in this experiment. Figure 40 shows that the dimer peaks are indeed not observed in the CRIPT experiment.

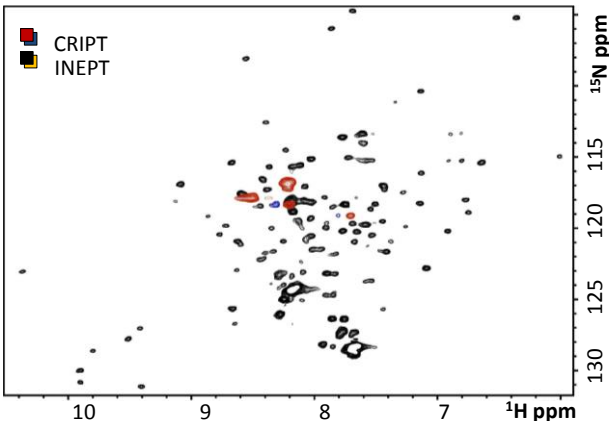

Figure 40. *Overlay between [*^{1}*H,*^{15}*N]-correlation spectra of the Hepatitis B virus capsid sample using INEPT-TROSY transfer (black) and CRIPT-TROSY transfer (red). Both spectra are recorded in 1024 scans and 256 increments..*

We set out to investigate protein dynamics of the HBV capsid. Some signals emanating from this 4 MDa complex were observed using the CRIPT experiment, but extending the duration of this experiment to obtain information on the effective rotation correlation times would inevitably lead to loss of signal intensity due to large relaxation rates.

Instead we propose a method to employ the size dependence of the optimal transfer time to measure an effective rotation correlation time for every observed peak. Since the effective rotation correlation time consists of a component related to the overall tumbling of the protein and a component that accounts for internal mobility, as described by equation 9, this value will yield qualitative information on the dynamics of the residue that the measured peak emanates from.

$$\tau_{c,eff} = \frac{\tau_{c,overall} * \tau_{c,internal}}{\tau_{c,overall} + \tau_{c,internal}} \qquad (9)$$

To this means we measured a series of 1D CRIPT spectra where we varied the magnetization transfer time T. This experiment can be considered an optimization process as the observed peak intensity varies with transfer time. Figure 41 shows the obtained spectra and one can see that the optimal transfer time is different for the different peaks, and hence the effective rotation correlation time must be too. Since all peaks should come from the virus capsid and the overall tumbling is consequently identical for all peaks, the difference in $\tau_{c,eff}$ can only be due to a difference in internal dynamics. Reason for the strong negative signals is that this 1D-CRIPT experiment acquires anti-phase magnetization that due to a difference in intensity could not be phased correctly.

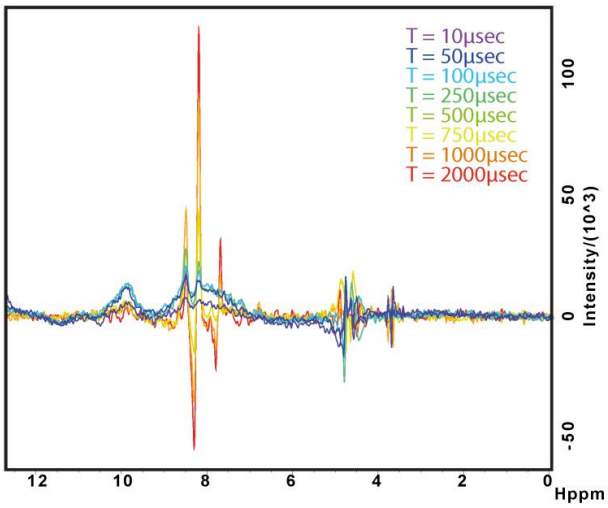

Figure 41. *Series of 1D CRIPT experiments with varying transfer times. One can see that different peaks have different optimal transfer times indicating a difference in their internal dynamics. Spectra were recorded in 6k scans.*

To obtain a value for the effective rotation correlation time corresponding to each of the observed peaks, the measured intensity was plotted as function of the transfer time, as can be seen in Figure 42. A value for $\tau_{c,eff}$ can be found by fitting the curve of the theoretical transfer efficiency as function of transfer time, based on equation 50. One can see that there is variation in the calculated effective rotation correlation of two orders of magnitude. Apparently the $\tau_{c,eff}$ of residue corresponding to the peak at 7.8 ppm is dominated by the internal flexibility, indicating that it is located in a very mobile part of the protein. The broad peak at 10 ppm though has a rotation correlation time of the order of microseconds, similar to the theoretical value for $t_{c,overall}$ of 3 to 6 µs, corresponding to a capsid with an effective molecular weight of 20 MDa. This indicates that the residue(s) corresponding to this 10 ppm signal are rigid.

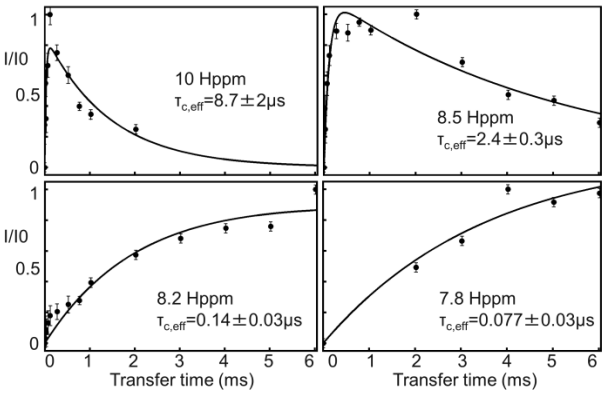

Figure 42. *Signal intensity as function of the CRIPT transfer time per observed peak. Values for* $\tau_{c,eff}$ *were obtained by curve-fitting.*

Concluding remarks

Coming back to the primary question, whether there are dynamics in the HBV capsid that can explain the entropy contribution to the self-assembly process, we found that the C-terminal tail of the HBV capsid is highly flexible. Based on a CRIPT based dynamics measurements we can also conclude that there are no other regions in the coat protein with flexibility with timescales on the order of or faster than microseconds, once it has assembled. If such fast mobility would have been present, the effective rotation correlation time of the corresponding residues would have been such that they could have been observed using the CRIPT experiment. Connecting this finding to the crystal structure of Cp149, it would make sense that the C-terminal tail is the region that increases flexibility on assembly. It is closely attached to the hydrophobic attraction pockets that become buried on assembly. Hence one could expect that the tail has to fold away to achieve this, thereby becoming extended and increasing flexibility. This is however only speculation and the dynamics of the C-terminal tail of the unassembled dimer have to be characterized before further conclusions on this can be drawn.

Furthermore we found indications for exchange between dimers free in solution and dimers as part of the capsid based on diffusion experiments. The exchange time was found to be of the order of seconds, which is fast compared to the timescale of a week required to reestablish the critical monomer concentration. A model of stochastic adsorption and release of dimers could explain this apparent discrepancy.

References

1. Pervushin, K., Riek, R., Wider, G. & Wüthrich, K. Attenuated T2 relaxation by mutual cancellation of dipole-dipole coupling and chemical shift anisotropy indicates an avenue to NMR structures of very large biological macromolecules in solution. *Proc. Natl. Acad. Sci. U. S. A.* **94,** 12366–71 (1997).

2. Riek, R., Wider, G., Pervushin, K. & Wüthrich, K. Polarization transfer by cross-correlated relaxation in solution NMR with very large molecules. *Proc. Natl. Acad. Sci. U. S. A.* **96,** 4918–23 (1999).

3. Kegel, W. K. & Schoot Pv, P. Van Der. Competing hydrophobic and screened-coulomb interactions in hepatitis B virus capsid assembly. *Biophys. J.* **86,** 3905–13 (2004).

4. Ceres, P. & Zlotnick, A. Weak Protein-Protein Interactions Are Sufficient To Drive Assembly of Hepatitis. **4,** 11525–11531 (2002).

5. Wynne, S. a, Crowther, R. a & Leslie, a G. The crystal structure of the human hepatitis B virus capsid. *Mol. Cell* **3,** 771–80 (1999).

6. Zlotnick, a *et al.* Dimorphism of hepatitis B virus capsids is strongly influenced by the C-terminus of the capsid protein. *Biochemistry* **35,** 7412–21 (1996).

7. Wingfield, P. T., Stahl, S. J., Williams, R. W. & Steven, a C. Hepatitis core antigen produced in Escherichia coli: subunit composition, conformational analysis, and in vitro capsid assembly. *Biochemistry* **34,** 4919–32 (1995).

8. Freund, S. M. V, Johnson, C. M., Jaulent, A. M. & Ferguson, N. Moving towards high-resolution descriptions of the molecular interactions and structural rearrangements of the human hepatitis B core protein. *J. Mol. Biol.* **384,** 1301–13 (2008).

9. Salzmann, M., Pervushin, K., Wider, G., Senn, H. & Wüthrich, K. TROSY in triple-resonance experiments: new perspectives for sequential NMR assignment of large proteins. *Proc. Natl. Acad. Sci. U. S. A.* **95,** 13585–90 (1998).

10. Horst, R., Horwich, A. & Wüthrich, K. Translational diffusion of macromolecular assemblies measured using transverse-relaxation-optimized pulsed field gradient NMR. *J. Am. …* **133,** 16354–16357 (2011).

11. Lee, D., Hilty, C., Wider, G. & Wüthrich, K. Effective rotational correlation times of proteins from NMR relaxation interference. *J. Magn. Reson.* **178,** 72–6 (2006).

12. Hedin, N., Yu, T. Y. & Furo, I. Growth of C 12 E 8 Micelles with Increasing Temperature. A Convection-Compensated PGSE NMR Study. 7548–7550 (2000).

13. Jerschow, a. Thermal convection currents in NMR: flow profiles and implications for coherence pathway selection. *J. Magn. Reson.* **145,** 125–31 (2000).

14. Brand, T. *et al.* Residue-specific NH exchange rates studied by NMR diffusion experiments. *J. Magn. Reson.* **187,** 97–104 (2007).

Appendix

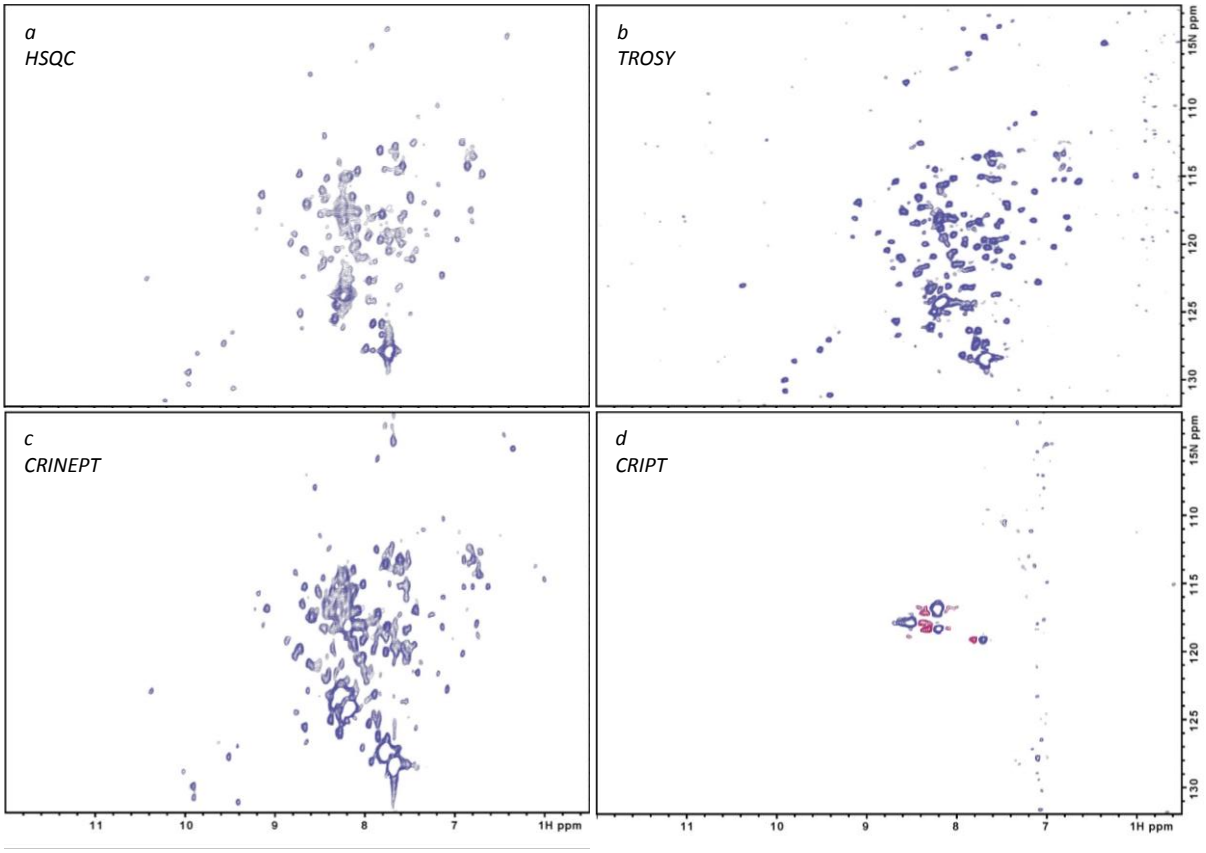

Figure 43. *Comparison between HSQC (a), TROSY (b), CRINEPT (c) and CRIPT (d) spectra of the HBV virus capsid. All spectra were recorded in 1k scans and 256 increments on a BRUKER AVANCE Spectrometer operating at 900MHz. Time for magnetization transfer was* $1/J_{NH}$ *in all experiments to be optimal for INEPT transfer except for the CRIPT where the delay was 1.5ms.*

3.2 Relaxation of the HBV capsid NMR signals

Despite the application of TROSY and CRIPT, only few peaks that corresponded to the HBV capsid could be observed, meaning that at least 140 are still absent, even if all proteins absorbed in the virus are identical. The following section will describe considerations why these peaks could not be observed.

In general two reasons can cause a lack of signal in (properly set up) NMR experiments. Either the magnetic coherence relaxes away before it can be acquired due to very fast T_2 relaxation, a process that has already been extensively discussed, or the magnetization becomes saturated as a consequence of very slow T_1 relaxation.

Where T_2, or transverse, relaxation causes loss of signal because it dephases the magnetization, T_1 (longitudinal) relaxation causes the magnetization to relax back to the equilibrium position, that is aligned with the z-magnetic field. As such T_1 relaxation determines the time required between scans to start again with z-magnetization. If one waits shorter than the T_1 relaxation time, only part of the magnetization has relaxed back to the z-axis and hence only part of the signal will be obtained. The remaining magnetization will remain dephased.

T_1 relaxation is like T_2 relaxation caused by fluctuations in the magnetic field due to Brownian motion. Small fluctuations in the x- and y-magnetic field will act as small radiofrequency pulses and rotate the magnetization from the xy-plane back to the z-axis. This process is most efficient when the frequency of the pulses matches the frequency of the rotation of the protein. As such there is a minimum in the T_1 relaxation time, as can be seen in Figure 44

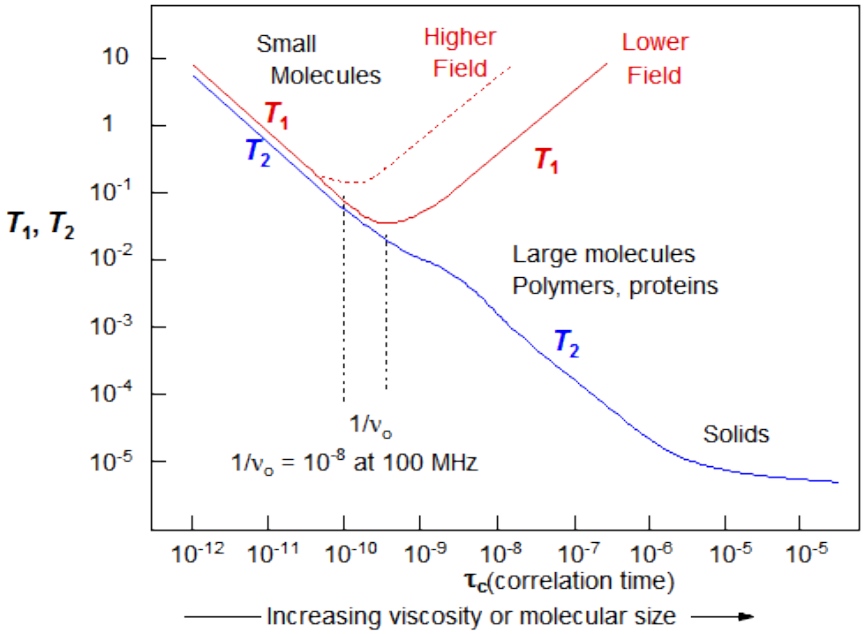

Figure 44. *Schematic of variation of the T_1 and T_2 relaxation times as function of the rotation correlation time. The HBV capsid has an estimated rotation correlation time of the order of microseconds, so the T_2 relaxation time should be of the order of milliseconds and the T_1 relaxation time could be tens of seconds. So the magnetization is almost instantaneously dephased and takes a long time to relax back to equilibrium magnetization.*

Longitudinal Relaxation

In common biomolecular NMR experiments an interscan delay of 1 second is enough to ensure that the largest part of the magnetization has returned to the z-axis, but *Figure 44* shows that for the HBV capsid (with an overall tumbling time of 3-6 microseconds) the T_1 relaxation time could be an order of magnitude longer. A simple way to see this would be to elongate the interscan delay and see if the signal intensity indeed increases

with time. This appears to be the case, but there is a practical limit on the interscan delay that can be used when measuring proton signals, that is related to water suppression. During most experiments water signal is saturated, but with interscan delays of more than 2 seconds the water signal also has time to relax back and interferes so strongly with the spectra that no other signal can be observed. To still get an estimate of the T_1 relaxation and to what extend magnetization saturation is responsible for the absence of capsid signals, we performed 1D ^{13}C NMR spectra with interscan delays of 1 s, 10 s and 60 s. The results are shown in Figure 45 and reveal that the T_1 relaxation time of residues in the HBV capsid are indeed considerably longer than seconds.

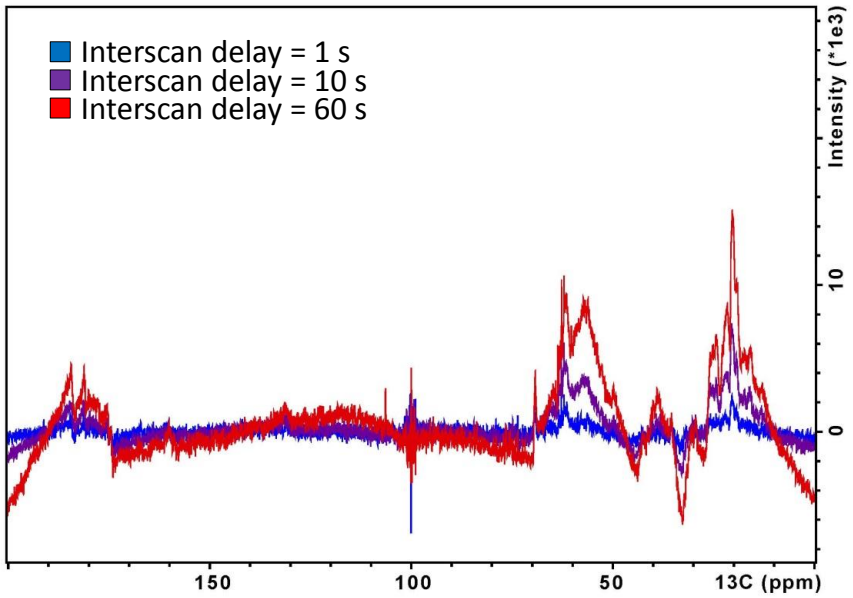

Figure 45. *Overlay of 1D 13C spectra recorded with variable interscan delay. All spectra are recorded in 1024 scans with an acquisition time of 0.39 seconds. It shows that longer interscan delays lead to larger peak intensity, implying that the T_1 relaxation time is at least larger than 10 seconds. The peaks represent from left to right carboxyl groups, C_α's and C_β's.*

To obtain an estimate of the T_1 relaxation time of the HBV capsid, the peak integral is plotted as function of the interscan delay. In order to predict how the peak intensity depends on the relaxation time we use the Bloch equation (eq. 10), which states that the increase of z-magnetization depends on the number of spins out of equilibrium

$$\frac{\partial M_z}{\partial t} = \frac{M_0 - M_z}{T1} \tag{10}$$

Here M_z is the instantaneous z-magnetization and M_0 the equilibrium z-magnetization. This first order differential equation can easily be solved to find that

$$M_z = M_0[1 - e^{-\frac{t}{T1}}] \tag{11}$$

If we now neglect the contribution of the first scan, for which the interscan delay is in principle infinite, we find that the peak intensity should than be related to the interscan delay as

$$I(t) = I(t = \infty) * [1 - e^{-\frac{t}{T1}}] \tag{12}$$

Figure 46 shows the fit of equation 12 to the peak integrals of the spectrum shown in *Figure 45*, where T1 is used as a fit parameter. From the fit the T_1 relaxation time appears to be of the order of 13-18 seconds, which indeed roughly corresponds to the value that would be expected from *Figure 44*.

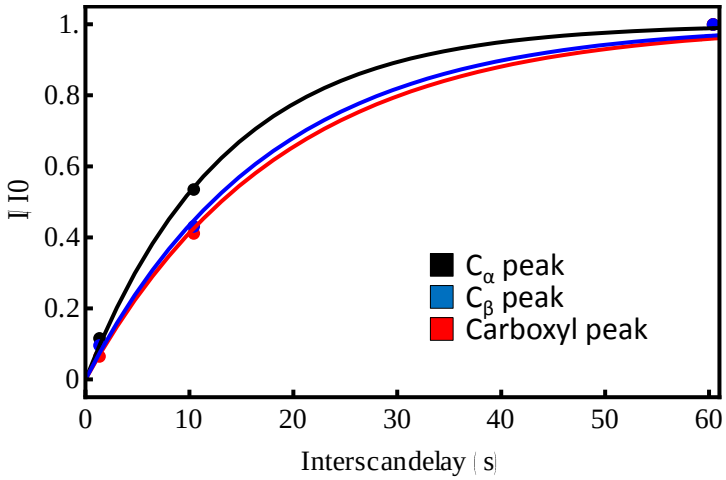

Figure 46. *Fit of the peak intensity as function of interscan delay as consequence of T1 relaxation. Peak integrals were measured in the carboxyl region (174-195 ppm), C_α region (45-70ppm) and C_β region (9-28 ppm). The T_1 relaxation time was used as fit parameter and appears to be in between 13 (for C_α) and 18 (for carboxyls) seconds. The experimental time of 0.39 s was also taken into account.*

Transverse Relaxation

So the extremely long T_1 relaxation times definitely account for part of the problem, but even at an interscan delay of 1 s, some signal should be observed. The other reason that could explain the lack of signal was fast loss of coherence. Although CRIPT and TROSY minimize transverse relaxation during acquisition and magnetization transfer, signal can still be lost there or during the nitrogen chemical shift evolution. To assess the scale of the signal loss during these experimental phases, we make a rough estimate of the T_2 relaxation time using the following equations:

$$\Delta\nu_{1/2} = \frac{1}{\pi * T2} \tag{13}$$

$$\frac{1}{T2} = 2\,\gamma^2 < B >^2 \left(\tau_c + \frac{\tau_c}{1 + (\omega_0 \tau_c)^2}\right) \tag{14}$$

Since we know the peak width for the dimer (21 Hz) we can calculate the corresponding transverse relaxation time, which appears to be 15 ms using equation 13. Based on its weight and the Stokes equation we can estimate the rotation correlation time of the dimer to be 9.4 ns. From equation 14 we can then get the squared average fluctuations in the magnetic field $<B>^2 = 4.9*10^{-8}\ T^2$.

When we now use the value for the rotation correlation time of the complete capsid (3 µs), we find a transverse relaxation time of only 42 µs, which is again in correspondence with the value for T2 of 10^{-5} s given in Figure 44 for a structure with a tumbling time of microseconds. This means that signal is lost almost instantaneously compared to the timescale of any NMR experiment. Compare this time for example to the duration of a 180 degree pulse which is of the order of 22 µs. So even for transverse relaxation optimized pulse sequences using CRIPT as method for magnetization transfer, a significant fraction of the magnetization is lost due to finite length of pulses and during nitrogen chemical shift evolution in a 2D experiment.

The spectra with a CRIPT transfer time of 100 and 50 µs in *Figure 41* show two peaks that are much broader than the other peaks observed. These might be the overlapping signals of all residues in the protein core for which CRIPT transfer should become efficient at these transfer times. To check if this is indeed the case a [^{1}H,^{15}N] correlation spectrum was recorded with a CRIPT transfer time of only 100 µs (see *Figure 47*). A complicating factor is the nitrogen chemical shift evolution, where the number and duration of time increments relates directly to the resolution in the nitrogen direction. Tens of increments of as long as 300 µs are usual, but for such long delay signal is lost quickly and hence we only took 12 increments in the nitrogen direction, leading to poor resolution. Also the water flip-back pulses required for water suppression had to be

removed, since their duration is about a millisecond. The resultant poor water suppression combined with lack of resolution in the nitrogen dimension lead to a noisy spectrum with exceptionally broad peaks. However, the fact that those peaks are also visible in the 1D analogue of this spectrum, where water suppression is considerably better, implies that they are indeed real signals. This raises the question to which residues they correspond. Especially the signal at 10 ppm is surprising, since this would correspond to tryptophan side chain amides, but there is no reason that this tryptophan would be observed and not any other signal.

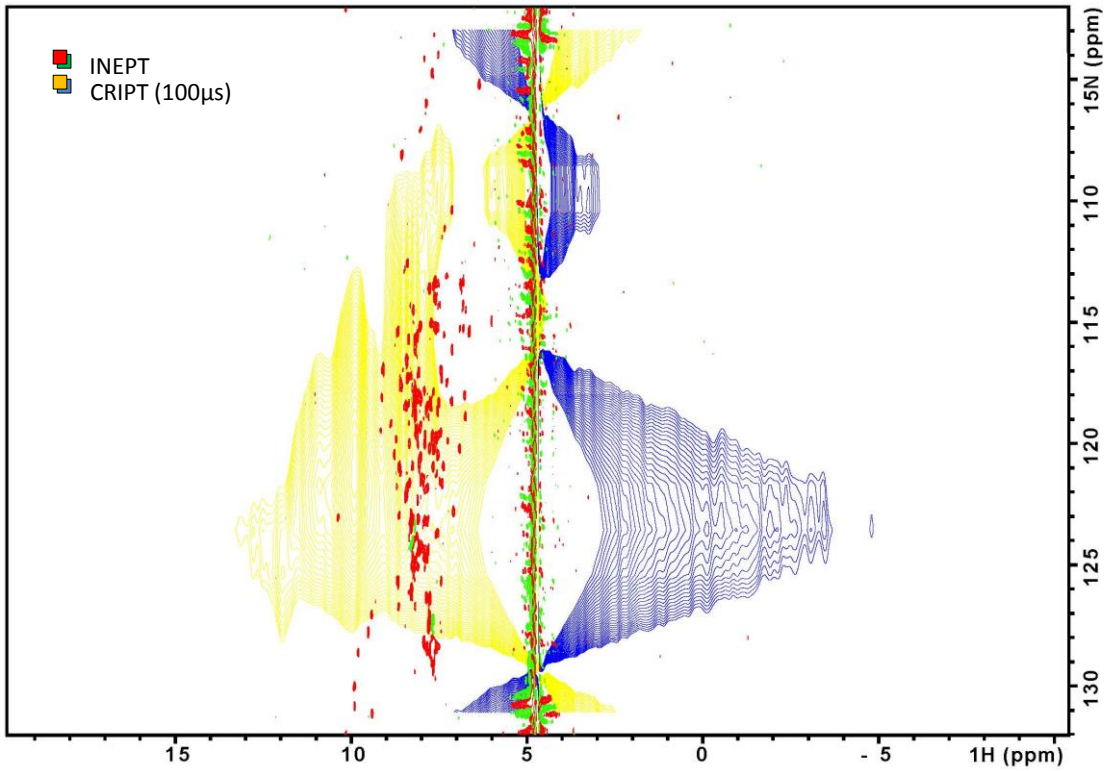

Figure 47. *Overlay of [^{1}H,^{15}N]-correlation spectra using CRIPT and INEPT transfer. The CRIPT transfer time was 100 µs, which was estimated to be optimal for transfer of rigid residues in the HBV capsid. Inept transfer time was 2.7 ms. We expect the broad signal in the CRIPT spectrum to be overlap between all residues of the HBV capsid.*

Attempts to improve water suppression were made through the usage of jump-return pulses. This is a set of two orthogonal 90 degree pulses with a delay in between, that is optimized to rotate water magnetization exactly 90 degrees. The result is that water will be flipped back to the z-axis and magnetization from residues at a different chemical shift, such as amide protons, will not be flipped back. The net result is a 90 degree pulse that flips magnetization into the xy-plane except for water magnetization. This would be a method to further investigate since it would also prevent saturation of the water magnetization so that it allows for long interscan delays.

Conclusion

So the lack of signals from rigid residues of the HBV capsid is a consequence of both their extremely long T_1 relaxation and their short T_2 relaxation. T_1 relaxation is in theory easily overcome by increasing the interscan delay, but this also leads to very strong water signals that interfere with the rest of the spectrum. T_2 relaxation is a problem that is less easily overcome, but the shorter the experiment, the more signal could be obtained. Again, shortening experiments in practice means compromising on the water suppression. For this reason jump return pulses could be a valuable tool to improve the quality of the HBV capsid spectra.

3.3 Diffusion-TROSY shows proton exchange in flexible regions of Ubiquitin

Biomolecular NMR spectroscopy allows for the accurate measurement of diffusion rates of proteins and protein complexes using the so called DOSY (Diffusion Ordered SpectroscopY) experiment. This is basically a series of 1D experiments where the decay in signal intensity over the series is a measure of the diffusion coefficient. The experiment is well-suited for measuring the average diffusion of a single compound, but when dealing with a mixture of components of different sizes, it often lacks the resolution to distinguish between the different complexes. Several experiments have already been developed to increase the resolution by adding a nitrogen or carbon dimension, such as the DOSY-HMQC[1] and the DOSY-HSQC [2]. We present an experiment that combines this type of three-dimensional diffusion spectroscopy with TROSY (TRansverse Optimized SpectroscopY) into a diffusion-TROSY, which is different from TROSTE in a way that it also records the ^{15}N chemical shift evolution. This experiment can in theory be used to obtain accurate and independent diffusion coefficients for every peak in a TROSY spectrum. In this way spectra of mixtures of large protein complexes can be analyzed without physically separating them by assigning peaks to either of the protein complexes based on measured diffusion coefficients.

In order to measure the diffusion coefficient of every peak in a TROSY spectrum the pulse sequences of a DOSY and a TROSY [3] are combined. A graphical representation of the pulse program is shown in Figure 17. The diffusion-decoding period and the magnetization transfer from proton to nitrogen of the TROSY have been merged to shorten the experiment slightly. This experiment is a pseudo-3D experiment so it is recorded as a series of 2D experiments. The result is a set of TROSY planes where the decay of the peak intensities yields information about the diffusion coefficient in a similar manner as for an ordinary DOSY experiment. To prevent artifacts in the diffusion coefficient arising from the long measurement times, the incrementation order that was uses was first the diffusion delay Δ and then the chemical shift evolution period d_0 . The result is an experiment that measures chemical shift of both proton and nitrogen and for every peak in the [^1H,^{15}N]-correlation spectrum it yields a diffusion coefficient. Note however that both DOSY and TROSY only have an efficiency of 50 %, so this experiment can maximally give 25 % of the signal intensity of an HSQC.

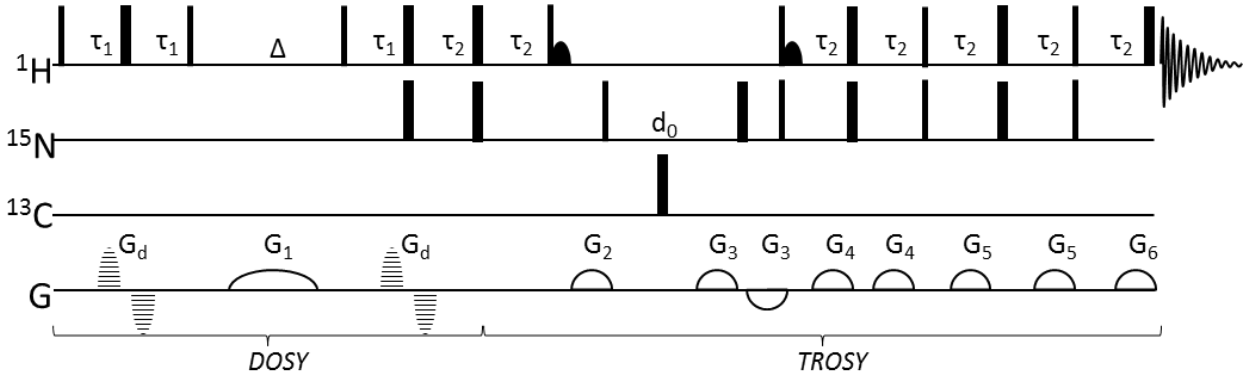

Figure 48 *Pulse sequence of a diffusion TROSY. Thin black bars represent hard 90 degree pulses, thick black bars 180 degree pulses. The small black hemispheres are water flip-back pulses. The white hemispheres are gradient pulses and the striped bullets are the encoding and decoding gradient pulses from the diffusion experiment. Delay d_0 is the incrementation delay in the nitrogen direction, $\tau_3 = \tau_1 + \tau_2$ and $\tau_2 = 1/2J_{NH}$. Δ Is the diffusion delay. Phase cycling: ϕ_1 = x, -x and ϕ_2 = 2(x), 2(-x). Receiver phase is x,-x,-x,x.*

The diffusion TROSY experiment has been tested on a highly concentrated solution (~2mM) of ubiquitin of which the diffusion coefficient had been measured before to check if the experiment yields reasonable results. The diffusion coefficient of ubiquitin can be estimated on its molecular weight assuming spherical shape and an

average density of 1.34g/mol. Then according to the Stokes-Einstein equation the diffusion coefficient of Ubiquitin should be 1.58m^2/s.

The experiment was performed at 298K at a BRUKER AVANCE III NMR spectrometer operating at 600MHz. The gradient strength of this spectrometer was calibrated and equaled 52.0 G/cm. A diffusion delay Δ of 100ms and a total encoding gradient length δ of 3200µs were used.

The diffusion decay of the peak corresponding to Arginine 42 (Arg42) gives a representative example of the decays that were observed for almost all ubiquitin signals and is shown in Figure 49. The y-axis shows the relative signal intensity and the x-axis is a measure of the gradient strength consisting of the proton gyromagnetic constant γ, the actual gradient strength g, a shape factor s (1/(2π) for a sine bell shaped gradient pulse), the gradient pulse length d (also δ) and the diffusion time t (also Δ).

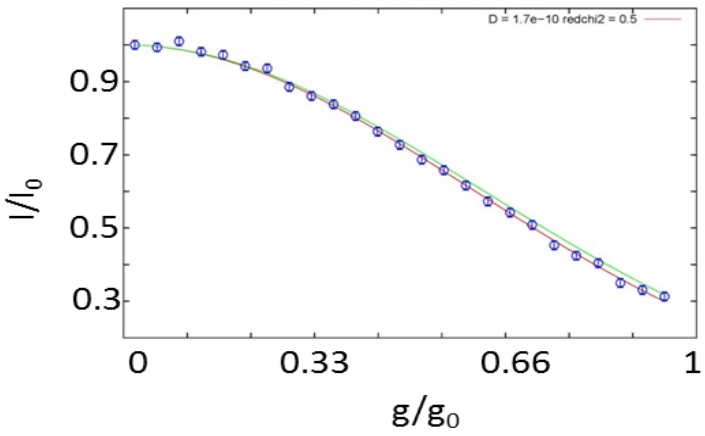

Figure 49. *Diffusion decay of the peak that corresponds to Ubiquitin Arg42. The error bar is represents the inverse of the signal to noise ratio. The red line is a fit of the Stesjkal-Tanner equation through the observed data points. The obtained diffusion coefficient is 1.7*10^{-10}m^2/s. The green line represents the theoretical prediction based on Stokes-Einstein of a diffusion coefficient of 1.6*10^{-10}m^2/s.*

As can be observed from *Figure 49*, the experiment works rather well. A diffusion coefficient was obtained that corresponds to the expected value based on the molecular weight of ubiquitin. The measured diffusion is on average slightly slower than the predicted. This is most likely due to the relatively high viscosity of a concentrated protein solution that was not accounted for in the theoretical calculation (viscosity of water was used).

There were some peaks that showed anomalous behavior. These correspond to residues Lys11, Thr12, Gly47, Leu73 and Gly76. The curve obtained from analysis of Leu73 signal intensities is shown in Figure 50.

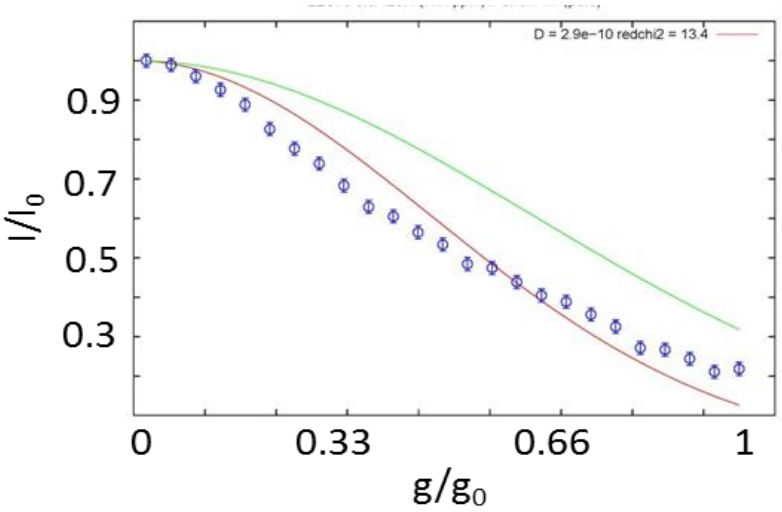

Figure 50. *Diffusion decay for Leu73. The error bar is represents the inverse of the signal to noise ratio. The red line is a fit of the Stesjkal-Tanner equation through the observed data points. The green line represents the theoretical prediction based on Stokes-Einstein of a diffusion coefficient of 1.6*10^{-10}m^2/s.*

The peak intensity of this residue seems to decay much faster than would be expected based on the molecular size. So it has a faster effective diffusion coefficient. Moreover the data cannot be described by a single exponential decay, because the fit matches the data points poorly.

All abovementioned abnormally behaving residues are located on known flexible loops in the protein and thus are not likely to have stable hydrogen bonds. This may cause the amide protons of these residues to exchange with water so that an effective diffusion is measured that is the combination of the diffusion of ubiquitin and that of water. In this case the data should be described by a linear combination of exponential decays [2].

$$\frac{I}{I0} = A * e^{-C*D_{ubiquitin}} + (1 - A) * e^{-C*D_{water}} \qquad (15)$$

Here C = $\sqrt{\gamma * g * s * \delta * (t - d/3)}$ and the pre-exponential factor A is used as fit parameter. It is a measure of the time an amide proton is attached to water. Using this bi-exponential equation to fit the data gives indeed a much better result as is shown in Figure 51.

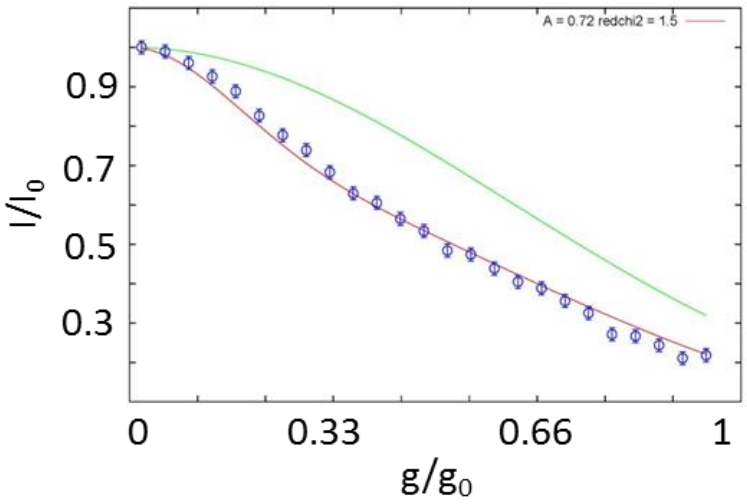

Figure 51. *Diffusion decay of Leu73 fitted by a bi-exponential decay combining the diffusion coefficient of water and ubiquitin. A value for fit parameter A of 0.72 was found indicating that Leu73 amide protons spent on average 38% of the measurement time attached to water.*

Apparently the exchange behavior of amide protons of residues in flexible parts of the protein influence their diffusion decay. The same observation was done by Brand *et al.*[2] who used a DOSY-HSQC (analogous to the diffusion TROSY, except it is not transverse relaxation optimized) experiment to measure the amide proton exchange rates based on their diffusion behavior. Surprisingly they found different residues showing proton exchange with water namely Thr9, Ala46, Arg74 and Gly75 [2]. These residues are situated in the same flexible loops as the residues that we found to behave anomalously, but the difference is in the pH of the used protein solutions. Where Brand *et al.* measured the exchange rates at pH=3 our protein solution has pH=8. It is well known that proton exchange, a base-catalyzed process, is faster at more alkaline pH. So at acidic pH Lys11, Thr12, Gly47, Leu73 and Gly76 may still have been in the slow exchange regime ($R_{exhange} < 1/\Delta$) and the effect of exchange on the diffusion coefficient may be negligible. But at more basic pH the exchange was accelerated and became of the same timescale as the diffusion experiment ($R_{exchange} \approx 1/\Delta$) so that the effect of proton exchange on the diffusion coefficient became observable.

But how does that relate to residues Thr9, Ala46, Arg74 and Gly75? Their diffusion coefficient was affected by proton exchange with water at low pH, but at higher pH the peaks corresponding to these residues were not observed whatsoever. Most likely the proton exchange, that was already in the fast regime at low pH, became so rapid in an alkaline solution that the signals coincide with the water signal due to fast exchange.

Although the diffusion TROSY allows for measurement of exchange rates of amide protons with water, this is an undesirable effect when attempting to measure accurate diffusion coefficients. Brand *et al.* suggested a method to prevent the effect of water exchange on the diffusion experiment by replacing the first 90 degree pulse by a selective amide pulse. We implemented this in TROSTE and Figure 52 shows that indeed the effect of proton exchange has disappeared.

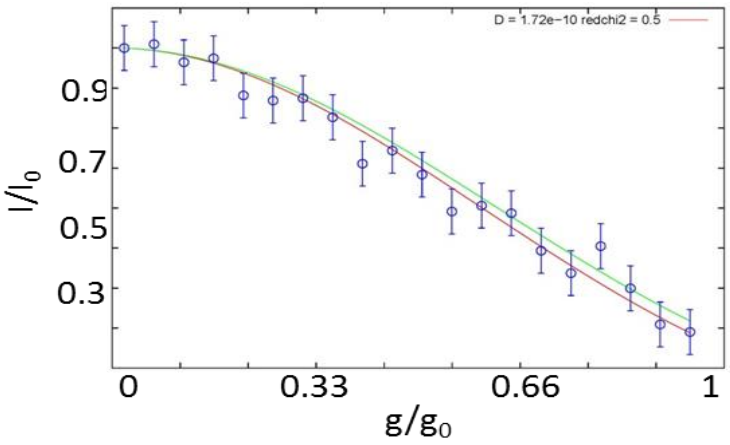

Figure 52. *Diffusion decay of Leu73 measured by an adapted version of the diffusion TROSY using a selective amide pulse to inhibit the effect of water exchange on the diffusion coefficient. Though the signal to noise ratio has decreased, the diffusion coefficient is indeed much more accurate.*

References

1. Didenko, T., Boelens, R. & Rüdiger, S. G. D. 3D DOSY-TROSY to determine the translational diffusion coefficient of large protein complexes. *Protein Eng. Des. Sel.* **24,** 99–103 (2011).

2. Brand, T. *et al.* Residue-specific NH exchange rates studied by NMR diffusion experiments. *J. Magn. Reson.* **187,** 97–104 (2007).

3. Pervushin, K., Riek, R., Wider, G. & Wüthrich, K. Attenuated T2 relaxation by mutual cancellation of dipole-dipole coupling and chemical shift anisotropy indicates an avenue to NMR structures of very large biological macromolecules in solution. *Proc. Natl. Acad. Sci. U. S. A.* **94,** 12366–71 (1997).

3.4 Calibration of z-magnetic gradient

Pulsed magnetic gradients are abundantly used in bio-molecular NMR experiments. They are used as clean-up gradients to dephase unwanted magnetization, in water suppression and in diffusion experiments. As previously discussed the signal attenuation in a diffusion experiments follows the Stesjkal-Tanner equation and the signal intensity scales with the exponent of the gradient strength squared

$$S/S_0 = Exp\left[-D\delta^2 g^2 \gamma^2 \left(\Delta - {}^{\delta}/_{3}\right)\right] \quad (16)$$

Calculation of the diffusion coefficient from a diffusion NMR experiment requires a fit of the Stesjkal-Tanner equation, where all variables, including the magnetic gradient strength g, are known. Since the signal attenuation depends so strongly on the gradient strength, it is of utmost importance that this gradient strength is very accurately known. If one makes a 10% error in the estimate of the gradient strength (it is not uncommon that the actual gradient strength deviates 10% from the value indicated by the producer), the diffusion coefficient will already be 20% off, highlighting the need for proper gradient calibration before engaging diffusion measurements.

Calibration of the z-magnetic gradient in NMR spectroscopy is quite straightforward and requires the acquisition of H_2O signal while the magnetic gradient is applied. The principle involved is described below. When measuring the NMR signal of water protons in absence of a magnetic gradient a peak will appear at approximately 4.7 ppm, a position that is determined by the rate of rotation of the proton magnetization. This precession rate depends amongst others on the strength of the z-magnetic field, as described by the Larmor frequency:

$$\nu = \gamma * B_z \quad (17)$$

It may be intuitive that upon application of a gradient in the z-magnetic field, the Larmor frequency of a spin will become dependent on its height in the sample. After all at different heights the spins will now experience a different magnetic field strength. As a consequence the obtained signal will no longer be a single peak at 4.7ppm but a broad square signal. Signal intensity on the left side of the peak arises from protons at one side of the sample where the z-magnetic field is lowest and intensity on the right side arises form protons at the other side of the sample. The top of the peak should be horizontal since the number of protons should be equally distributed over the sample, that is if the gradient over the sample is perfectly linear. Anomalous peak shapes arise from inhomogeneous magnetic gradients. Although these inhomogeneities may lead to artifacts, they will not affect the gradient calibration.

The width of the peak is a measure for the difference in magnetic field gradient between the upper and the lower part of the sample and as such can be measured by measuring the peak with at half height.

$$\Delta B_z = \frac{\Delta \nu_{1/2}}{\gamma} \quad (18)$$

To convert the difference in z-magnetic field strength to a gradient one only needs to divide by the height over which the gradient was applied by the gyromagnetic constant of protons. In particular two conditions should be met:

- The sample height should be smaller than the height of the coil, if the sample extends on either side of the coil, the height over which the gradient is applied depends on the height of the coil itself and this is hard to measure.

- A Shigemi tube should be used as container so that the height of the sample can be accurately set and measured. A sample height of approximately 1 cm is small enough to fit completely within the coil. The height should be measured accurately because an error in the height will translate directly to an error in the gradient strength.

The gradient strength g can then be calculated by dividing the difference in magnetic field by the height of the sample.

$$g = \frac{\Delta B_z}{h} \tag{19}$$

One should be aware of the fact that in most experiments a Sinc shaped gradient pulse is used. The integral of this shape is only 2/π of that of a square gradient pulse, since it is has a sine-bell shape.

So in practice the following steps are involved in calibration of the magnetic gradient

1) A Shigemi tube should be filled with tap water and the sample height should be set at approximately 1 cm. Measure the sample height accurately since it will be required in the calculation.
2) Insert the sample into the NMR spectrometer that requires gradient calibration and tune and match like for any other experiment. Also determine the length of the 90 degree proton pulse.
3) Open the experiment named [hvi_imgegp1d] (pulse program is shown in appendix) and fill in the required parameters. Important are a correct 90 degree proton pulse length, a proper spectral width (for large gradients the peak will be too wide to fit in the default spectral width), the shape of the gradient pulse, and the gradient strength.
4) The gradient strength parameter is indicated as a percentage of the maximum gradient strength. Start by using a gradient of 1% and repeat the experiment for gradients of 2%, 5%, 10%, 20% and 50%.
5) For each experiment, measure the peak width and use equations 3 and 4 to calculate the gradient strength.
6) Plot the experimentally determined gradient strength as function of the percentage of the maximal gradient that was applied and extrapolate to a gradient of 100%. (Multiply the obtained gradient strength by π/2 to correct for the shape if a sine-shaped gradient pulse was used.) This is the value of the gradient strength that we set out to determine.

The graph obtained for gradient calibration of the BRUKER AVANCE NMR spectrometer operation at 600MHz is shown in Figure 53. The gradient strength is determined from the slope. The standard deviation linearly relates to the root mean squared deviation. A line was fitted through the experimental data where the slope is used as fit parameter. A peak width at half height of 493.24 ± 8.29 kHz for a magnetic gradient strength of 100% was found. That relates to a gradient strength of 28.9 ± 0.48 G.

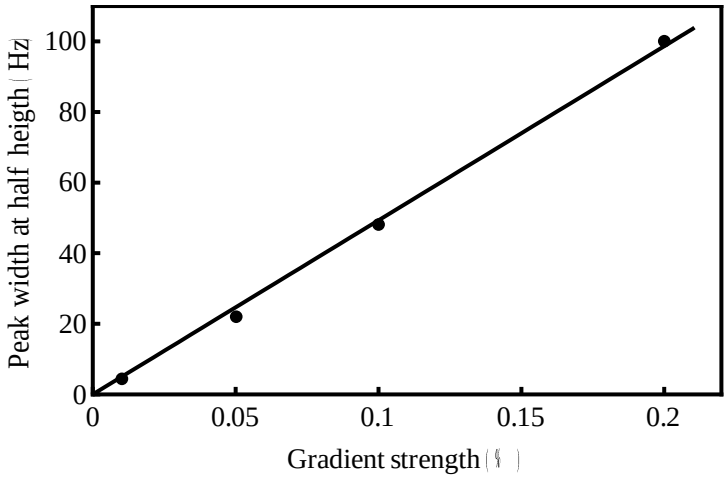

Figure 53. *Calibration of z-magnetic gradient. Dots represent the experimental peak width at half height at different gradient strength. The line is a linear fit through the experimental data, of which the slope relates to the z-magnetic gradient.*

3.5 Theory of bio-molecular NMR experiments

The results that were presented in this chapter are almost exclusively based on solution state NMR experiments. Purpose of this section is to provide some theoretical background on those experiments[1] and indicate what measures are taken to optimize them for the application to very large protein structures.

As the name already implies NMR spectroscopy is indeed a spectroscopy technique, meaning that it monitors the interaction between electromagnetic waves and matter, the latter of which are atomic nuclei in the case of NMR. All nuclei have small magnetic moment, called magnetic spin, that is under normal circumstances randomly orientated. When such atom is placed in a large magnetic field however the spins will align with this field in either parallel or antiparallel direction. It is the difference between parallel and antiparallel aligned nuclear spins (parallel is slightly more energetically favorable) that leads to the formation of a net magnetization in the direction of the external field. NMR spectroscopy measures the response of this magnetization on light, or more specifically to radiofrequency pulses.

The energy of the transition of z-oriented magnetization to transverse magnetization is such that it can be induced through interaction with radiofrequency waves. Almost every solution state NMR experiment starts with such excitation event effected by a radiofequency pulse that flips the z-magnetization into the xy-plane, in short referred to as a 90 degree pulse. The thus obtained transverse magnetization rotates in the xy-plane with a frequency that is directly related to the magnetic field strength. This rotation is the NMR observable and it is affected by the chemical environment because the chemical nature of the surroundings of an atom determines to which extend it is shielded from the z-magnetic field. This shielding hence affects the rate of rotation and this is in turn observed as a chemical shift. So large shielding by electronegative species gives a large chemical shift.

In the simplest possible NMR experiment the chemical shift of all protons (or any other nucleus) is measured by applying a 90 degree pulse and recording the rotation of the transverse magnetization. This type of experiment can be extended to measure the chemical shift of both a proton and its neighboring nitrogen in a single [^{1}H,^{15}N]-correlation spectrum. In such experiment first transverse proton magnetization is created through a 90 degree pulse and is transferred to the nitrogen. Then during a waiting period the nitrogen chemical shift gives a modulation on the signal, that is transferred back to proton and recorded as proton magnetization.

If the magnetization would continue to rotate in the xy-plane, the resolution of NMR spectroscopy would be infinite, but in reality the signal decays over time due to relaxation events. Hence the observed oscillating signal is called a Free Induction Decay or FID that is converted to a peak at a certain chemical shift by Fourier transformation. There are two types of relaxation that cause the signal intensity to decrease over time: longitudinal or T_1 relaxation, which is the slow back rotation of the magnetization to the z-axis where it is aligned with the magnetic field, and transverse relaxation or T_2. To understand the latter, one needs to realize that the observed magnetization is the sum of an ensemble of spins. As these spins experience a slightly different field due to random interaction with the environment that changes continuously due to Brownian motion, they rotate at slightly different rates causing them to dephase. When coherence between the spins is lost the ensemble average gives a net zero magnetization and the signal has decayed to zero. Both transverse and longitudinal relaxation rates depend on the tumbling time of the observed structure, because both effects are causes by interaction with the surroundings. For a quickly rotating molecule these random interactions are largely averaged out in time causing slow relaxation. For a large protein structure that has almost no rotation, the interactions are much less efficiently averaged out, leading to quick relaxation.

In the following section we will discuss several [^{1}H,^{15}N]-correlation experiments, with and without relaxation optimization to tailor the experiment for measurement of very large structures. We will describe to

[1] Information that is not experiment-specific is based on the textbook *Protein NMR Spectroscopy* [5]

fundamentally different ways of transferring magnetization between nuclei of which again one is more suitable for application to large proteins than the other. Finally we will deal with diffusion NMR spectroscopy, an experiment where the signal is modulated as a consequence of Brownian motion, so that diffusion coefficients can be measured.

HSQC

Arguably the most commonly used experiment in biomolecular NMR is the [^{1}H,^{15}N]-HSQC (Heteronuclear Single Quantum Coherence) experiment, which shows the correlation between proton and nitrogen magnetic spins. The resulting spectrum is often referred to as protein fingerprint, because it is unique for every protein. The spectrum is dominated by peaks originating from amide bonds, but also shows proton nitrogen correlations of amide containing amino acid sidegroups, such as glutamine and asparagine. So apart from the sidegroup peaks every signal in an HSQC experiment corresponds to one amino acid. And vice versa every amino acid produces one peak in an HSCQ spectrum, with the exception of proline that does not have an N-H bond. This type of experiment is particularly useful when the NMR assignment of a certain protein is available, that is if one know for every peak in the spectrum exactly to which amino acid it corresponds to. Such assignment can be obtained using a combination of several triple resonance experiments that will be discussed later on. With the assignment available HSQC experiments can be used to do NMR titrations. For example adding a certain chemical that your protein of interest interacts with, will change the chemical environment of the particular residues that are involved in the interaction, leading to a chemical shift perturbation that is observable in the HSQC spectrum. This type of experiments gives information on which residues are involved in the interaction and they can be used to roughly estimate an interaction strength.

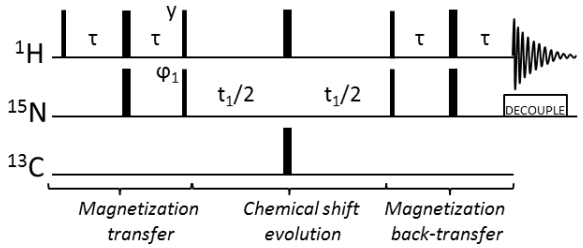

Figure 54. *HSQC pulse sequence used to obtain a proton nitrogen correlation spectrum. Decoupling on nitrogen is applied during acquisition. Thin bars represent 90 degree pulses (π/2) and thick bars represent 180 degree pulses (π). All pulses have phase x unless otherwise indicated. A simple phase cycle to ensure that the measured magnetization has gone via nitrogen is ϕ_1=x,-x and receiver phase ϕ_r=x,-x.*

A basic pulse program for a [^{1}H,^{15}N]-HSQC on a triple labeled sample is shown in Figure 54. It consists roughly of four elements: magnetization transfer from proton to nitrogen, chemical shift evolution on the nitrogen, magnetization back transfer to proton and finally acquisition on the proton channel. Usually pulse sequences also contain a set of gradient pulses to suppress signal from water and dephase unwanted polarization. We focus however on the basic requirements to obtain an HSQC spectrum. The transfer of magnetization during the full pulse program is described below.

Flip of proton z-magnetization to the xy-plane

$$H_z \xrightarrow{\frac{\pi}{2}(H_x)} H_y$$

Magnetization transfer to nitrogen via INEPT (Insensitive Nuclei Enhanced Polarization Transfer)

$$H_y \xrightarrow{\omega_H \tau} \xrightarrow{2\pi J_{NH} \tau H_z N_z} \xrightarrow{\pi(H_x)} \xrightarrow{\pi(N_x)} \xrightarrow{\omega_H \tau} \xrightarrow{2\pi J_{NH} \tau H_z N_z}$$

$$H_y \xrightarrow{\pi(H_x)} \xrightarrow{\pi(N_x)} \xrightarrow{4\pi J_{NH} \tau H_z N_z}$$

$$H_y \xrightarrow{\pi(H_x)} \xrightarrow{\pi(N_x)} -H_y \xrightarrow{4\,\pi\,J_{NH}\,\tau\,H_zN_z} -H_y\cos(2\pi J_{NH}\tau) - 2H_xN_z\sin(2\pi J_{NH}\tau)$$

In the case $\tau = \frac{1}{4J_{NH}}$ the sine term equals one and the cosine term disappears giving

$$-2H_xN_z \xrightarrow{\frac{\pi}{2}(H_y)} -2H_zN_z \xrightarrow{\frac{\pi}{2}(N_x)} -2H_zN_y$$

Chemical shift evolution on nitrogen while decoupling proton and carbon

$$-2H_zN_y \xrightarrow{\omega_N\,(t_1/2)} \xrightarrow{2\,\pi\,J_{NH}\,(t_1/2)\,H_zN_z} \xrightarrow{\pi(H_x)} \xrightarrow{\pi(C_x)} \xrightarrow{\omega_N\,(t_1/2)} \xrightarrow{2\,\pi\,J_{NH}(t_1/2)\,H_zN_z}$$

$$-2H_zN_y \xrightarrow{\pi(H_x)} \xrightarrow{\pi(C_x)} \xrightarrow{\omega_N\,t_1}$$

$$-2H_zN_y \xrightarrow{\pi(H_x)} \xrightarrow{\pi(C_x)} 2H_zN_y \xrightarrow{\omega_N\,t_1} 2H_zN_y\cos(\omega_N\,t_1) + 2H_zN_x\sin(\omega_N\,t_1)$$

Magnetization back-transfer via reversed INEPT

$$2H_zN_y\cos(\omega_N\,t_1) + 2H_zN_x\sin(\omega_N\,t_1) \xrightarrow{\frac{\pi}{2}(N_x)} -2H_zN_z\cos(\omega_N\,t_1) + 2H_zN_x\sin(\omega_N\,t_1)$$

$$-2H_zN_z\cos(\omega_N\,t_1) + 2H_zN_x\sin(\omega_N\,t_1) \xrightarrow{\frac{\pi}{2}(H_x)} -2H_yN_z\cos(\omega_N\,t_1) + 2H_yN_x\sin(\omega_N\,t_1)$$

$$-2H_yN_z\cos(\omega_N\,t_1) + 2H_yN_x\sin(\omega_N\,t_1) \xrightarrow{\pi(H_x)} \xrightarrow{\pi(N_x)} -2H_yN_z\cos(\omega_N\,t_1) - 2H_yN_x\sin(\omega_N\,t_1)$$

$$-2H_yN_z\cos(\omega_N\,t_1) - 2H_yN_x\sin(\omega_N\,t_1) \xrightarrow{4\,\pi\,J_{NH}\,\tau\,H_zN_z} -2H_yN_z\cos(\omega_N\,t_1)\cos(2\pi J_{NH}\tau) +$$
$$H_x\cos(\omega_N\,t_1)sin(2\pi J_{NH}\tau) - 2H_yN_x\sin(\omega_N\,t_1)\cos(2\pi J_{NH}\tau) - 2H_xN_y\sin(\omega_N\,t_1)\sin(2\pi J_{NH}\tau)$$

Again considering the case that $\tau = \frac{1}{4J_{NH}}$ only theH_x and the$-2H_xN_y$ terms survive. The latter of the two is a double quantum coherence that will not be observed during acquisition and the H_x term will start rotating under the influence of chemical shift evolution during the acquisition time t_2. The signal will also exponentially decrease in time with characteristic time T_2 so that the following FID (Free Induction Decay) will be obtained:

$$\big(H_x\cos(\omega_N\,t_1)\cos(\omega_H\,t_2) - H_y\cos(\omega_N\,t_1)\sin(\omega_H\,t_2)\big)\exp(-\frac{t_1}{T_{2,N}} - \frac{t_2}{T_{2,H}})$$

A simple phase cycle that will ensure that magnetization has gone via the nitrogen would be φ_1=x,-x. The finally obtained magnetization will switch accordingly between x and –x, so that the receiver phase should also be φ_r=x,-x. Decoupling on the nitrogen and carbon channel will prevent J-coupling of the signal during acquisition. This would lead to line broadening and thus decrease in signal intensity. In this description we considered the correlation between proton and nitrogen, but a very similar pulse sequence can be used to obtain a proton carbon correlation spectrum.

TROSY

So the most common way to measure the correlation between hetero-nuclear spins (we consider ^{1}H and ^{15}N) in a biomolecular complex is the HSQC experiment. The size of the proteins that can be measured using this method is however severely limited by relaxation effects. During the chemical shift evolution periods, the magnetic spins need to be oriented in the xy-plane making them susceptible to transverse relaxation leading to peak broadening and decreased sensitivity. Two types of interactions that are the main cause of transverse relaxation of magnetic spins in large proteins are dipole-dipole interactions (DD) and chemical shift anisotropy

(CSA). Transverse Relaxation Optimized SpectroscopY or TROSY is a method to decrease the peak broadening during measurements of large proteins by using constructive cancellation of DD and CSA [1].

Before discussing the way TROSY exploits the cross-correlation between DD and CSA, it would be good to look into dipole-dipole interactions and chemical shift anisotropy separately and discuss their effect on line broadening first.

To understand the effect of dipole-dipole interactions we consider a proton H1 next to another proton H2. Proton H1 now experiences a small deviation to the z-magnetic field due to dipolar interaction with its neighbor. These differences in magnetic field experienced by the spins will cause them to precess with a slightly different frequency and so dephase. This will cause T_2 relaxation and hence peak broadening. If proton H1 not only neighbored a proton H2 but also a proton H3, it experiences two dipolar fields. Now we can differentiate between two situations: H1 and H3 have the same spin (both α or both β) or different spins (one α and one β). In the first case the two dipole fields will reinforce each other causing stronger peak broadening but in the latter the fields will almost cancel out, yielding a much sharper peak.

A similar situation can be considered for the interaction between a proton and a nitrogen atom in the amide bond of a protein. Now the nitrogen atom affects the relaxation of the proton magnetization via both dipole-dipole interaction and chemical shift anisotropy. Also the other way around the proton affects the relaxation rate of the nitrogen magnetization. Now like in the case with the three protons the effect between the chemical shift anisotropy and the dipole-dipole interaction can either add up or (partially) cancel each other out depending on whether the spins align or not. So the relaxation rate depends on the so-called cross-correlation between the chemical shift anisotropy and the dipole-dipole interaction.

Now for the spins of a neighboring proton and nitrogen atom there is yet another effect taking place which is the J-coupling. If the spectrum of this particular proton were to be recorded, two peaks would appear, one at the frequency $\omega_H + J_{NH}/2$ when the neighboring nitrogen has spin α and one at frequency $\omega_H - J_{NH}/2$ when the neighboring nitrogen has spin β. If the nitrogen has spin β the chemical shift anisotropy and dipole-dipole interaction partially cancel each other out, so that the peak will be relatively sharp. When nitrogen has spin α, the interactions add up so that the peak will be broad. So for proton we will see a spectrum with a sharp peak at $\omega_H - J_{NH}/2$ and a broad peak at $\omega_H + J_{NH}/2$. The same goes for nitrogen. So an uncoupled 2D spectrum of this amide bond showing both the proton and the nitrogen chemical shift, would give a 4 peaks in a square pattern with different peak width depending on the spin state of the nuclei as shown in Figure 55.

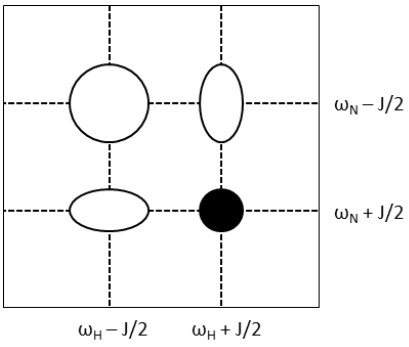

Figure 55. *Splitting of an amine peak due to J-coupling. Peak width is determined by the cross-correlation between DD and CSA. TROSY selects the black peak only.*

In more mathematical terms the Hamiltonian that describes the combination of dipole-dipole interactions and chemical shift anisotropy is given by

$$H = H_{DD} + H_{CSA} = D * H_z N_z + C * N_z$$

$$D = \frac{\gamma_H \gamma_N}{r^3} \hbar (1 - 3cos^2\vartheta)$$

$$C = \omega_0^s \Delta\sigma_s \hbar (1 - 3cos^2\vartheta)$$

Here H_z is the proton z-magnetization and N_z the nitrogen z-magnetization. The dipole-dipole interaction depends on γ the gyromagnetic constant, r the distance between the nuclei, ħ Planck's constant divided by 2π and ϑ the angle between the magnetic moments. The chemical shift anisotropy depends on ω the L'armor frequency of nitrogen and Δσ the difference in magnetic shielding due to nitrogen. It has the same angular dependence as the DD interactions. These equations also already show that only CSA is magnetic field dependent. A property that causes TROSY to be most effective on machines that operate at a proton frequency of around 1 GHz.

Applying this Hamiltonian on a spin system of two spins with m=1/2, as for a proton and a nitrogen gives:

$$\langle \alpha\alpha | H | \alpha\alpha \rangle = \left(\frac{1}{4}D + \frac{1}{2}C\right)$$
$$\langle \alpha\beta | H | \alpha\beta \rangle = \left(-\frac{1}{4}D - \frac{1}{2}C\right)$$
$$\langle \beta\alpha | H | \beta\alpha \rangle = \left(-\frac{1}{4}D + \frac{1}{2}C\right)$$
$$\langle \beta\beta | H | \beta\beta \rangle = \left(\frac{1}{4}D - \frac{1}{2}C\right)$$

For the proton there are two possible spin transitions: one for which the nitrogen is α and one for which it is β. The corresponding transition energies are:

$$N_\alpha: \Delta E = \pm(\alpha\beta - \alpha\alpha) = \mp(\frac{D}{2} + C)$$
$$N_\beta: \Delta E = \pm(\beta\beta - \beta\alpha) = \pm(\frac{D}{2} - C)$$

The relaxation rate that determines the peak width goes with the square of transition energy.

$$\left(\frac{D}{2} + C\right)^2 > \left(\frac{D}{2} - C\right)^2$$

So the proton peak is narrower in the situation that nitrogen has spin β than when it has spin α. A TROSY experiment uses spin state selective magnetization transfer (transferring only α or β spins) so that the slowest relaxing and thus sharpest of the four peaks can be selected.

The pulse sequence used to achieve this goal is very similar to the HSQC pulse sequence, see Figure 56. Also in this case magnetization is transferred from proton to the nitrogen using an INEPT block. Then the nitrogen chemical shift evolution takes place and the magnetization is transferred back to proton and recorded. However in this case no decoupling pulses are applied, neither during the nitrogen chemical shift evolution, nor during the acquisition.

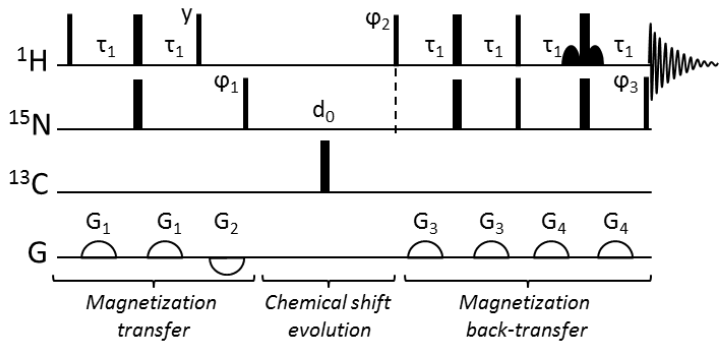

Figure 56. TROSY pulse sequence. Thin black lines represent 90 degree pulses and thick black lines 180 degree pulses. The white hemispheres are gradient pulses. All pulses have phase x unless otherwise indicated. Phase cycling: ϕ_1:y,-y,-x -x, ϕ_2:4(y),4(-y), ϕ_3:4(x),4(-x). Receiver phase: x,-x,-y,y,x,-x,y,-y

CRINEPT

So the TROSY experiment can yield reasonable spectra for proteins up to a molecular weight of about 100kDa by minimizing the transverse relaxation during acquisition. For larger proteins or protein complexes however, transfer relaxation during magnetization transfer becomes a limiting factor. Wüthrich *et al.* [2] also proposed an experiment that exploits cross-relaxation effects to transfer magnetization from one nucleus to another in order to obtain reasonable signal to noise ratio for proteins of even higher molecular weight [2]. The proposed experiment is called cross relaxation enhanced polarization transfer and is often referred to as CRINEPT which is a contraction of CRIPT (Cross Relaxation Induced Polarization Transfer) and INEPT. It combines the principles of both the molecular size independent CRIPT polarization transfer and INEPT transfer that decreases with molecular size so that it, in theory, always yields to better results than either of the two. The CRINEPT-TROSY pulse sequence is given by Figure 57

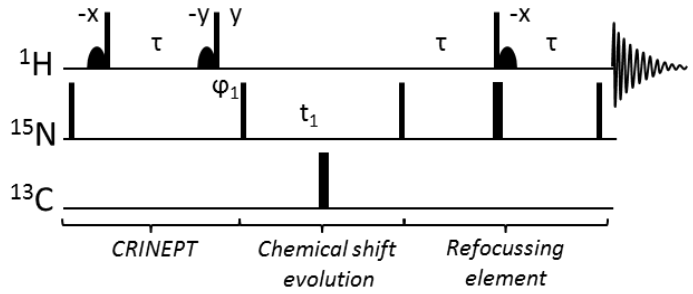

Figure 57. *CRINEPT-TROSY pulse sequence for a triple labeled sample. It also contains a set of gradient pulses that are not shown in this scheme. Narrow bars represent 90 degree pules. Wide bars are 180 degree pulses. The black bullets are water flip back pulses that keep the polarization on water on the z-axis. All phases are x unless otherwise indicated. Phase cycling: ϕ_1=x,-x and ϕ_r=x,-x.*

As mentioned CRINEPT increases sensitivity by combining polarization transfer via INEPT and via CRIPT. We first describe the contribution of INEPT transfer to the obtained anti-phase magnetization during a CRINEPT block. Like during in the description of an HSQC, in-phase magnetization on the proton is transferred to anti-phase magnetization, but now we also take into account the effect of transverse relaxation. According to the Bloch equations, the signal is damped with a factor $\exp(-R_H\tau)$ where R_H is the transverse relaxation rate.

$$H_x \rightarrow H_x\cos(\pi J_{NH}\tau)\exp(-R_H\tau) + 2H_yN_z\sin(\pi J_{NH}\tau)\exp(-R_H\tau)$$
$$H_y \rightarrow H_y\cos(\pi J_{NH}\tau)\exp(-R_H\tau) - 2H_xN_z\sin(\pi J_{NH}\tau)\exp(-R_H\tau)$$

Because in a CRINEPT transfer the chemical shift evolution is not refocused by a 180 degree pulse, this effect also needs to be taken into account.

$$H_y \rightarrow H_y \cos(\omega_H \tau) H_x \sin(\omega_H \tau)$$

Combining these equations, the anti-phase magnetization that is obtained after a period τ as a consequence of INEPT starting from proton y-magnetization is given by the density matrix $\sigma(1)_{INEPT}$

$$\sigma(1)_{INEPT} = -2H_x N_z \sin(\pi J_{NH}\tau)\cos(\omega_H \tau)\exp(-R_H \tau) + 2H_y N_z \sin(\pi J_{NH}\tau)\sin(\omega_H \tau)\exp(-R_H \tau)$$

Now let us consider the effect of cross-relaxation on polarization transfer. As discussed in the part about TROSY, cross-correlation between dipole-dipole interactions and chemicals shift anisotropy cause relaxation. However, theoretical considerations show that together with the decay of in-phase magnetization, cross-relaxation can also lead to simultaneous buildup of anti-phase magnetization thus effectively yielding magnetization transfer.

$$H_x \rightarrow -2H_x N_z \sinh(R_c \tau)\exp(-R_H \tau) + 2H_y N_z \cosh(R_c \tau)\exp(-R_H \tau)$$
$$H_y \rightarrow +2H_x N_z \cosh(R_c \tau)\exp(-R_H \tau) - 2H_y N_z \sinh(R_c \tau)\exp(-R_H \tau)$$

Here R_c represents the rate of cross-relaxation that causes the polarization transfer and R_H is again the transverse relaxation of proton magnetization that damps the signal. Combining the above equations we can describe the antiphase coherence buildup as during CRINEPT. For simplicity we define

$$\cos(\pi J_{NH}\tau)\sinh(R_c \tau)\exp(-R_H \tau) = A_{1H}$$
$$\sin(\pi J_{NH}\tau)\cosh(R_c \tau)\exp(-R_H \tau) = A_{2H}$$

Here the 1 refers to the fact that during this type of polarization transfer the direction of the magnetization remains the same (e.g. $H_x \rightarrow H_x N_z$) and the 2 means that the direction of the polarization shifts 90 degrees (e.g. $H_x \rightarrow H_y N_z$). Then the polarization will be transferred as follows

$$H_x \rightarrow -2H_x N_z * A_{1H} + 2H_y N_z * A_{2H}$$
$$H_y \rightarrow +2H_x N_z * A_{2H} - 2H_y N_z * A_{1H}$$

Now starting from proton y-magnetization and taking the chemical shift evolution into consideration the obtained antiphase polarization after period τ is given by density matrix σ(1)

$$\sigma(1) = \left(-2H_x N_z * A_{2H} + 2H_y N_z * A_{1H}\right)\cos(\omega_H \tau) - \left(2H_x N_z * A_{1H} + 2H_y N_z * A_{2H}\right)\sin(\omega_H \tau)$$

Reorganizing this equation by separating y-antiphase magnetization from x-antiphase magnetization gives

$$\sigma(1) = -2H_x N_z[A_{2H}\cos(\omega_H \tau) + A_{1H}\sin(\omega_H \tau)] + 2H_y N_z[A_{1H}\cos(\omega_H \tau) - A_{2H}\sin(\omega_H \tau)]$$

Now a set of two 90 degree pulses flips the antiphase coherence of the first term to antiphase coherence on nitrogen and the coherence of the second term becomes a multiple quantum coherence.

$$-2H_x N_z[A_{2H}\cos(\omega_H \tau) + A_{1H}\sin(\omega_H \tau)] \xrightarrow{\frac{\pi}{2}(H_y)} \xrightarrow{\frac{\pi}{2}(N_x)} -2H_z N_y[A_{2H}\cos(\omega_H \tau) + A_{1H}\sin(\omega_H \tau)]$$
$$2H_y N_z[A_{1H}\cos(\omega_H \tau) - A_{2H}\sin(\omega_H \tau)] \xrightarrow{\frac{\pi}{2}(H_y)} \xrightarrow{\frac{\pi}{2}(N_x)} +2H_y N_y[A_{1H}\cos(\omega_H \tau) - A_{2H}\sin(\omega_H \tau)]$$

Since the multiple quantum coherence will not be observed during the acquisition, we ignore it from here on. Subsequently chemical shift evolution in the nitrogen dimension takes place during t_1. Again no decoupling

pulse is applied because the sequence is transverse relaxation optimized. As a consequence J-coupling has to be taken into account and the obtained density matrix after t_1 is given by σ(2)

$$\sigma(2) = \begin{bmatrix} [-2H_z N_y \cos(\omega_N t_1) - 2H_z N_x \sin(\omega_N t_1)]\cos(\pi J_{NH} t_1) \\ +[N_x \cos(\omega_N t_1) - N_y \sin(\omega_N t_1)]\sin(\pi J_{NH} t_1) \end{bmatrix} * [A_{1H} \cos(\omega_H \tau) - A_{2H} \sin(\omega_H \tau)]$$

The N_y-magnetization will not be observed because it is not transferred to proton magnetization by the remaining pulse sequence. The same goes for the H_zN_x-term, so we will ignore both terms from now on. That means that after the 90 degree pulse that concludes that t_1 evolution the remaining magnetization is given by σ(3)

$$\sigma(3) = [2H_z N_z \cos(\omega_N t_1)\cos(\pi J_{NH} t_1) + N_x \cos(\omega_N t_1)\sin(\pi J_{NH} t_1)] * [A_{1H} \cos(\omega_H \tau) - A_{2H} \sin(\omega_H \tau)]$$

This magnetization will be transferred back to proton in a similar manner as before, making use of cross-relaxation effects. The spin-echo like block is required to refocus the proton chemical shift evolution of the CRINEPT block. Finally both an antiphase component and an inphase component are acquired, which are separated by phase cycle on final 90 degree pulse and the receiver phase. This type of acquisition is very similar to TROSY. The combination of this CRIPT transfer and INEPT transfer leads to a more efficient transfer than either of the two provided that the transfer time is chosen properly. Considering the fact that the optimum is different from INEPT transfer than for CRIPT, this choice is non-trivial and can only be found by experimental optimization. Figure 58 shows the theoretical transfer efficiency by CRINEPT compared with CRIPT and INEPT for proteins with different tumbling times (i.e. of various sizes).

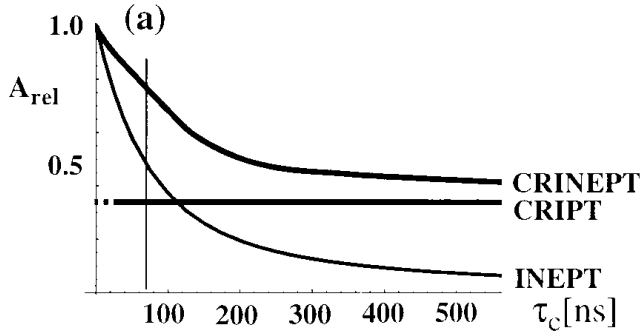

Figure 58. *Transfer efficiency of INEPT, CRIPT and CRINEPT as function of molecular size. CRINEPT is in theory always more efficient than either of its two components. Note that for small proteins with low rotation correlation times INEPT is a fairly efficient type of magnetization transfer, but that for larger protein CRIPT transfer provides the largest contribution. Copied from ref [2]*

CRIPT

Although the principles behind CRIPT are already discussed, it would be good to elaborate on practical applications of this experiment, since it has several interesting properties, amongst others its ability to selectively measure high molecular weight species. As mentioned, CRIPT exploits cross-relaxation effects to transfer polarization from one nucleus to the other. The effectiveness of this polarization transfer depends on the relaxation rate R_c. When considering an amide bond, the relaxation depends on the strength of both the CSA and the DD interactions and is given by the following equation:

$$R_c = \frac{4}{15}(\gamma_H B_0 \Delta\sigma_H) * \left(\frac{\hbar \gamma_H \gamma_N}{r_{HN}^3}\right) * \tau_c$$

Here the first term accounts for the chemical shift anisotropy and the second term for the dipole-interactions. What is important to notice is that the relaxation rate increases linearly with the rotation correlation time.

Because of that, the optimal transfer T_{opt} time will be inversely proportional to τ_c. So that in theory, by varying the transfer time different protein sizes within a mixture can be sampled.

Let us now consider the specific case of a sample containing HBV capsids with T=4 geometry and around 1 molpercent of residual dimer. The dimers have an estimated rotation correlation time of several nanoseconds, whereas the rotation correlation time of the capsid is expected to be 3-6 microseconds. To see what the consequences are for the optimal transfer time, we use the experimentally determined T_{opt} of 5 ms for aldolase (τ_c ≈70ns) by Riek *et al.* [ref] as a reference. Using the observation that T_{opt} is inversely proportional to τ_c we estimate $T_{opt} \approx 10^{-1}$ ms for the capsid, where the optimal transfer time of the free dimer would only be longer than that for aldolase. So when the CRIPT transfer time is optimized for one size of structure, by definition it leads to poor transfer for a structure of a different size. This allows us to measure the capsid only and get rid of peaks with faster rotation correlation times, like the free dimer. The pulse sequence of the CRIPT experiment is shown in Figure 59.

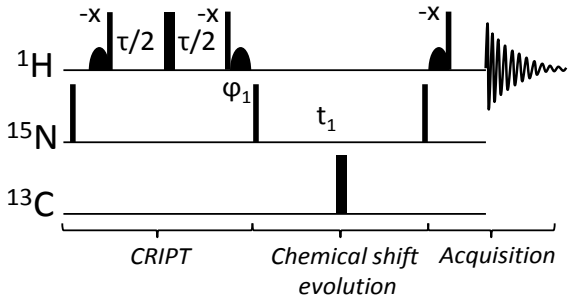

Figure 59. *Pulse sequence of a CRIPT-TROSY. Thick black bars represent 180 degree pulses. Narrow bars represent 90 degree pulses. The filled black bullets are water flip back pulses (shaped pulses designed to selectively excite water) that keep the water magnetization along the z-axis.*

The other advantage of CRIPT over CRINEPT is that magnetization transfer only depends on one process, the efficiency of which linearly depends on the effective rotation correlation time. This property enables us to get information on this $\tau_{c,eff}$ by finding the optimal transfer time for each peak. One knows that the overall tumbling time of the structure is the same for each residue in a protein, so any difference in $\tau_{c,eff}$ will be due to internal dynamics. Hence the CRIPT experiment can also be used as a qualitative dynamics measurement technique.

DOSY

NMR spectroscopy allows for the accurate measurement of diffusion rates of proteins and protein complexes using the so-called DOSY (Diffusion Ordered SpectroscopY) experiment. This is basically a series of 1D experiments where the decay in signal intensity over the series is a measure of the diffusion coefficient. The principle of DOSY relies on the fact that information about the location of a protein can be stored as magnetization strength by using magnetic gradients.

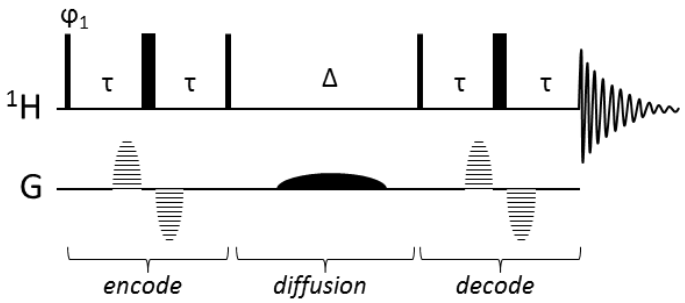

Figure 60. *Pulse sequence of a stimulated echo diffusion experiment using bipolar gradients. Thick bars represents a 180 degree pulse and lines 90 degree pulses. Striped pulses are the encoding and decoding*

gradient pulses. The filled black gradient is a cleanup pulse that dephases unwanted xy-magnetization during the delay period. A simple phase cycle that ensures that magnetization has been encoded and decoded is ϕ_1 = x,-x and all other pulses x. Then the receiver phase must -y,y

The DOSY experiment (see Figure 60) can roughly be divided in four parts: The encoding, the diffusion, the decoding and finally the acquisition. During the encoding part the z-magnetization is flipped into y (or x) magnetization using a 90 degree x (or y) pulse. Without the presence of a z-gradient this y-magnetization would dephase during a delay τ, be flipped by the 180 degree pulse and be refocused again at the location of the second 90 degree pulse after another delay τ. However, because of the presence of the two gradient pulses acting as a temporal z-gradient in the magnetic field, the y-magnetization will dephase in a location-dependent manner. The stronger the z-field, the larger the defocussing effect and so the smaller the part of the magnetization that is refocused by the 180 degree pulse. The second 90 degree pulse will store the magnetization at the z-axis. But because it carries the same phase as the first 90 degree pulse (or minus the phase of the first pulse), it will only affect the y-magnetization. That means that spins that experienced a strong z-gradient, and thus were completely dephased (giving equal amounts of x- and y-magnetization), will have only 50% of its initial magnetization refocused and thus will lead to a small z magnetization after the encoding period. Spins that experienced almost no z-gradient however will be almost completely refocused and hence almost 100% of their initial magnetization will be stored as z-magnetization after the encoding period. So after this period the location on the z-axis of every spin is encrypted as z-magnetization.

During the diffusion delay all information containing magnetization is stored nicely along the z-axis, but the magnetization that was not refocused during the encoding part is still rotating in the xy-plane. A strong gradient pulse is given to dephase this unwanted magnetization so that it will not be observed after the experiment. Δ Is a long delay (in the order of a hundred milliseconds) so that the protein diffuses through space and thus changes is z-coordinates. Obviously smaller proteins with a larger diffusion coefficient move faster and thus have on average moved further away from their initial position.

The first 90 degree pulse of the decoding part flips the z magnetization back to the xy-plane. Let us now first consider the situation that there is no diffusion (or Δ is extremely short), so that all spins have exactly the same z-coordinate as during the encoding period. Note firstly that the two 90 degree pulses around the diffusion delay give a net 180 degree pulse so that all spins will have exactly the opposite sign during the decoding period as with respect to during the encoding period. As a consequence the z-gradient will have exactly the opposite effect now. Magnetization that was strongly defocussed during the encoding part will barely be defocussed during the decoding part and vice versa so that every spin will now have 50% magnetization independent of their location. However, when a protein diffuses, the spins do not exactly experience the opposite magnetic gradient during the decoding period and the final magnetization will not be 50% but smaller. Now the faster a protein diffuses, the bigger the difference between the encoding magnetic gradient and the decoding magnetic gradient that a spin experiences and the smaller the final magnetization is. So the final magnetization happens to be a measure for the average displacement of a spin during the diffusion delay.

The magnetization is recorded during the acquisition period where every spin rotates with a different frequency depending on their chemical environment (like in a normal 1D proton spectrum) so that the frequency of a peak yields information about the chemical environment of a spin and the relative peak intensity with respect to the maximum peak intensity gives information about the diffusion behavior of the spin. Problem is clearly that one does not a priori know the maximum peak intensity. Therefore a diffusion experiment could be set up as a set of 1D experiments as described above in which the diffusion delay is sequentially increased. This way the effect of diffusion would become more dominant in every next experiment so that the signal intensities will decrease following an exponential decay that can be described by the Stesjkal-Tanner equation [3]

$$S = S_0 * Exp\left[-D\delta^2 g^2 \gamma^2 \left(\Delta - {}^{\delta}/_{3}\right)\right]$$

Here S is the measured intensity, S_0 the maximum intensity, D the diffusion coefficient, and Δ the diffusion delay. There is however a main disadvantage of using the diffusion delay as variable during this type of experiment, because increasing Δ will not only increase the effect of diffusion on the signal intensity but also cause a longer period in which T_1 relaxation can occur. That means that two separate effects will cause the signal intensity to decrease during the experiment so that no unbiased diffusion coefficient could ever be obtained. Therefore it is more convenient to increase the gradient strength every next experiment while keeping the diffusion delay constant. This will also increase the effect of diffusion on the intensity but the loss of signal due to T_1 relaxation will now be the same in every experiment.

Then the diffusion coefficient of a protein can be calculated by plotting the signal intensity as function of the gradient strength and fitting the Stesjkal-Tanner equation through the data points using the maximum intensity and diffusion coefficient as fit parameters. The diffusion coefficient can subsequently be back calculated to a size using the Stokes-Einstein equation assuming ideal behavior of spherical objects

$$D = \frac{kT}{6\pi\eta r}$$

where k is Boltzmann's constant, T the temperature, η the viscosity and r the radius.

The experiments performed on the HBV capsid are not actual DOSYs but the transverse relaxation optimized version called ^{15}N-TRO-STE (Transverse Relaxation Optimized STimulated Echo) [4]. This experiment exploits the TROSY effect to minimize transverse relaxation during acquisition. Moreover the magnetization is stored as spin order magnetization (H_zN_z) during the diffusion delay. This type of magnetization has slower T_1 relaxation so that longer diffusion delays are achievable.

References

1. Pervushin, K., Riek, R., Wider, G. & Wüthrich, K. Attenuated T2 relaxation by mutual cancellation of dipole-dipole coupling and chemical shift anisotropy indicates an avenue to NMR structures of very large biological macromolecules in solution. *Proc. Natl. Acad. Sci. U. S. A.* **94,** 12366–71 (1997).

2. Riek, R., Wider, G., Pervushin, K. & Wüthrich, K. Polarization transfer by cross-correlated relaxation in solution NMR with very large molecules. *Proc. Natl. Acad. Sci. U. S. A.* **96,** 4918–23 (1999).

3. Sinnaeve, D. The Stejskal – Tanner Equation Generalized for Any Gradient Shape — An Overview of Most Pulse Sequences Measuring Free Diffusion. **40,** 39–65 (2012).

4. Horst, R., Horwich, A. & Wüthrich, K. Translational diffusion of macromolecular assemblies measured using transverse-relaxation-optimized pulsed field gradient NMR. *J. Am. …* **133,** 16354–16357 (2011).

5. Arthur G. Palmer III, Wayne J. Fairbrother, John Cavanagh, Nicholas J. Skelton, M. R. *Protein NMR spectroscopy ISBN:978-0121644918*. 978 (Academic Press, 2006).

Appendix: Pulse program for z-gradient calibration, by Hugo van Ingen

```
;hvi_imgegp1d
;avance-version
;1D Gradient Echo for gradshim-procedure


#include<Avance.incl>
#include<Grad.incl>
#include<De.incl>



"d11=30m"

1 ze
  d11 UNBLKGRAD
2 d1
  (p1 ph1):f1
  d21 gron1
  ACQ_START (ph30,ph31)
  aq DWELL_GEN:f1
  5u groff
rcyc=2
  d11 wr #0
  d11 BLKGRAD
exit


ph1=0 2
ph30=0
ph31=0 2


;pl1 : f1 channel - power level for pulse (default)
;p1 : f1 channel -  small flip angle              [2 usec]
;d1 : relaxation delay
;d11: delay for disk I/O                         [30 msec]
;d21: gradient stabilisation delay
```

Summary

The goal of this study was to obtain a better understanding of the self-assembly process that leads to the formation of hollow virus capsids and more specifically the role of entropy therein. To this means we extended the model of the virus interaction potential previously discussed by Kegel and Van der Schoot with pH dependence of the interaction strength. Comparison of the calculated interaction potentials with the experimental potentials (that were calculated from the observed critical monomer concentrations) showed quantitative agreement for the Hepatitis B virus, and the same order of magnitude for the Norovirus and the Brome Mosaic Virus.

The model was used to predict the ratio between different polymorphs of the Hepatitis B virus. We found that the addition of a curvature free energy term was required to account for the experimentally observed polymorphism. Furthermore we compared a model based on kinetics and one based on thermodynamics and found that measurements of the concentration of the different polymorphs at high overall protein concentrations can distinguish between kinetically and thermodynamically governed polymorphism.

Lastly we performed NMR experiments on hollow HBV capsids, with an apparent size of 20 MDa. Diffusion measurements indicated that large protein assemblies are indeed present but yielded diffusion coefficients that were lower than expected. The results could be explained by a model of stochastic adsorption and release of dimers where the timescale of the exchange process Is of the order of 1 s.

The dynamics of the coat proteins that makes up the virus capsid were assessed using a novel CRIPT-based experiment. The measurements showed that the tail of the protein is highly dynamic, with rotation correlation times of the order of nanoseconds. The rest of the protein does not show significant dynamics of the order of microseconds of faster. Slower dynamics cannot be excluded since they are not accessible to NMR techniques.

Acknowledgements

Thanks to Willem Kegel, Rolf Boelens and Hans Wienk for great supervision. I would like to thank also Paul van der Schoot and Jan Groenewold for their help with the theoretical part and Hugo van Ingen for is help with the NMR part. Special thanks also to our collaborators Maaike Jurgens and Crispin Alexander and Dr. Neil Feruson for preparation of the NMR sample and to our collaborator Stephan Freund for feedback and discussions. Lastly thanks to the Friday morning brainstorm for enlightening discussion and to FCC and NMR for a pleasant working environment.